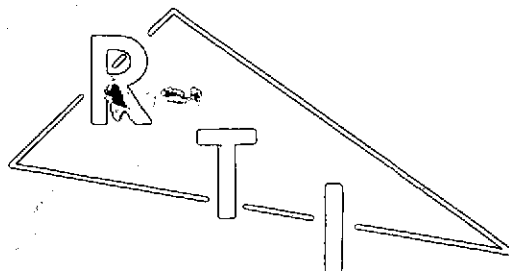


2C (mk)

NASA CR-137466



RESEARCH TRIANGLE INSTITUTE

ENGINEERING STUDIES RELATED TO
GEODETIC AND OCEANOGRAPHIC REMOTE
SENSING USING SHORT PULSE TECHNIQUES

L. S. Miller
G. S. Brown
G. S. Hayne

Final Engineering Report
For Tasks B and E
February 1973

Prepared Under
NASA CONTRACT NO. NAS6-2135

for

National Aeronautics and Space Administration
Wallops Station
Wallops Island, Virginia 23337

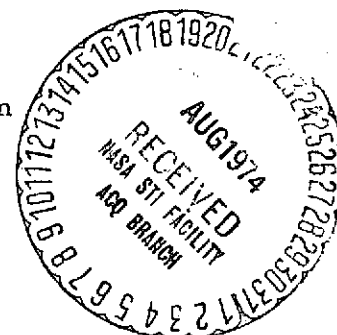
(NASA-CR-137466) ENGINEERING STUDIES
RELATED TO GEODETIC AND OCEANOGRAPHIC
REMOTE SENSING USING SHORT PULSE
(Research Triangle Institute Research
Triangle) 120 p HC \$9.00

CSCL 14B

G3/13

Unclass
46530

N74-30843



RESEARCH TRIANGLE PARK, NORTH CAROLINA 27709

FOREWORD

This report was prepared for the National Aeronautics and Space Administration by Drs. L. S. Miller, G. S. Brown and G. S. Hayne of the Research Triangle Institute under Contract No. NAS6-2135. Messrs J. T. McGoogan and H. R. Stanley of NASA/Wallops Station acted as technical coordinators of the contract.

The authors would like to express their appreciation to E. L. Hofmeister of the General Electric Company, Utica, New York, for valuable assistance provided through numerous informal discussions.

ABSTRACT

For the Skylab S-193 radar altimeter, this report presents data processing flow charts and identification of calibration requirements and problem areas for all presently defined S-193 altimeter experiments, and an analysis and simulation of the relationship between one particular S-193 measurement ("mean-of-the-peaks") and the parameter of interest ("peak-of-the-mean") for determining the sea surface scattering cross-section, σ^0 . For the GEOS-C radar altimeter, this report presents results of system analyses pertaining to signal-to-noise ratio, pulse compression threshold behavior, altimeter measurement variance characteristics, desirability of on-board averaging, tracker bandwidth considerations, and statistical character of the altimeter data in relation to harmonic analysis properties of the geodetic signal.

CONTENTS

	<u>Page No.</u>
Foreword	ii
Abstract	iii
<u>Chapter</u>	
1. Introduction and Summary of Results	1-1
1.0 Scope of the Report	1-1
1.1 Conclusions and Recommendations	1-1
2. TASK B: S-193 Altimeter Calibration Logic	2-1
2.0 Introduction	2-1
2.1 Altimeter Data Calibration by Mode	2-3
2.1.1 Mode I: Pulse Shape	2-3
2.1.2 Mode II: Cross-Section (σ^0)	2-8
2.1.3 Mode III: Time Correlation	2-9
2.1.4 Mode V: Pulse Compression	2-16
2.1.5 Special Problems to be Resolved	2-16
2.2 Altimeter Experimentation Data Flow	2-24
2.2.1 Data Flow and Processing Diagram	2-24
2.2.2 Quick Look Data Processing for σ^0	2-28
References	2-32
Appendix 2A: Mean Return Waveform Computation for Mode II	2-33
Appendix 2B: Simulation of the AGC r-Factor	2-53
Appendix 2C: Computer Programming for Tracker and Sample-and-Hold Simulation	2-62
3. TASK E: GEOS-C Satellite Program	3-1
3.0 Introduction and Summary	3-1
3.1 Altimeter Data Considerations	3-1
3.1.1 Analysis of Altimeter-Data Variance Characteristics as Influenced by the On-Board Tracker	3-5
3.1.2 Discussion of Altimeter Variance as Influenced by Digital Delay Gate Start Signal Quantization Error	3-10

3.2	Open Questions Regarding Estimated Values of Altimeter SNR	3-14
3.2.1	The Threshold Effect	3-14
3.2.2	SNR Estimates	3-17
3.2.3	Sea State Experimentation	3-19
3.3	Telemetry Requirements	3-20
3.4	Recommended Calibration Tests	3-24
	References	3-33
	Appendix 3A:	3-34

CHAPTER 1

INTRODUCTION AND SUMMARY OF RESULTS

1.0 SCOPE OF THE REPORT

This is the final engineering report on Tasks B and E of NASA Contract No. NAS6-2135. Task B consisted of a study of data processing and calibration procedures for the Skylab S-193 altimeter, and Task E consisted of system analyses and related factors for the GEOS-C satellite program. Task D, which is still in progress and is to be reported separately, comprises a study of oceanographic current sensing using remote sensing methods.

Chapter 2 of this report summarizes our work on Task B, the S-193 task, examining the data processing required to calibrate and/or correct the data which the S-193 radar altimeter will obtain. Special problem areas such as signal-to-noise ratio determination and RF system losses are addressed in detail. A data flow and processing diagram which suggests data reduction/analysis responsibilities is also presented. Finally, the problem of relating the altimeter AGC measurement to the peak-of-the-mean return waveform is investigated in order to obtain radar cross-section (σ^0) data from the S-193 altimeter.

Chapter 3 reports the Task E (GEOS-C) work and gives results of investigations of several system engineering aspects of the altimeter. Recommended calibration data requirements to support waveform experiments are also reported. The system analyses pertain to potential problem areas of signal-to-noise ratio (SNR), pulse compression threshold behavior, altimeter measurement variance characteristics, desirability of on-board averaging, tracker bandwidth considerations as influenced by waveform experiments, and the statistical character of the altimeter data in relation to harmonic analysis properties of the geodetic signal.

1.1 Conclusions and Recommendations

The following paragraphs summarize the principal findings of this study and the remainder of this report provides the detailed work from which these conclusions and recommendations are derived.

TASK B, the S-193 task (see Chapter 2):

1. Data obtained by the S-193 radar altimeter do not permit a direct determination of receiver signal-to-noise ratio. Analytical results presented

in this report provide a means for determining the signal-to-noise ratio, but they must be substantiated by measurements on the S-193 breadboard hardware.

2. Determination of σ^0 from the S-193 altimeter AGC data can only be approximately accomplished for off-nadir angles of 0, 0.5 and 1.5 degrees. To overcome this problem, we recommend that an r-factor study be conducted using the S-193 breadboard hardware in conjunction with pulse shaping circuits which approximate computed waveshapes for 0, 0.5, 1.5, 3, 8 and 15.6 degrees off-nadir.

3. Time sidelobes due to the pulse expansion/ compression network prevent the accurate measurement of sample-and-hold (S&H) gate offset levels in Mode V of the S-193 radar altimeter. Measurements on the breadboard hardware should be made to ensure that S&H level offset is stable from mode to mode.

4. There is a definite need for measurements of instantaneous and average tracker jitter as a function of signal-to-noise ratio. These data are required for post-flight S&H gate position reconstruction and evaluation of the altimeter under radial acceleration conditions.

5. Additional RF-loss measurements must be made on the breadboard hardware to eliminate unknown loss factors which directly affect the measurement of σ^0 .

TASK E, the GEOS-C task (see Chapter 3):

1. We recommend the incorporation of a lower (~ 5 Hz) closed-loop altitude tracker bandwidth option in addition to the presently planned 4.0 Hz bandwidth. The availability of this lower bandwidth option would lessen the need for derivation of S&H positional jitter in waveform reconstruction, provide more desirable slew characteristics for the final acquisition step, and provide an on-board filtering capability more nearly in consonance with the spatial filter effect. More study and analysis is needed to quantitatively characterize this last effect, especially in regard to data processing methods for altitude and slope extraction.

2. Regarding system configuration, we feel that the on-board averaging processes (the signal conditioners following the altitude tracker) do not favorably affect statistical properties of the altimeter data and are generally superfluous. These characteristics may in fact be obtained by appropriate

changes in tracker bandwidths. Also signal-to-noise considerations are felt to argue against use of a 40 dB time sidelobe filter with its attendant loss properties. A 20 dB filter is considered to be a better choice. Also, SNR levels are such that time sidelobes are not expected to be a prime consideration.

3. We recommend that system level tests of the type described be conducted to determine if latent problem areas exist, such as the threshold effect discussed. We also emphasize the need for statistical data on the altitude quantization problem and on tracker performance at SNR values near 0 dB.

4. The acquisition of more performance and qualification test data is strongly recommended. The Skylab S-193 altimeter program has amply demonstrated the need for such data in support of data processing and technology evaluation. We also recommend that the GEOS-C Altimeter Experiment Proposals be reviewed before completion of the hardware test phase to determine the possible need for added test activities, even if the satellite program time schedule dictates that such data be obtained on back-up hardware.

CHAPTER 2

TASK B: S-193 ALTIMETER CALIBRATION LOGIC

2.0 INTRODUCTION

As a consequence of the spacecraft hardware constraints and the rather sophisticated experimental objectives of the S-193 radar altimeter, little if any of the raw data from the altimeter can be used without extensive calibration. Except for the Nadir Align mode, each functional mode of the altimeter contains calibration steps in its operating sequence. It would of course be desirable to obtain all of the calibration data during in-flight operation of the altimeter; however, this is impractical. Therefore, it will be necessary to augment the in-flight data with preflight measurements. In addition, some calibrations cannot be accomplished even during preflight, and we must rely on simulation and/or analytical results. A very general block diagram of how these various calibration data will be merged to yield information for the sensor evaluation and EREP programs is shown in Figure 2.1.

Except for the requirement of proper operation of Mode VI (Nadir Align), all of the operating modes of the S-193 radar altimeter are functionally independent. Also, the data obtained in one mode may not be completely correlated with the data from another mode due to the motion of the spacecraft and changes in the scattering surface. For this reason, it appears logical to develop raw data calibration procedures on a mode-by-mode basis. Basic data calibration block diagrams are developed in Section 2.1 of this chapter.

Once the raw data are calibration corrected, they are available for use by S-193 radar altimeter sensor technology and EREP experimenters. The goals of these experimenters, however, dictate additional data processing which is beyond mere calibration. In order for NASA to know the type and scope of this additional data processing, Section 2.2 presents a general discussion of this topic. In particular, a block diagram is presented which outlines the anticipated areas of responsibility and the type of processing anticipated for the EREP categories. Also shown in the diagram are the expected outputs from the various experiments. Additionally, Section 2.2 contains a short discussion of the type of data reduction which will be necessary in order to obtain a "quick-look" estimate of σ^0 from the Skylab data.

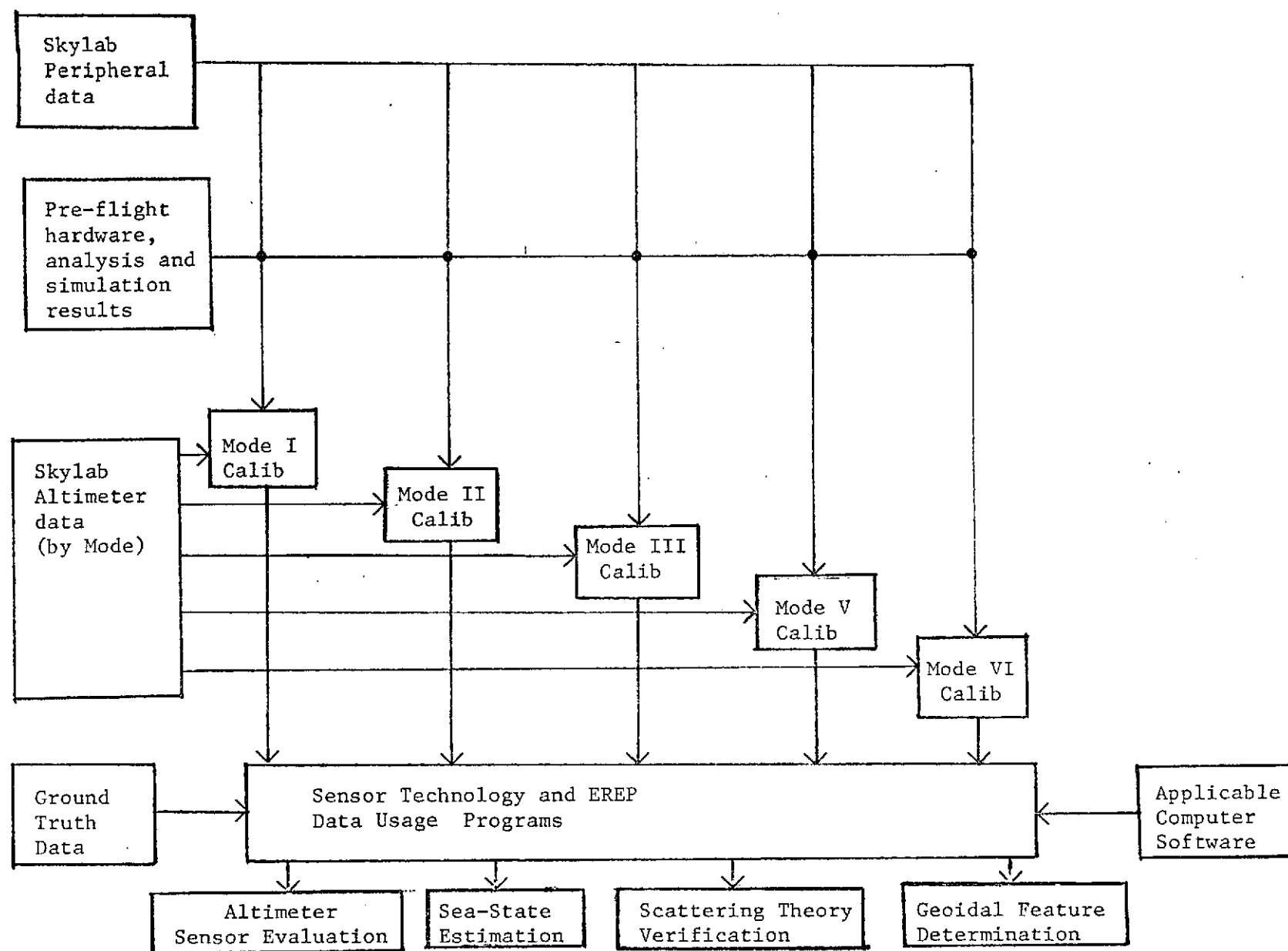


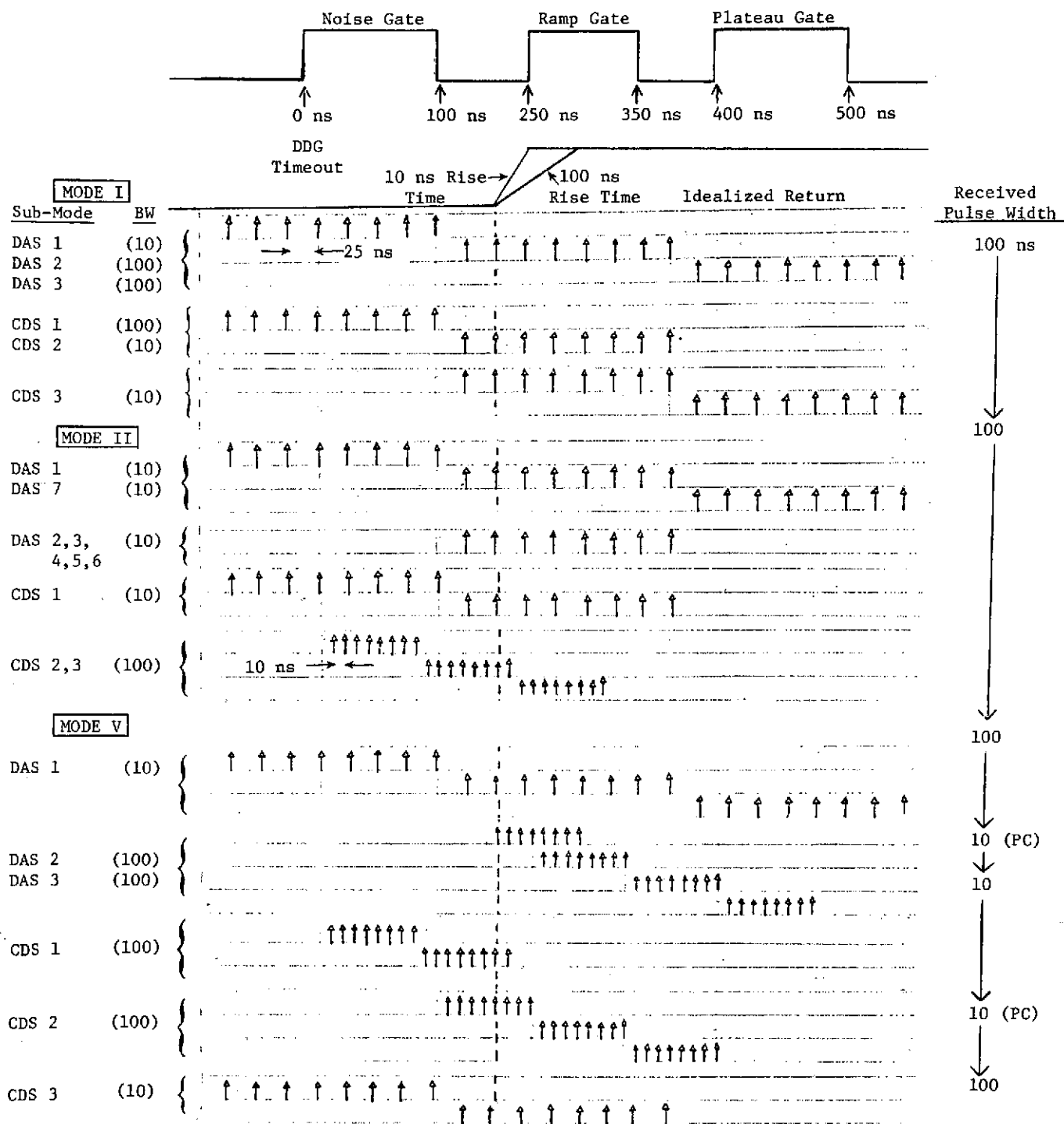
Figure 2.1. Data processing, calibration and usage diagram for the S-193 radar altimeter.

2.1 Altimeter Data Calibration by Mode

2.1.1 Mode I: Pulse shape.— Throughout this section we will refer to the mean location of the returned signal relative to the noise, ramp and plateau gates and also to the locations of the Sample and Hold (S&H) gates in the various operating modes. To avoid possible confusion, Figures 2.2 and 2.3 have been included to show the positions of the various gates relative to the mean return for all of the operating modes and DAS (Data Acquisition Step) or CDS (Calibration Data Step) sub-modes. Figure 2.2 is applicable to Modes I, II, and V, while Figure 2.3 covers Mode III. In Figure 2.3, the time difference between the first and second returns is not to scale in order to get all of the "2nd" returns on the graph. Also, the number "4" appearing in the S&H gate positions in DAS-2 and 3 denotes the presence of four S&H gates; the relative spacing of the gates is the same as the S&H gates which sample the first return.

Figure 2.4 is the data processing block diagram for obtaining calibration data from Mode I, CDS-1, 2, and 3. The purpose of this processing is to obtain corrected data which are not available from the DAS sub-modes. In particular, the corrected outputs will be: the peak transmitter power, S&H gate timing, S&H gate level offset and transmitted waveforms as influenced by the transmitter, receiver and S&H gates. Most of the processing indicated is relatively straightforward; however, there are some special points of caution to be noted. Level offset of the eight S&H gates should be determined from the first eight S&H gate positions in CDS-1 since the gates are sampling zero-mean noise in this sub-mode. It is also recommended that a level offset be determined from the last eight S&H positions in CDS-3 (see Figure 2.2), and these results should also be the same as with CDS-1. Histograms should be plotted for these S&H gates to determine if each S&H gate is operating properly. Any drastic difference in the histograms recorded by each of the eight S&H gates (apart from changes in the mean) will most probably indicate a malfunction in the gate for certain classes of malfunctions. In this way we can isolate improperly operating gates and ignore the data recorded by the gate. L_T^* and L_R^* are losses in the transmit and receive paths, respectively, which are not included in the path loss measurement made in the CDS sub-modes. A more detailed discussion of these losses is presented in Section 2.1.5.

Figure 2.5 indicates the processing which will be required for all of the DAS sub-modes of Mode I. As shown by the stars, there are a number of data processing functions which are either yet to be determined or are problem areas. Included in this category are the following outstanding problems. The



Sample Points, As Shown, Occur when the Actual Readout Time Occurs. This is 25 or 10 ns after start of the sample.

Figure 2.2. S&H gate positioning for Modes 1, 2, and 5 based on information available as of November 1972.

MODE III

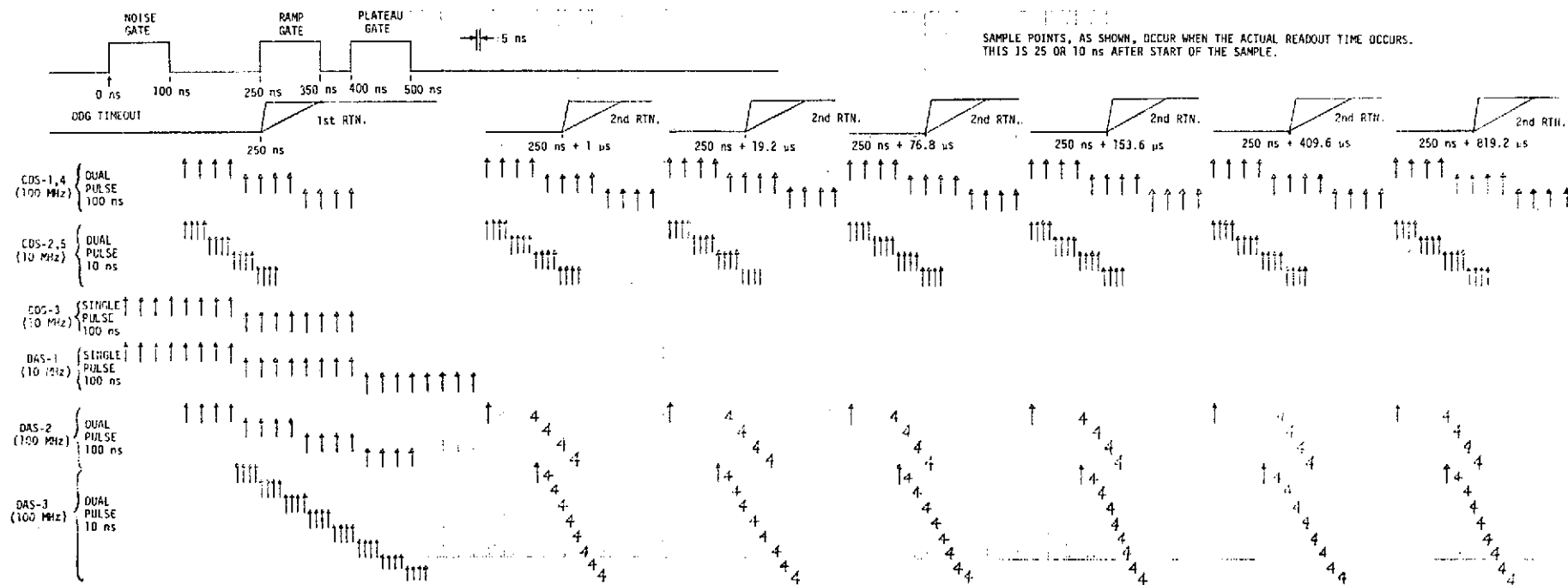


Figure 2.3. S&H gate positioning for Mode 3 based on information available as of November 1972.

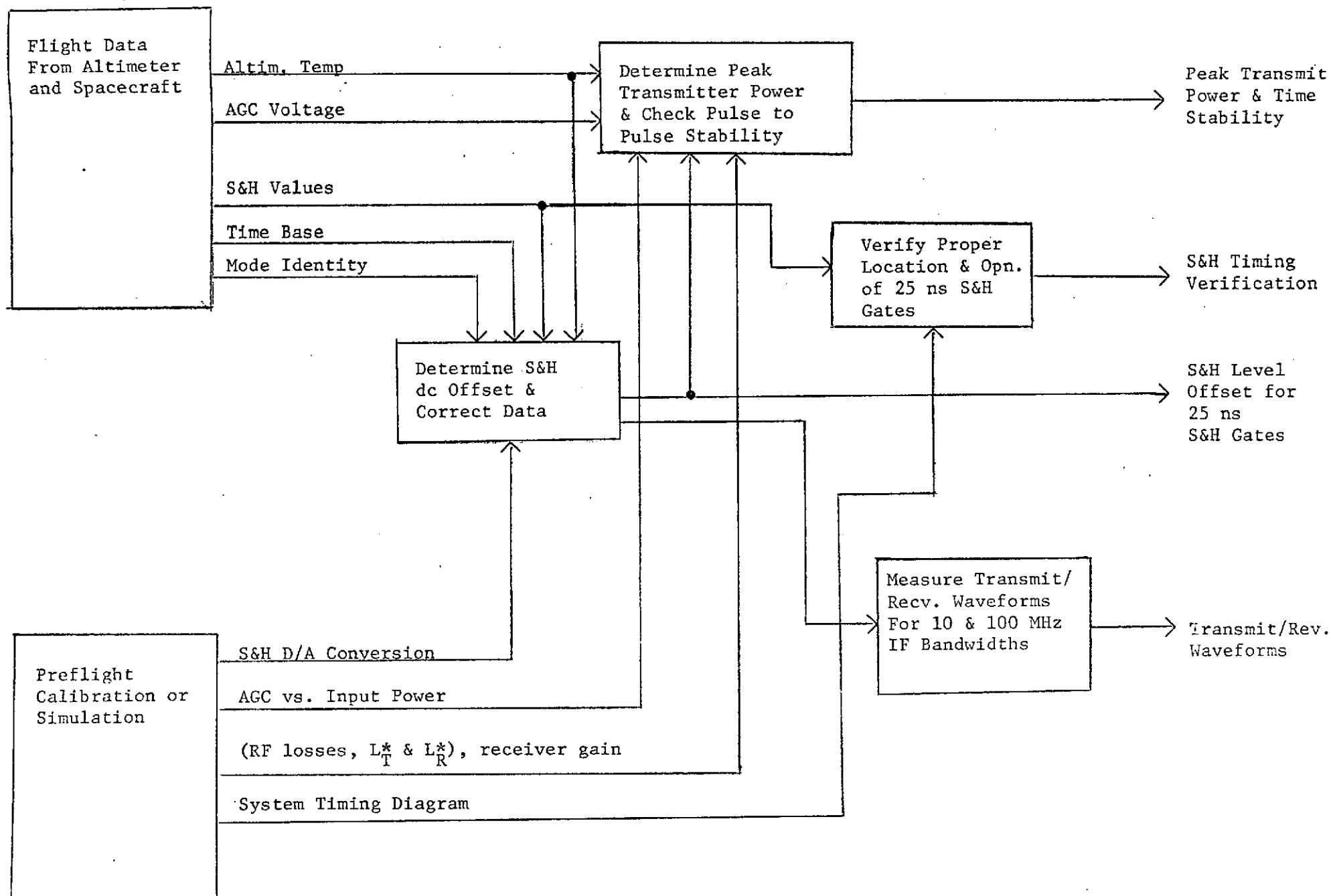


Figure 2.4. Data processing diagram for Mode I, CDS-1, 2, and 3.

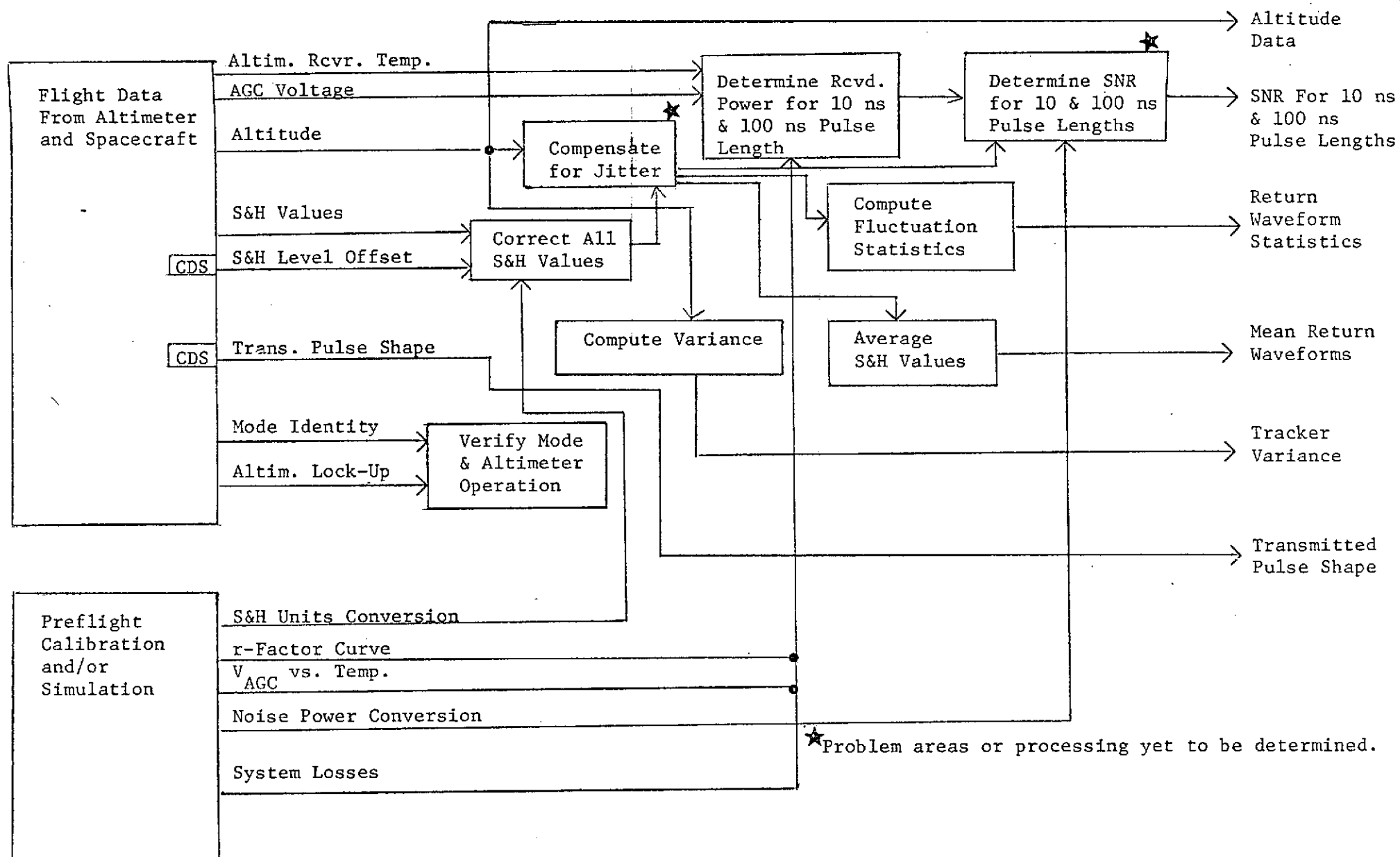


Figure 2.5. Data Processing for Mode I, DAS-1, 2, and 3.

ratio of the peak-of-the-mean return waveform (which is required to determine σ^0 and Signal-to-Noise Ratio (SNR)) to the mean-of-the-peaks of the return waveform (which is measured by the AGC) is defined as the r-factor. Determination of the r-factor is a major problem and is discussed in Section 2.1.5 and in Appendix 2B. Compensation of the tracker jitter in order to align the S&H gates appears to be a very complex problem because of the different signal points involved and the marginal rate at which the tracker error is recorded (eight times per second). Details of a tracker simulation scheme are given in Appendix 2C. It is also not obvious how an estimate of the SNR can be made from the altimeter data. Originally, it was thought that the integrated noise gate voltage would be a valid measure of the post-detection noise power. However, since the input to the noise gate integrator is AC-coupled, this clamps the integrated noise gate voltage to zero. Thus, determination of the SNR is not straightforward and we discuss it further in Section 2.1.5. It should be noted (see Figure 2.5) that we are suggesting that the fluctuation statistics be computed in the plateau gate region of the mean return. The reason for selecting this region is that the mean return waveform is least rapidly varying in the plateau region (see Appendix 2A for mean waveform computations) and the S&H gate position uncertainty relative to the mean return waveform will least affect the fluctuation statistics here. Also indicated on the DAS diagram for Mode I (Figure 2.5) is the fact that the S&H offset data and the peak transmit power are derived from CDS data.

2.1.2 Mode II: Cross-section (σ^0).— The processing of the CDS data from Mode II is exactly the same as for the CDS data from Mode I (see Figure 2.4). To understand the processing that must be accomplished for the DAS sub-modes of Mode II, it is first necessary to understand how σ^0 is to be extracted from the data. In Appendix 2A, it is shown that σ^0 may be computed from a knowledge of the peak-of-the-mean return which depends on the antenna gain, pattern and pointing angle, altitude, system and propagation* losses and transmitted waveform and power. Thus, if the altimeter measured the peak-of-the-mean return and we knew these other parameters, we could compute σ^0 from the measured data. All of the above parameters can be measured except the peak-of-the-mean return. The actual S-193 hardware measures the mean-of-the-peaks instead of the peak-of-the-means, and thus we must obtain a relation between these two quantities, i.e., the r-factor. This particular problem is discussed more thoroughly in Section 2.1.5 and Appendix 2B. For the present purposes,

*Propagation losses over and above free-space losses.

assume that this problem can be resolved and that we know, for each pointing angle, the relation between the peak-of-the-mean and the mean-of-the-peaks or the r-factor. The data processing diagram in Figure 2.6 illustrates the basic operations which must be accomplished to obtain σ^0 from the data. In DAS-2 through 6, the tracker will not be operating, thus there is no way to compare the computed and measured waveforms. Other than obtaining a relation between the peak-of-the-mean return waveform and the mean-of-the-peaks (the r-factor), data processing for this mode appears to be relatively straightforward.

2.1.3 Mode III: Time correlation.— The processing for the CDS sub-mode data from Mode III is shown in Figure 2.7 and is essentially the same as for Mode I except that the S&H gate and pulse-to-pulse spacing must be accurately known. There is a problem with determining the level offset of the S&H gates. Figure 2.3 shows that in CDS-1 and 4, only the first four or five S&H gates will sample the noise prior to the CDS pulse. Thus, we will not be able to determine a level offset for the last three or four S&H gates. Hopefully, the level offset will be stable enough that offset data from Modes I or II can be used for Mode III.

The general scheme of data processing for the DAS sub-modes of Mode III is shown in Figure 2.8. This mode was designed to provide the opportunity to study pulse-to-pulse correlation as a function of pulse spacing, SNR and pulse length. The transmitter, receiver and scattering surfaces are the primary contributors to pulse-to-pulse correlation effects. From the data available from Mode III, it is not possible to isolate the effects of each of the above factors. From power spectral density computations given in ref. 2.5, we estimate the receiver decorrelation time to be on the order of 15 to 20 ns and 150 to 200 ns for the 10 ns and 100 ns pulse widths, respectively. Unfortunately, there does not appear to be any way to verify these figures from the data available from Mode III; however, since the minimum pulse separation in the dual pulse configuration is one microsecond (μ s), we anticipate that any observable pulse-to-pulse correlation will be a result of scattering surface effects.

In all of the dual-pulse sub-modes of Mode III, four of the S&H gates sample the first pulse, while the other four S&H gates sample the second pulse. After one frame of data (1.04 sec, or about 250 pulse-pairs), the S&H gates are shifted to sample another portion of the return pulses. After sequencing through the appropriate number of S&H gate positions (four for DAS-2,

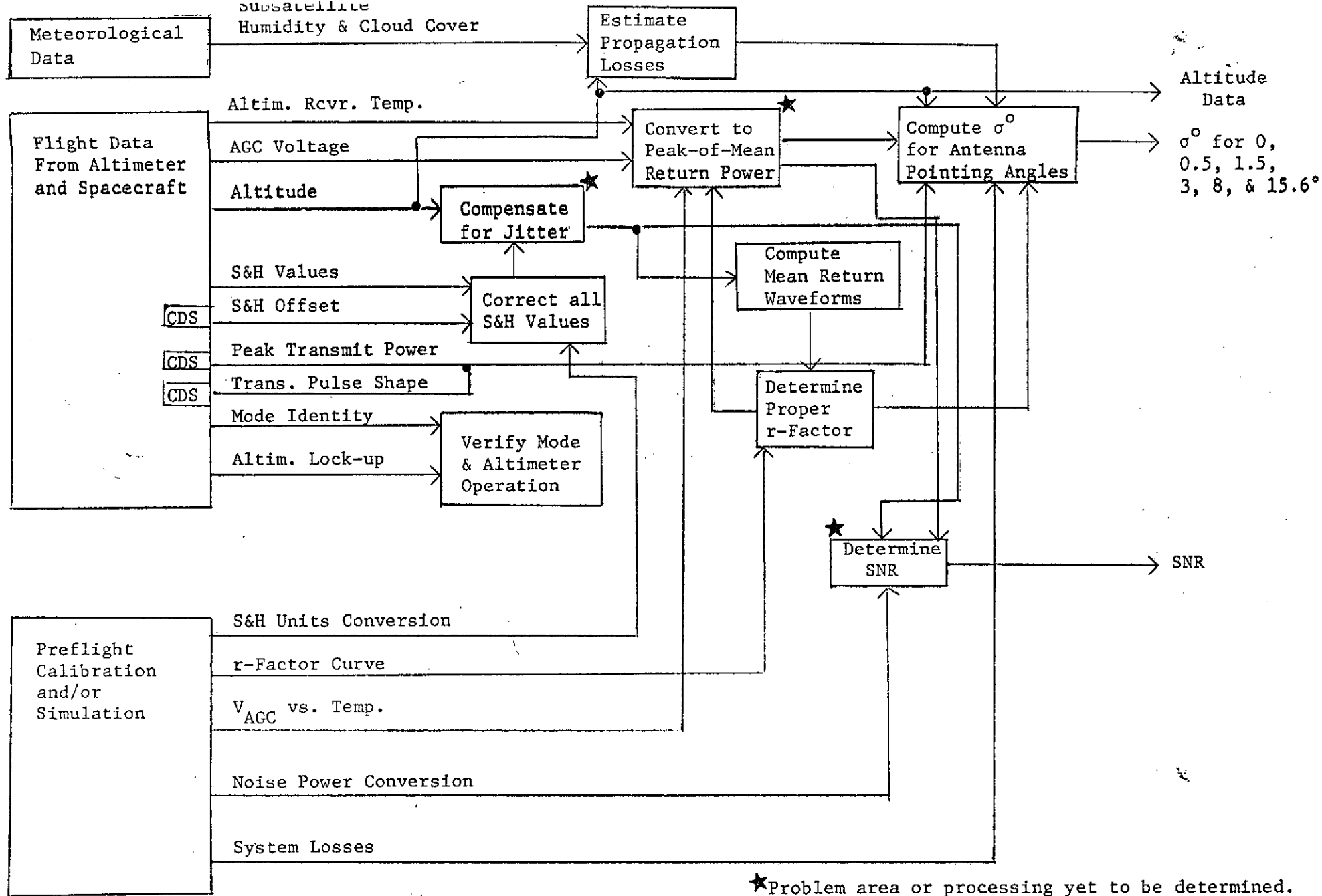


Figure 2.6. Data processing diagram for Mode II, DAS 1-7: note that DAS 2-6 will not provide S&H data.

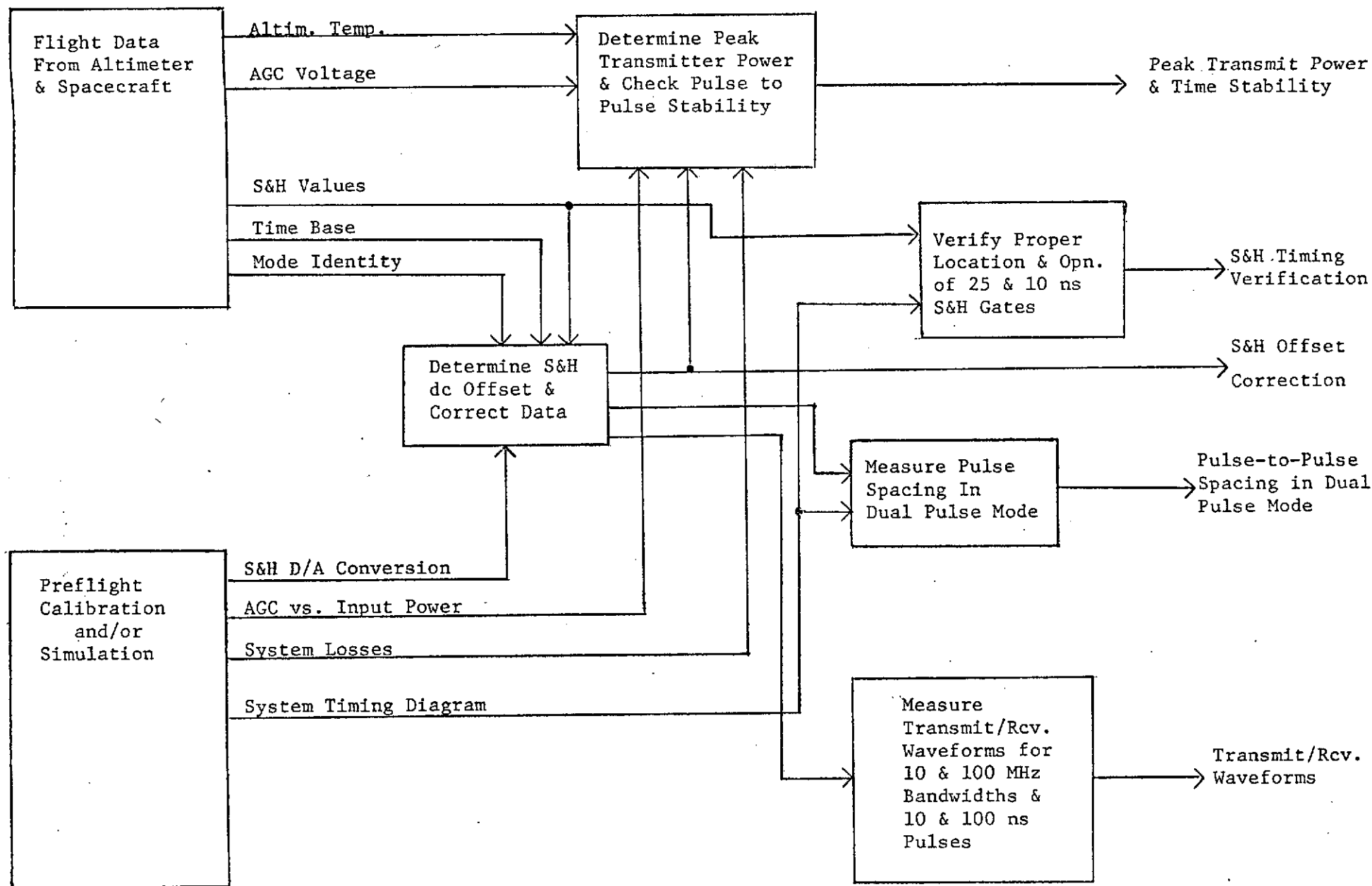


Figure 2.7. Data processing diagram for Mode III, CDS-1, 2, 3, 4, and 5.

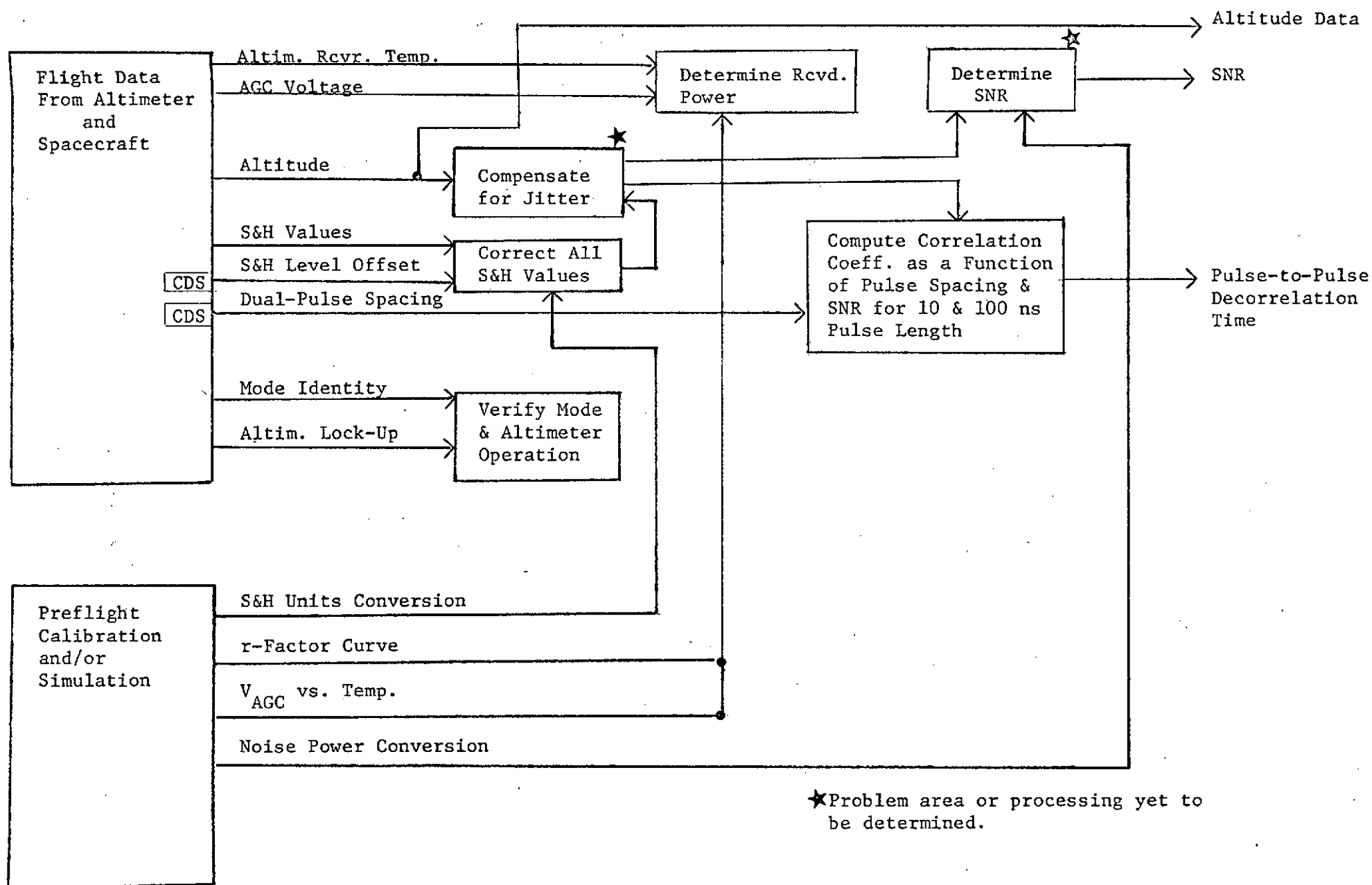


Figure 2.8. Data processing diagram for Mode III, DAS-1, 2, and 3.

eight for DAS-3) for each sub-mode, the pulse-pair spacing is changed. Thus, for each S&H gate position and each pulse-pair spacing, we will have about 250 returns to work with.

A typical sequence of return pulses is shown in Figure 2.8a. The S&H gates are represented by the vertical arrows and are shown to be in the first position (see Figure 2.3 for other typical positions). The pulse-pair spacing is T_p and the pulse-pair period is T (4 ms).

The following notation and discussion are restricted to a single position; the measurement process described is to be repeated for each of the other positions as well. The (local) time origin is taken as zero at the first S&H gate in the first sample set after the position is set. Then the voltages recorded by the S&H gates for the first pulse and the first sample set are (for τ = S&H gate spacing),

$$v_1(0), v_2(\tau), v_3(2\tau), v_4(3\tau),$$

while the voltages recorded for the S&H gates in the second pulse of the first sample set are

$$\tilde{v}_1(T_p), \tilde{v}_2(\tau + T_p), \tilde{v}_3(2\tau + T_p), \tilde{v}_4(3\tau + T_p) .$$

The voltages recorded by the S&H gates for the first and second pulses of the i th sample set are, respectively,

$$v_1((i-1)T), v_2(\tau + (i-1)T), v_3(2\tau + (i-1)T), v_4(3\tau + (i-1)T),$$

and

$$\tilde{v}_1(T_p + (i-1)T), \tilde{v}_2(\tau + T_p + (i-1)T), \tilde{v}_3(2\tau + T_p + (i-1)T), \tilde{v}_4(3\tau + T_p + (i-1)T) .$$

Because of the paucity of S&H values for each pulse, it is not advisable to do a conventional cross-correlation of the first and second pulses. What is really required is the correlation between corresponding S&H gates in the first and second pulses of the pulse-pair. That is, we need to know the correlation between $v_1(0)$ and $\tilde{v}_1(T_p)$, $v_2(\tau)$ and $\tilde{v}_2(\tau + T_p)$, etc.

If we define $\rho(l, T_p)$ as the cross-correlation coefficient* of the l th S&H gate for a pulse-pair spacing of T_p , we have

* $\rho = 0$ implies independence, while $\rho = 1$ implies complete dependence.

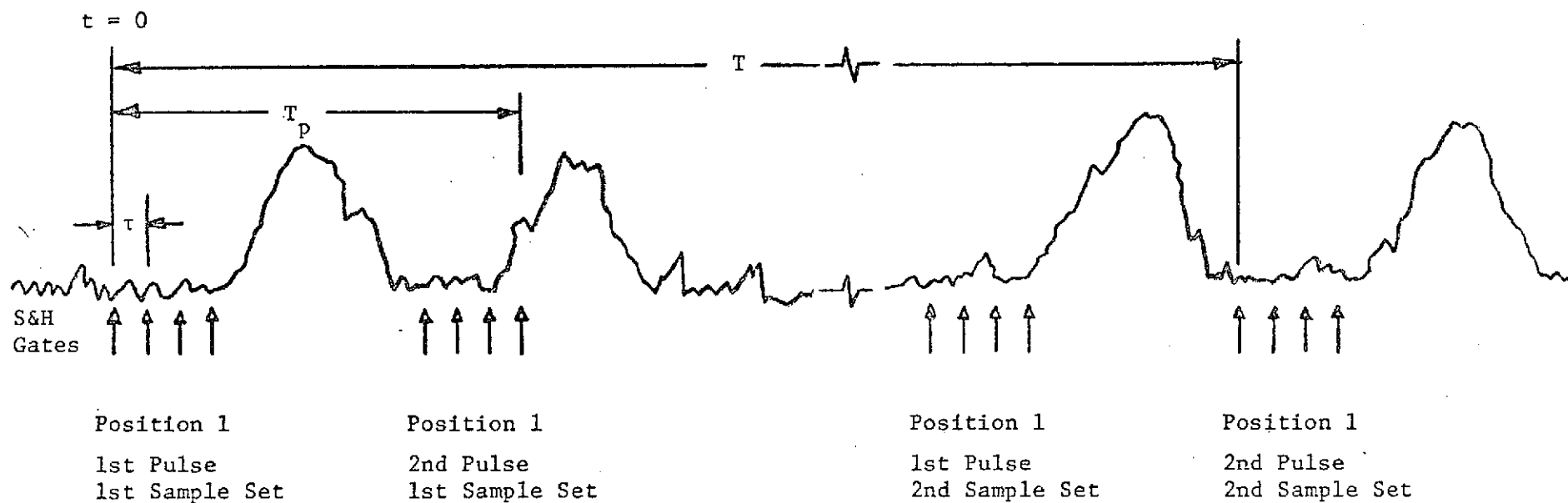


Figure 2.8a. Two typical pulse-pair returns with the S&H gates shown in the first position. Note that of the eight total S&H gates, four are allocated to the first pulse and four are allocated to the second of the pulse-pair.

$$\rho(\ell, T_p) = \frac{\frac{1}{N} \sum_{i=1}^N \left\{ v_{\ell}((\ell-1)\tau + (i-1)T) - \bar{v}_{\ell} \right\} \left\{ \tilde{v}_{\ell}((\ell-1)\tau + T_p + (i-1)T) - \bar{\tilde{v}}_{\ell} \right\}}{\overline{v_{\ell}^2} \overline{\tilde{v}_{\ell}^2}},$$

where \bar{v}_{ℓ} is the mean of the ℓ th S&H gate for N measurements,

$$\bar{v}_{\ell} = \frac{1}{N} \sum_{i=1}^N v_{\ell}((\ell-1)\tau + (i-1)T)$$

and $\overline{v_{\ell}^2}$ is the variance,

$$\overline{v_{\ell}^2} = \frac{1}{N} \sum_{i=1}^N v_{\ell}^2((\ell-1)\tau + (i-1)T).$$

The second-pulse mean, $\bar{\tilde{v}}_{\ell}$, and variance, $\overline{\tilde{v}_{\ell}^2}$, are defined similarly. By expanding terms inside the summations in the expression for $\rho(\ell, T_p)$, one may obtain the following alternative expression:

$$\rho(\ell, T_p) = \frac{\frac{1}{N} \sum_{i=1}^N \left\{ v_{\ell}((\ell-1)\tau + (i-1)T) \right\} \left\{ \tilde{v}_{\ell}((\ell-1)\tau + T_p + (i-1)T) \right\}}{\overline{v_{\ell}^2} \overline{\tilde{v}_{\ell}^2}}$$

$$= \frac{\frac{1}{N^2} \left\{ \sum_{i=1}^N v_{\ell}((\ell-1)\tau + (i-1)T) \right\} \left\{ \sum_{i=1}^N \tilde{v}_{\ell}((\ell-1)\tau + T_p + (i-1)T) \right\}}{\overline{v_{\ell}^2} \overline{\tilde{v}_{\ell}^2}}.$$

This expression for $\rho(\ell, T_p)$, for $\ell = 1, 2, 3$, or 4 , is somewhat more computationally convenient to use than the earlier $\rho(\ell, T_p)$.

In these expressions, N is the total number of pulse-pairs sampled (~ 250) at a given position and pulse-pair spacing. For a given pulse-pair spacing, $\rho(\ell, T_p)$ should be independent of ℓ ; that is, each point on the first pulse and each point on the second pulse which are separated by T_p should yield the same cross-correlation coefficient, independent of jitter. The results of this measurement and calculation process for a given position of the S&H gates will allow us to determine $\rho(\ell, T_p)$ as a function of T_p and consequently to determine how the scattering surface decorrelates. As previously noted, the above description has been for a single position, and carrying out the same procedure for the other positions will yield additional estimates of ρ .

2.1.4 Mode V: Pulse Compression.—As shown in the CDS data processing diagram for Mode V (Figure 2.9), the primary emphasis in this mode is on obtaining data on the pulse shape after the expansion/compression process. The reason for this concern is that we do not want to confuse hardware problems such as time-sidelobes with sea-state effects. In this study, it would have been desirable to compute mean return waveforms for the 10 ns pulse compression case as was done for the 100 ns pulse length case (see Appendix 2A), since we would then have some estimate of the effect of the time sidelobes on the mean return waveform. However, time was not available to do this. If relatively high time-sidelobes do appear in the pulse as recorded by the CDS-2 sub-mode, it is not entirely clear at this time how best to correct the data from the DAS-2 sub-mode to eliminate this effect. The data currently available on the pulse compression network do not appear to be extensive enough to obtain the transfer function of the system. Therefore, it does not seem feasible to consider a deconvolution process for correcting the data.

The data processing for the DAS sub-modes of Mode V is diagrammed in Figure 2.10. As with some of the other modes, the problems of SNR and tracker variance determination are present. Obtaining the proper level offset compensation of the S&H gates for all of the DAS sub-modes may be difficult because time sidelobes may fall into the region where we would normally expect just noise (see Figure 2.2). Hopefully, this mode will provide a more favorable SNR with which to estimate sea state from the mean return waveform.

2.1.5 Special Problems to be Resolved.—Throughout the previous sections of this chapter we have made numerous references to certain problems which have a direct impact on the experimental data that may be obtained from the radar altimeter. The purpose of this section is to present detailed discussions of these problem areas and to recommend possible solutions.

SNR Determination: For purposes of design of future sensors, and validity of S-193 data, it is most important that the SNR be known in each of the operating modes. In order to obtain this ratio, it is necessary to measure the noise power in the receiver prior to the arrival of the scattered pulse. Originally, it was thought that such information could be derived directly from the S&H gates which are positioned in the noise gate. In order to maintain amplifier stability (ref. 2.1), GE inserted a large blocking capacitor between the output of the video amplifier and the S&H gates input. Unfortunately, this capacitor converts the noise voltage (at the input to the S&H gates) to a zero-mean process, and the mean

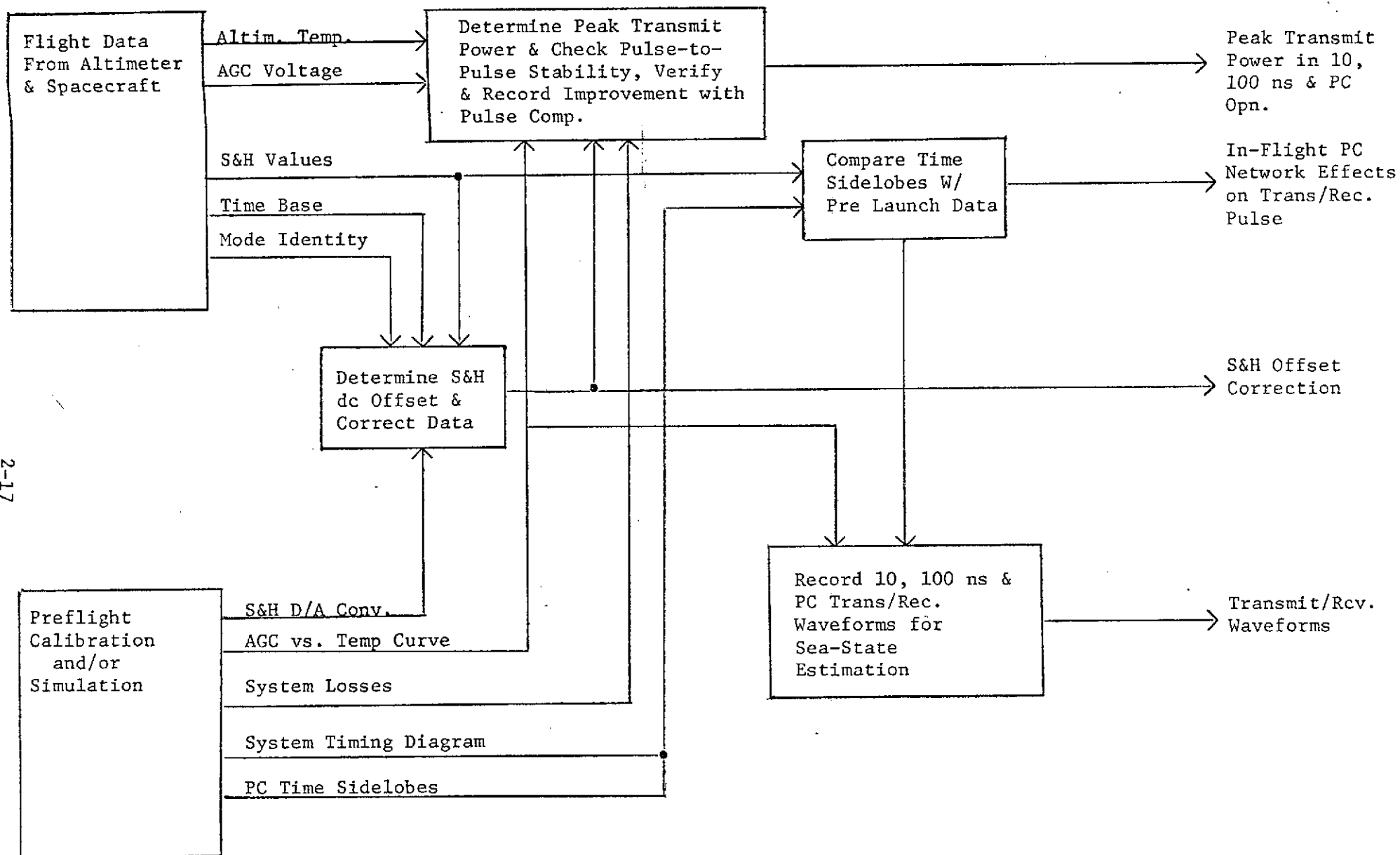


Figure 2.9. Data processing diagram for Mode V, CDS-1, 2, and 3.

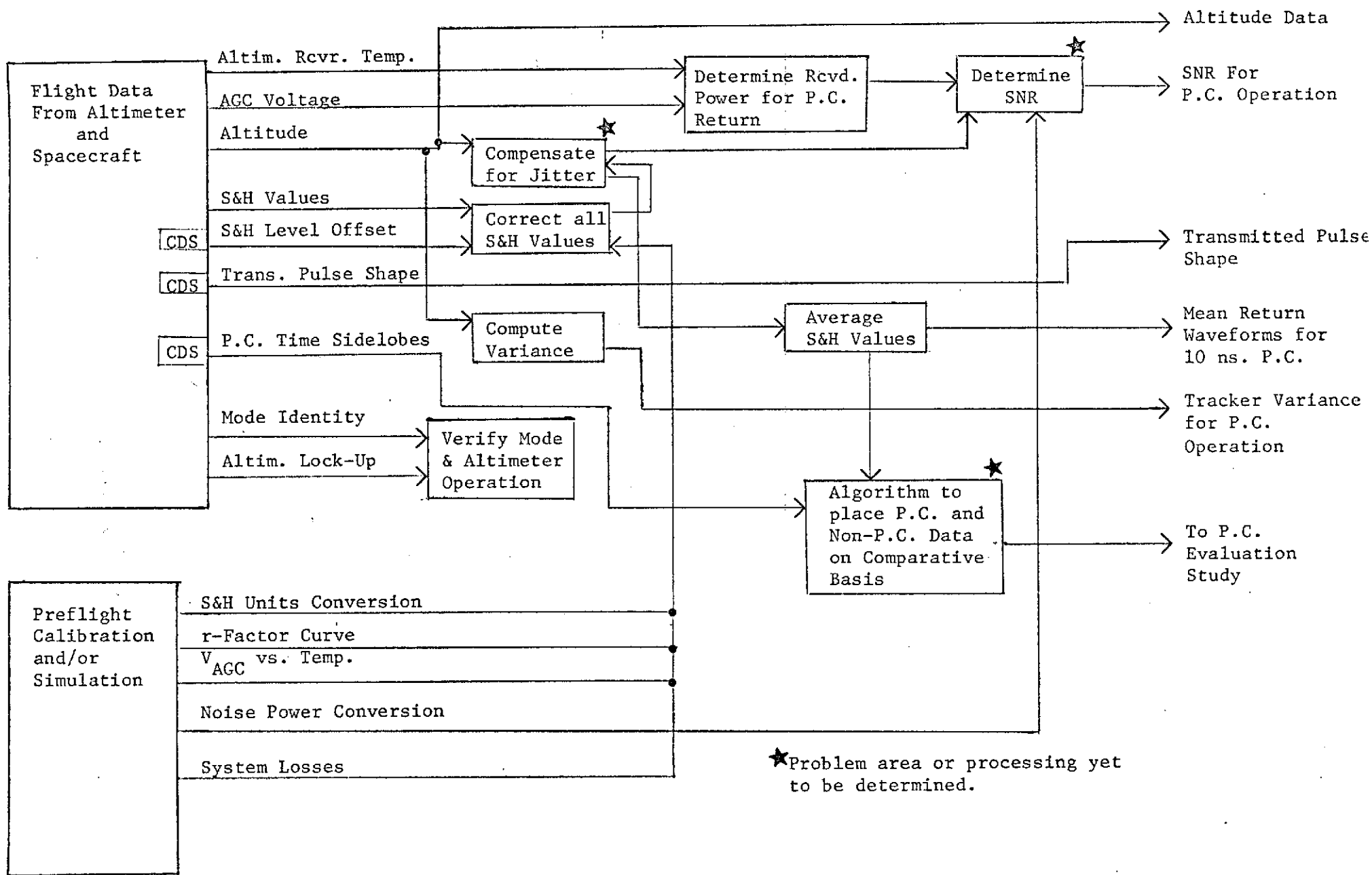


Figure 2.10. Data processing diagram for Mode V, DAS-1, 2, and 3.

of the S&H gate values is no longer proportional to the noise power. While we can construct histograms for the noise voltage recorded by the S&H gates, there is no direct measurement which can be made to determine the mean noise power.

In order to obtain an approximation to the noise power, we will use the results of ref. 2.5. That is, assuming that the noise into the IF filter is narrow-band Gaussian with zero mean, we can compute the noise power as recorded by the S&H gates. This process will yield a relationship between the post-IF noise power and the noise power as recorded by the S&H gates (after the blocking capacitor). Through this relationship we can relate the actual noise power as measured by the S&H gates to the post-IF noise power. The basic assumption in this process is that we know the characteristics of the various receiver components, i.e., the IF and video filters, the detector and the blocking capacitor. Thus, we see that accurate measurements of these receiver characteristics are essential to the qualification of this process.

The important parts of the receiver are shown in Figure 2.11. It should be noted that the IF and video filter bandwidths scale down by a factor of ten when switching from 10 to 100 ns pulse length operation, thus the results should apply to either case. We assume that the noise into the IF filter is flat over a bandwidth large compared to the IF filter bandwidth and has a spectral amplitude of N_0 watts/hertz. We also assume that the noise has a Gaussian density with zero mean. The power spectral density (psd) of the noise is taken to be

$$\phi_n(\omega) = \begin{cases} N_0 & |\omega| \leq \omega_1 \\ 0 & |\omega| > \omega_1 \end{cases}$$

The post-IF psd is given by

$$\phi_{IF}(\omega) = \phi_n(\omega) |H_{IF}(\omega)|^2,$$

where $H_{IF}(\omega)$ is the transfer function of the IF filter.

Since $2\omega_1$ is assumed to be much greater than the IF filter bandwidth,

$$\phi_{IF} \approx N_0 |H_{IF}(\omega)|^2.$$

The noise power out of the IF filter is N_{IF} , where

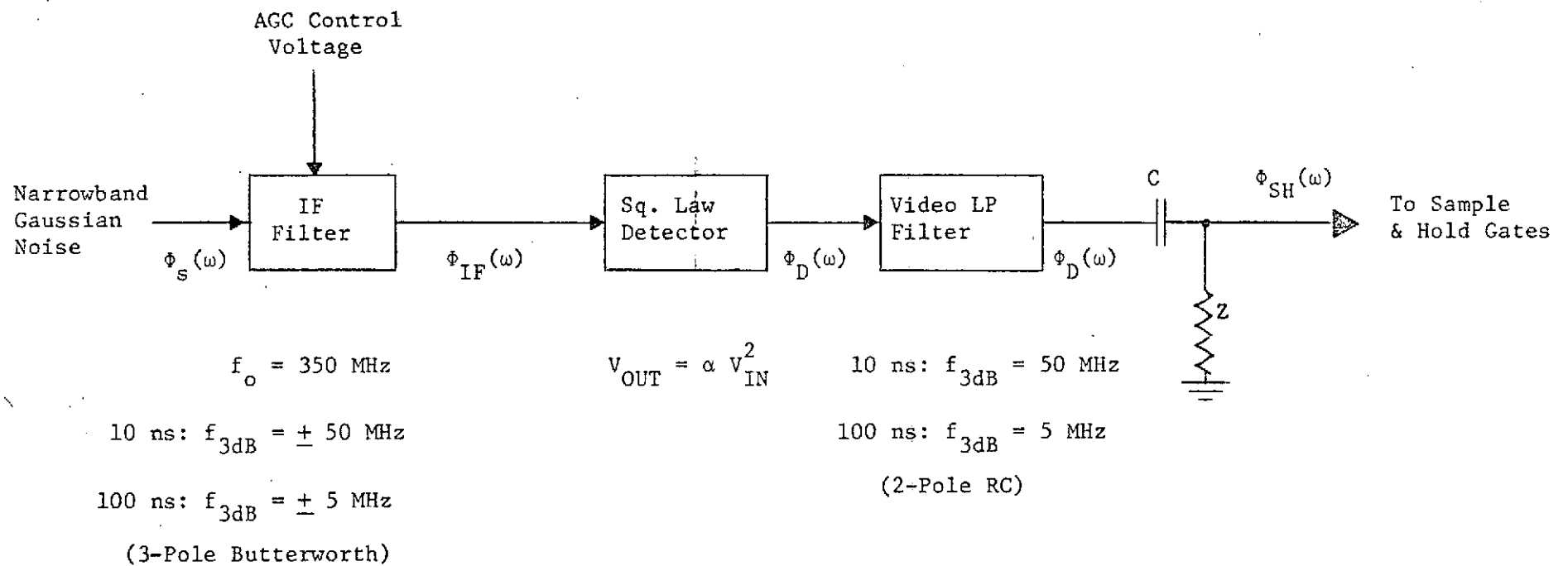


Figure 2.11. Receiver configuration for noise power computation.

$$N_{IF} = \frac{N_o}{2\pi} \int_{-\infty}^{\infty} |H_{IF}(\omega)|^2 d\omega \quad (2-1)$$

The psd at the output of the detector is given by

$$\phi_D(\omega) = 2\alpha^2 \left\{ \phi_{IF}(\omega) * \phi_{IF}(\omega) \right\} + \alpha^2 N_{IF}^2 \delta(\omega) \quad (2-2)$$

where the symbol * denotes convolution.

The psd at the input to the S&H gates is

$$\begin{aligned} \phi_{SH}(\omega) = & 2\alpha^2 |H_V(\omega)|^2 |H_{CZ}(\omega)|^2 \left\{ \phi_{IF}(\omega) * \phi_{IF}(\omega) \right\} \\ & + 2\alpha^2 N_{IF}^2 |H_V(\omega)|^2 |H_{CZ}(\omega)|^2 \delta(\omega) \quad , \end{aligned}$$

where $H_V(\omega)$ is the transfer function of the video filter and $H_{CZ}(\omega)$ is the transfer function of the ZC-circuit at the output of the video filter. The noise power as recorded by the S&H gates is given by

$$N_{SH} = \frac{1}{2\pi} \int_{-\infty}^{\infty} \phi_{SH}(\omega) d\omega \quad (2-3)$$

or

$$N_{SH} = \frac{2\alpha^2 N_o^2}{2\pi} \int_{-\infty}^{\infty} \left\{ |H_V(\omega)|^2 |H_{CZ}(\omega)|^2 \left[|H_{IF}(\omega)|^2 * |H_{IF}(\omega)|^2 \right] \right\} d\omega \quad (2-4)$$

In obtaining (2-4) we have used the fact that $|H_{CZ}(0)| \equiv 0$. Using (2-1), we can solve (2-4) for N_{IF} in terms of N_{SH} , i.e.,

$$N_{IF} = \frac{\sqrt{N_{SH}}}{2\sqrt{\pi}\alpha} \frac{\int_{-\infty}^{\infty} |H_{IF}(\omega)|^2 d\omega}{\left\{ \int_{-\infty}^{\infty} |H_V(\omega)|^2 |H_{CZ}(\omega)|^2 \left[|H_{IF}(\omega)|^2 * |H_{IF}(\omega)|^2 \right] d\omega \right\}^{1/2}} \quad (2-5)$$

Equation (2-5) is the desired relation between the noise power at the S&H gates and the post-IF noise power. Its accuracy depends almost entirely upon how well we know the various transfer functions. The transfer function about which we have no knowledge is $H_{CZ}(\omega)$, and we recommend that this be measured on the S-193 altimeter breadboard. It should be noted that since the S&H gates are sampling

zero mean noise, N_{SH} is just equal to the variance of the voltage recorded by any one S&H gate in the noise region prior to the arrival of a return pulse.

RF Hardware Losses: One of the primary purposes of the CDS sub-modes is to provide a check on the peak transmitted power. This check is implemented as shown in Figure 2.12. A switch between the transmitter and the coupling circulator is activated and the transmitted power* is routed through a fixed attenuator and then into the front end of the receiver. If the loss in the attenuator is L_α and the loss through the switch and waveguide connecting the transmitter (through the attenuator) and the receiver is L'_α , the peak power into the receiver is $\hat{P}_t / (L_\alpha L'_\alpha)$. Compensating for the known loss through the attenuator would lead to a measured transmitter power of P_t / L' . Unfortunately, in a DAS configuration the actual loss through the waveguide and circulator hardware will be $L_{BA} L_{AC} = L_T^* L_R^*$ (see Figure 2.12).

In the computations for σ^0 , we need the ratio \hat{P}_t / L where L is the actual attenuation between the output of the transmitter and the input to the antenna terminals plus the attenuation between the antenna terminals and the receiver input, i.e., $L = L_T^* L_R^*$. Data from the CDS sub-modes will yield \hat{P}_t / L'_α rather than $\hat{P}_t / L_T^* L_R^*$ as shown above. Thus, there exists a very definite need for a pre-flight measurement of the quantities L'_α , L_T^* and L_R^* , for only then can we adequately correct the CDS data. It should be noted that any difference between L_α and $L_T^* L_R^*$ will be directly reflected in the computation of σ^0 (see Appendix 2A). While this may seem to be a minor point, it could conceivably cause an error in σ^0 of 1 to 2 dB depending on the ratio $L'_\alpha / L_T^* L_R^*$. To date, we have seen no GE calibration or qualification data which provide a measure of any of these required losses.

r-Factor Determination: As we noted in the discussion of Mode II (Section 2.1.2), before σ^0 can be extracted from the measured data, an accurate study of the relation between the mean-of-the-peaks of the return (AGC voltage) and the peak-of-the-mean return (required to compute σ^0) must be accomplished. The first step in obtaining the relation is to compute the mean return waveforms and, hence, the theoretical peak-of-the-mean return. This computation must be accomplished because the relation between the two quantities is highly dependent upon the amplitude and the shape of the mean return waveform. A computation of the mean return waveform is given in Appendix 2A for DAS 1 through 7 of Mode II.

GE made some preliminary computations of the r-factor (ref. 2.3), but these calculations were necessarily approximate since some of the parameters used were

*Of peak amplitude \hat{P}_t .

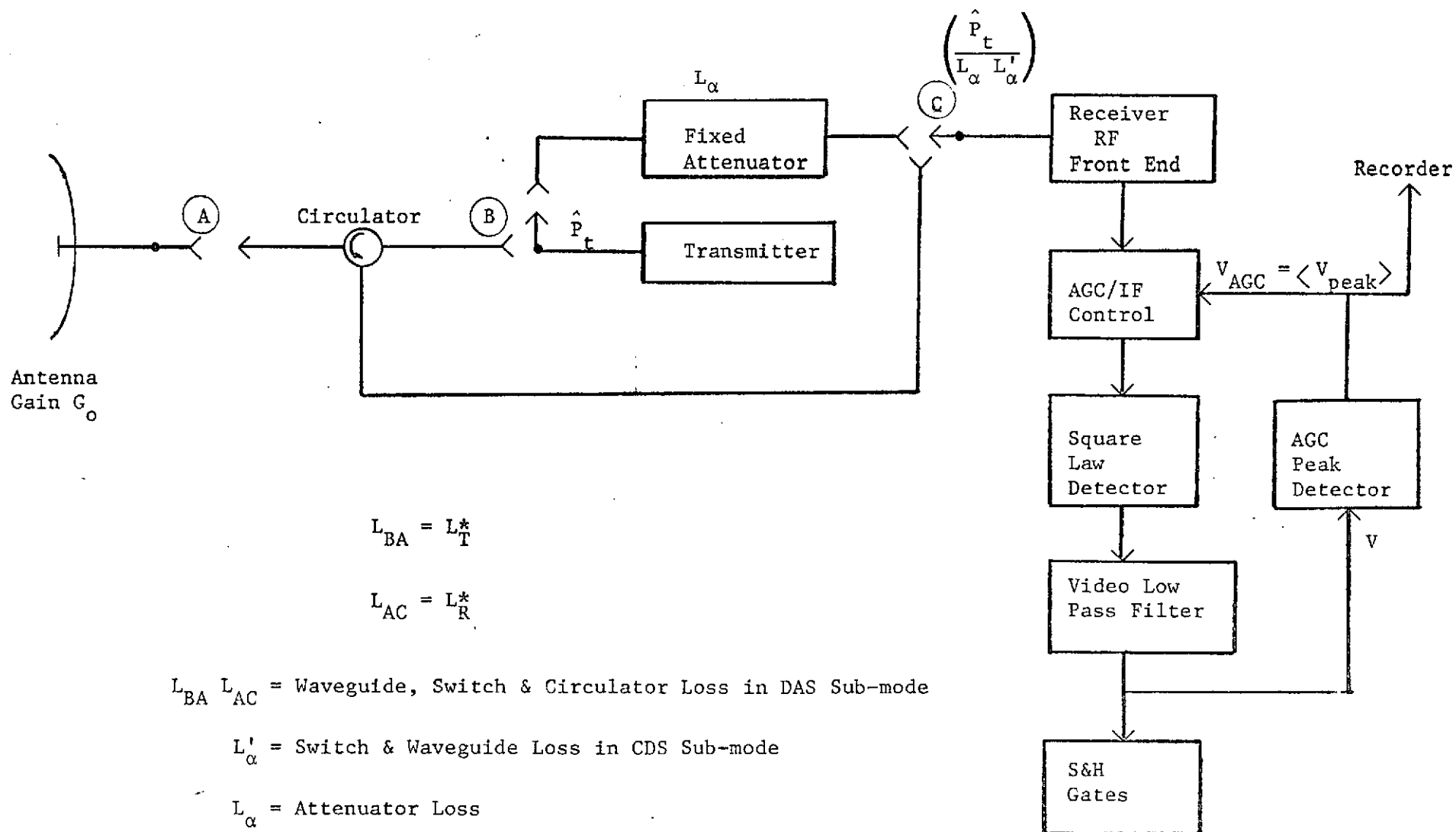


Figure 2.12. S-193 altimeter configuration during measurement of peak transmitted power and pulse shape (CDS Sub-mode).

not Skylab parameters. We performed an analog/digital computer simulation of the altimeter hardware in an attempt to verify GE's results. The results and details of the simulation are given in Appendix 2B. Although the simulation effort was not complete in all details, it clearly showed that the presently available data are questionable. We therefore recommend a much more detailed analysis for the determination of the r-factor for all pointing angles of the antenna. It is essential that this simulation effort be accomplished before the Skylab launch data, for if we do not know the r-factor, we cannot determine if Mode II is providing reasonable values of σ^0 . That is, there will be no way we can obtain "quick-look" data on σ^0 from the Mode II measurements. A block diagram of how the r-factor can be determined by simulation is shown in Figure 2.13, however, hardware measurements are strongly recommended.

2.2 Altimeter Experimentation Data Flow

The data processing diagrams presented in Section 2.1 were primarily directed toward calibrating the data from the S-193 altimeter. How the S-193 altimeter data are used and what results are sought are major areas of concern. It is also essential that some decision be made on what organization is to be responsible for the various areas of data processing.

This section presents a data processing and usage chart which attempts to answer some of the above-stated questions. Also presented in this section is the processing which must be accomplished in order to obtain a "quick look" value for σ^0 from the data.

2.2.1 Data Flow and Processing Diagram.—Construction of a data flow block diagram for the S-193 altimeter involved establishment of certain ground rules. These so-called ground rules were based either on known facts or on our estimate of certain situations. Using these criteria, we established the following guidelines for preparing the S-193 altimeter data flow diagram:

- a. data inputs would comprise only the following:
 - S-193 altimeter data,
 - pre-flight calibration and/or simulation data,
 - ground truth data, and
 - spacecraft tracking data;
- b. NASA-MSC (Houston) in conjunction with NASA-Wallops Station would:
 - verify proper altimeter operation,
 - accomplish "quick-look" data processing,

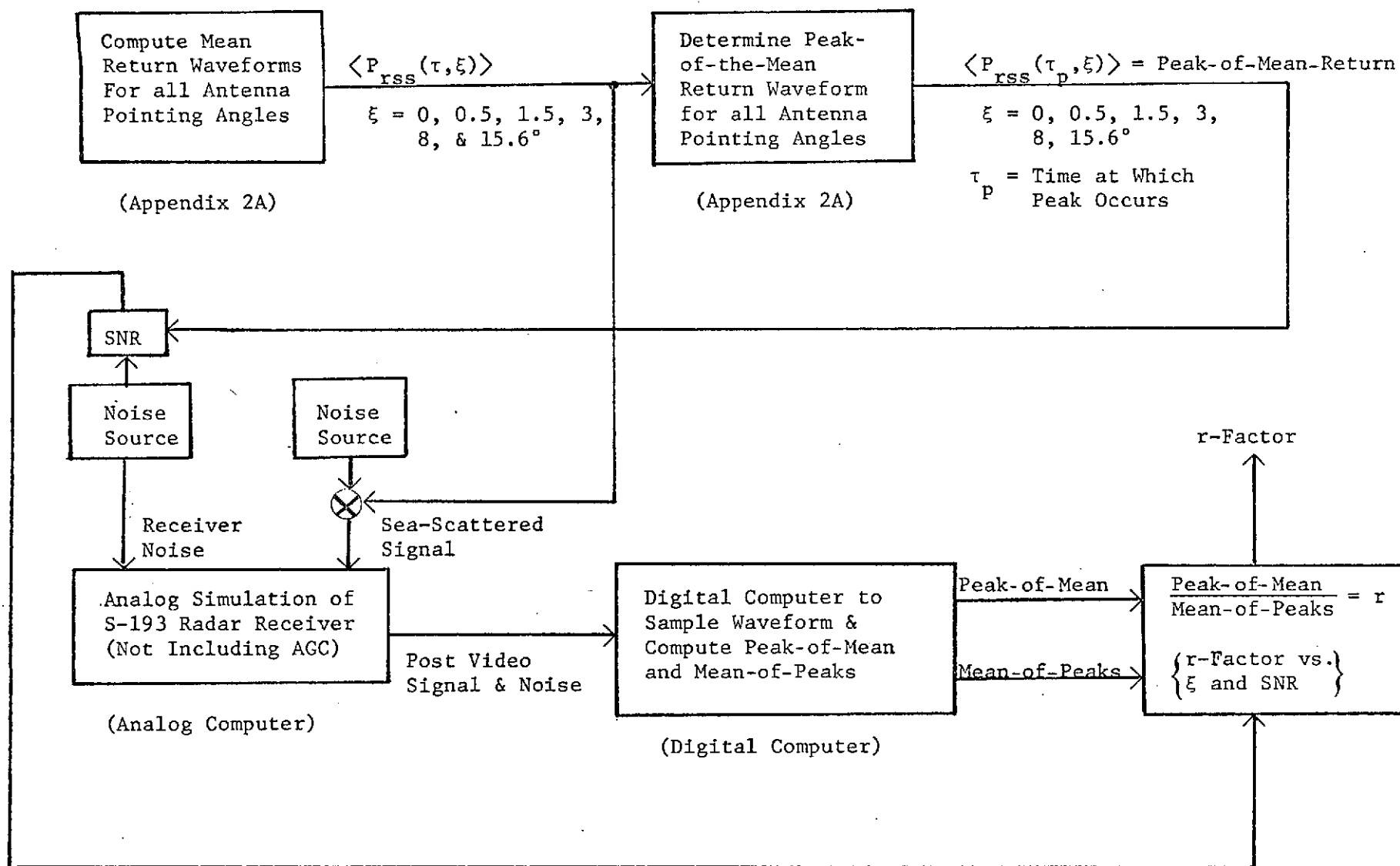


Figure 2.13. Block diagram of how r-factor simulation could be configured.

perform all engineering units conversion,
distribute standardized data tapes to experimenters,
accomplish basic data calibration and correction,*
collect and refine ground truth data, and
distribute corrected S-193 and ground truth data to the
experimenters;

- c. the S-193 altimeter experimental programs would be:
sensor technology,
sea-state estimation (EREP),
altimetry, and
terrain scattering (EREP).

In addition, based on available information, we assumed that the outputs from the S-193 experimental programs would be as follows:

- a. sensor technology:
pulse compression evaluation,
tracker bias determination,
evaluation of tracker performance versus SNR,
evaluation of tracker averaging effects, and
estimation of decorrelation time of the scattering process;
- b. sea-state estimation (EREP):
 σ^0 determination,
sea-state estimation from σ^0 ,
sea-state estimation from mean waveform smearing, and
comparison of σ^0 and waveform sea-state estimation techniques;
- c. altimetry:
geoidal feature extraction, and
determination of sea-state effects through radar-derived pdf of
waveheight;
- d. terrain scattering (EREP):
measurement of σ^0 from various terrains, and
determination of specular scattering effects on the altimeter.

Figure 2.14 illustrates how and by which experimental program the S-193 altimeter data will be analyzed. Also shown are the ground truth data requirements which are based on the goals of the EREP programs. The terrain scattering and altimeter program were left blank since it is not known how the data are to be analyzed.

*To include the processing as indicated in the charts in Section 2.1.

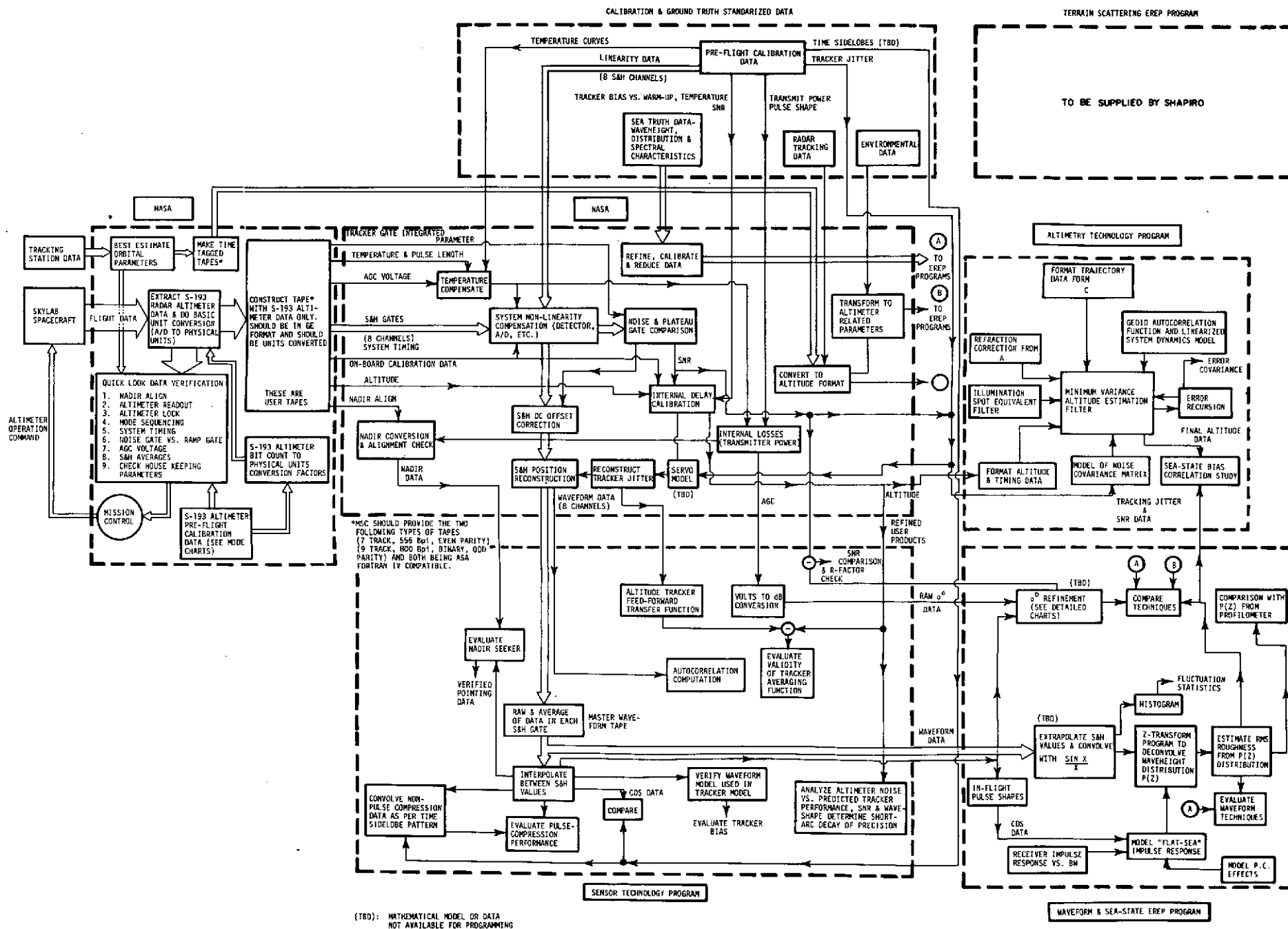


Figure 2.14. S-193 Altimeter data flow diagram.

2.2.2 Quick Look Data Processing For σ^0 .— While most of the data processing in Figure 2.14 will be accomplished post-mission, there is one set which must be performed soon as the data are available. In order to determine if the S-193 altimeter is operating properly and also to plan the next phase of the mission, NASA-MSC must have the capability to accomplish "quick-look" processing of the data. From our analysis of the situation, Mode II (σ^0) appears to require the least amount of data processing since many of the unknowns can be determined from "look-up" tables. In this section we will present a means for obtaining σ^0 from Mode II data and look-up tables.

It is shown in Appendix 2A that the peak of the mean return power is given by

$$\langle P_{\text{rss}}(\tau_p, \xi) \rangle = \left[\frac{\hat{P}_t}{L_p L_T^* L_R^*} \right] \left[\frac{G_o^2 \lambda^2}{(4\pi)^3 h^2} \right] F(h, \zeta_m, \xi, \alpha, \tau_p) \sigma^0(\xi) \quad (2-5)$$

where

τ_p = Time at which peak of the mean return occurs,

G_o = Antenna boresight power gain,

\hat{P}_t = Peak transmitted power,

$L_T^* L_R^*$ = RF losses due to the waveguide hardware between the transmitter output and antenna input and the antenna output and the receiver input, respectively,

L_p = Propagation loss over and above free space loss,

λ = RF wavelength,

h = Altimeter altitude above the surface of the earth

α = A parameter determined by the width of the pulse recorded in Mode II, CDS-1 (≈ 2100),

ζ_m = rms waveheight of the sea surface,

ξ = Pointing angle of the antenna relative to nadir,

$F(h, \zeta_m, \xi, \alpha, \tau_p)$ = An integral which will be provided in a look-up table,

and $\sigma^0(\xi)$ is the desired backscattering cross section at an angle ξ off nadir. The digitized AGC voltage may be converted to $\langle P_{\text{rss}}(\tau, \xi)_{\text{peak}} \rangle$ through the use of GE-provided look-up tables (ref. 2.4). The peak-of-the-mean return power in (2-5) may be computed from

$$\langle P_{\text{rss}}(\tau_p, \xi) \rangle = r(\xi) \langle P_{\text{rss}}(\tau, \xi)_{\text{peak}} \rangle, \quad (2-6)$$

where $r(\xi)$ is known for $\xi = 0^\circ, 0.5^\circ$ and 1.5° from Appendix 2B and as yet is undetermined for $\xi = 3, 8$ and 15.6° . In Mode II, CDS-1 the AGC measurement will be related by GE look-up tables* to $(\hat{P}_t / L_\alpha L'_\alpha)$ where $L_\alpha = 119$ dB and L'_α is a quantity yet to be measured (see Section 2.2.5). For the present, we shall assume that $L'_\alpha \approx L_T^* L_R^*$, but this assumption must be verified by measurements on the engineering model.

The parameters measured in the altimeter and converted by GE look-up tables are

$$[M_1(\xi)] = \langle P_{\text{rss}}(\tau, \xi)_{\text{peak}} \rangle \quad (2-7)$$

and

$$[M_2] \approx \frac{\hat{P}_t}{L_\alpha L_T^* L_R^*} \quad (2-8)$$

Substituting (2-8), (2-7) and (2-6) in (2-5) yields the following;

$$r(\xi) M_1(\xi) = [M_2 L_\alpha] \left\{ \frac{G_o^2 \lambda^2}{(4\pi)^3 h^2} \right\} F(h, \zeta_m, \xi, \alpha, \tau_p) \sigma^0(\xi) \quad (2-9)$$

Solving (2-9) for $\sigma^0(\xi)$ in decibels gives

$$[\sigma^0(\xi)]_{\text{dB}} = [M_1(\xi)]_{\text{dB}} - [M_2]_{\text{dB}} - 119 - \left\{ \frac{1}{r(\xi)} \frac{G_o^2 \lambda^2}{(4\pi)^3 h^2} F(h, \zeta_m, \xi, \alpha, \tau_p) \right\}_{\text{dB}}$$

*A measurement of receiver temperature is also necessary to insure that the correct look-up table is used.

The last factor in the above equation can be computed and provided in a look-up table, while the first two quantities are the result of measurements (AGC A/D converter output) and a look-up table (AGC A/D converter output vs. input power and receiver temperature). If we denote the last two terms in the above equation by Q , we have

$$[\sigma^0]_{\text{dB}} = [M_1(\xi)]_{\text{dB}} - [M_2]_{\text{dB}} - [Q]_{\text{dB}} \quad (2-10)$$

The complete processing necessary to obtain "quick-look" values of σ^0 is shown in block diagram form in Figure 2.15. No requirement for ζ_m , the rms waveheight, has been shown since computations (Appendix 2A) have shown that $F(h, \zeta_m, \xi, \alpha, \tau_p)$ is insensitive to ζ_m for $0 \leq \zeta_m \leq 2$ meters. Values for $F(h, \zeta_m, \xi, \alpha, \tau_p)$ may be determined from curves presented in Appendix 2A for an altitude of 235 nautical miles and a measured α of 2100.

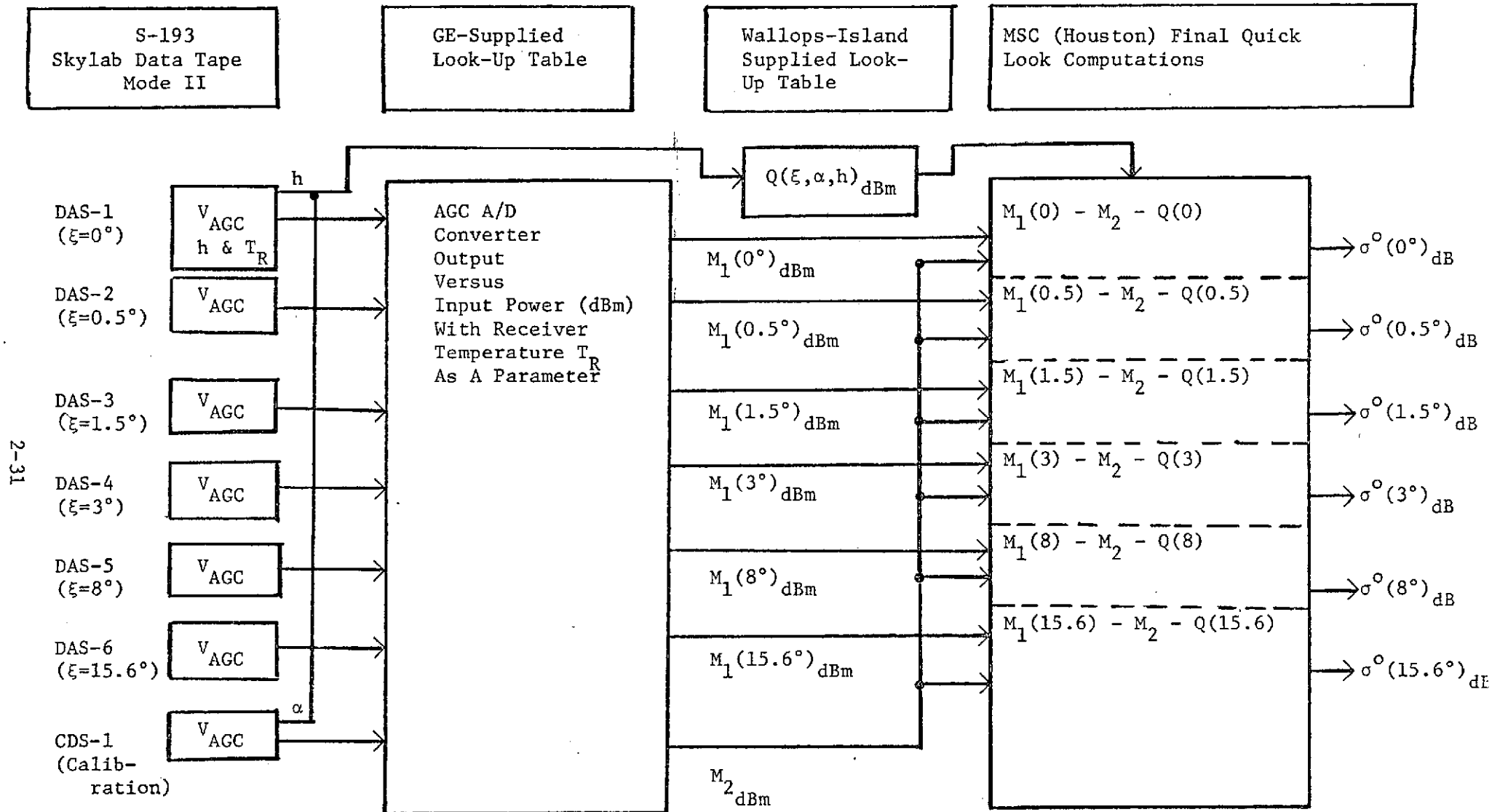


Figure 2.15. Data processing necessary to determine "quick-look" values for $\sigma^0(\xi)$, $\xi = 0, 0.5, 1.5, 3, 8$, and 15.6° .

REFERENCES

- 2.1 Hofmeister, E. L., Private Communications, December, 1972.
- 2.2 Steenson, B. L. and N. C. Stirling, "The Amplitude Distribution and False-Alarm Rate of Filtered Noise," Proc. of IEEE, Vol. 52, pp. 42-55, January, 1965.
- 2.3 Lambert, R., "Automatic Gain Control Loop Calibration Curve Analysis," G. E. System Tech. Memo., STM 2-3-LA, GE Utica, New York, February, 1971.
- 2.4 "S-193 Microwave Radiometer/Scatterometer Altimeter," Calibration Data Report, Vol. 1B, Contract No. NAS9-11195, General Electric Company, October, 1972.
- 2.5 "A Study of the Capabilities of the Geodetic Satellite Altimeter to Measure Ocean Surface Characteristics," Final Report, Contract No. NASW-1909, Research Triangle Institute, April, 1970.

APPENDIX 2A

MEAN RETURN WAVEFORM COMPUTATION FOR MODE II

The primary purpose of Mode II is to provide data on σ^0 , the back-scattering cross-section of the ocean's surface per unit area of scattering surface. To obtain σ^0 from the data provided by Mode II, it is first necessary to compute both the shape and amplitude of the average back-scattered pulse. According to the linear scattering theory (ref. 2A1), the average or mean return waveform is a convolution of the following functions:

- (1) transmitted pulse waveform,
- (2) flat sea impulse response,
- (3) radar observed wave height distribution, and
- (4) radar receiver impulse response.

The flat sea impulse response, above, includes the antenna pattern and also variations of σ^0 with the angle of incidence. Since the convolution operation is both commutative and distributive, we are at liberty to regroup the above convolutions in any desired order. In particular, the convolution of (1) and (4) is easily seen to be the waveform as recorded by the Sample and Hold (S&H) gates in Mode II, CDS-1. Using the pulse shape as measured and calibrated by GE (ref. 2A2, page 6-86) plus the fact that both the S&H word count-to-voltage conversion* (ref. 2A2, pages 6-38 to 6-85) and the detector power-to-voltage conversion are linear, the normalized pulse shape was found to be nearly Gaussian and of the form

$$P(t_r) \approx \frac{\hat{P}_t}{L} \frac{1}{\sqrt{\pi\alpha}} e^{-\frac{(t_r - 100)^2}{\alpha}} \quad (2A1)$$

where $\alpha = 2100$ for the time t_r measured in nanoseconds, \hat{P}_t is the peak transmitted power and L is the system loss.

*At +25°C and over a word count range of 130 to 70 counts.

For the 100 ns pulse length used in Mode II, it is reasonable to assume that the radar observed wave height distribution is Gaussian. Such higher order effects as skew and kurtosis may be significant in the case of 10 ns pulse scattering, but the 100 ns return is not expected to be sensitive to such small perturbations. Therefore for Mode II, the wave height distribution $p(z)$, where z is the height above the mean plane ($z=0$), is taken to be,

$$p(z) = \frac{1}{\sqrt{2\pi\zeta_m^2}} e^{-\left(\frac{z^2}{2\zeta_m^2}\right)} \quad (2A2)$$

where ζ_m^2 is the mean-square wave height. $t_r = 0$ in equation (2A1) corresponds to the time at which the leading edge of the transmitted pulse, scattered from the surface at a height of $h-z$ below the radar, enters the receiver. If the variable t denotes the time relative to transmission of the pulse ($t=0$), then $t_r = 0$ corresponds to $t = 2(h-z)/c$. Converting from t_r in (2A1) to t yields*

$$P\left(t + \frac{z}{c}\right) = \frac{\hat{P}_t}{L} \frac{1}{\sqrt{\pi\alpha}} e^{-\frac{1}{\alpha} [t - 2(h-z)/c - 100]^2} \quad (2A3)$$

The effect of sea-state roughness upon the transmitted received waveform may be found from the following convolution:

$$P_{ss}(t) = \int_{-\infty}^{\infty} P(t + z/c) p(-z) dz \quad (2A4)$$

Letting $\tau = t - 2h/c$, i.e., letting τ be the incremental two-way ranging time relative to the mean height h , and accomplishing the integration in (2A4) yields

$$P_{ss}(\tau) = \frac{\left(\frac{\hat{P}_t}{L}\right)}{\sqrt{\pi\alpha} \sqrt{1 + \frac{8\zeta_m^2}{\alpha c^2}}} e^{-\frac{1}{\alpha} \left[1 - \frac{1}{1 + \frac{\alpha c^2}{8\zeta_m^2}}\right] (\tau - 100)^2} \quad (2A5)$$

*To be consistent with (2A1), t should be in units of nanoseconds and $c = 0.3$ meters/nanoseconds.

We now must determine the flat-sea impulse response and convolve this result with (2A5) to find the complete mean return waveform.

It has been previously shown that the flat-sea impulse response is given by ref. 2A3

$$P_r(\tau, \xi) = \frac{G_o^2 \lambda^2}{L_p (4\pi)^3} \int \frac{\delta(t - \frac{2r}{c}) f^4(\theta, \omega) \sigma^o(\psi)}{r^4} dA \quad (2A6)$$

scattering
surface area

where;

L_p = Propagation loss over and above free-space loss,

G_o = Boresight power gain of the transmitting/receiving antenna,

λ = rf-wavelength,

$\delta(t - \frac{2r}{c})$ = Delta function,

$f(\theta, \omega)$ = Antenna voltage pattern normalized to a maximum amplitude of unity,

r = Distance from the antenna to the incremental area dA on the scattering surface, and

$\sigma^o(\psi)$ = Backscattering cross-section of the sea surface per unit area of scattering surface.

The angle between the boresight axis of the antenna and the nadir axis is ξ , while $\tilde{\phi}$ is the azimuth angle on the scattering surface of the antenna boresight axis. θ is the angle between the boresight axis and a line extending from the antenna to the elemental surface area dA , and ω is the projection of the pattern azimuth angle on the scattering surface. The other various geometrical parameters are defined in Figure 2A1. The antenna pattern is a function of the angular coordinates θ and ω , while the incremental area dA is a function of ρ and ϕ , i.e. $\rho d\rho d\phi$. Thus, it is necessary to determine θ and ω in terms of ρ and ϕ . It can be easily shown that

$$\cos \theta = \frac{\cos \xi + \frac{\rho}{h} \sin \xi \cos(\phi - \tilde{\phi})}{\sqrt{1 + (\rho/h)^2}} \quad (2A7)$$

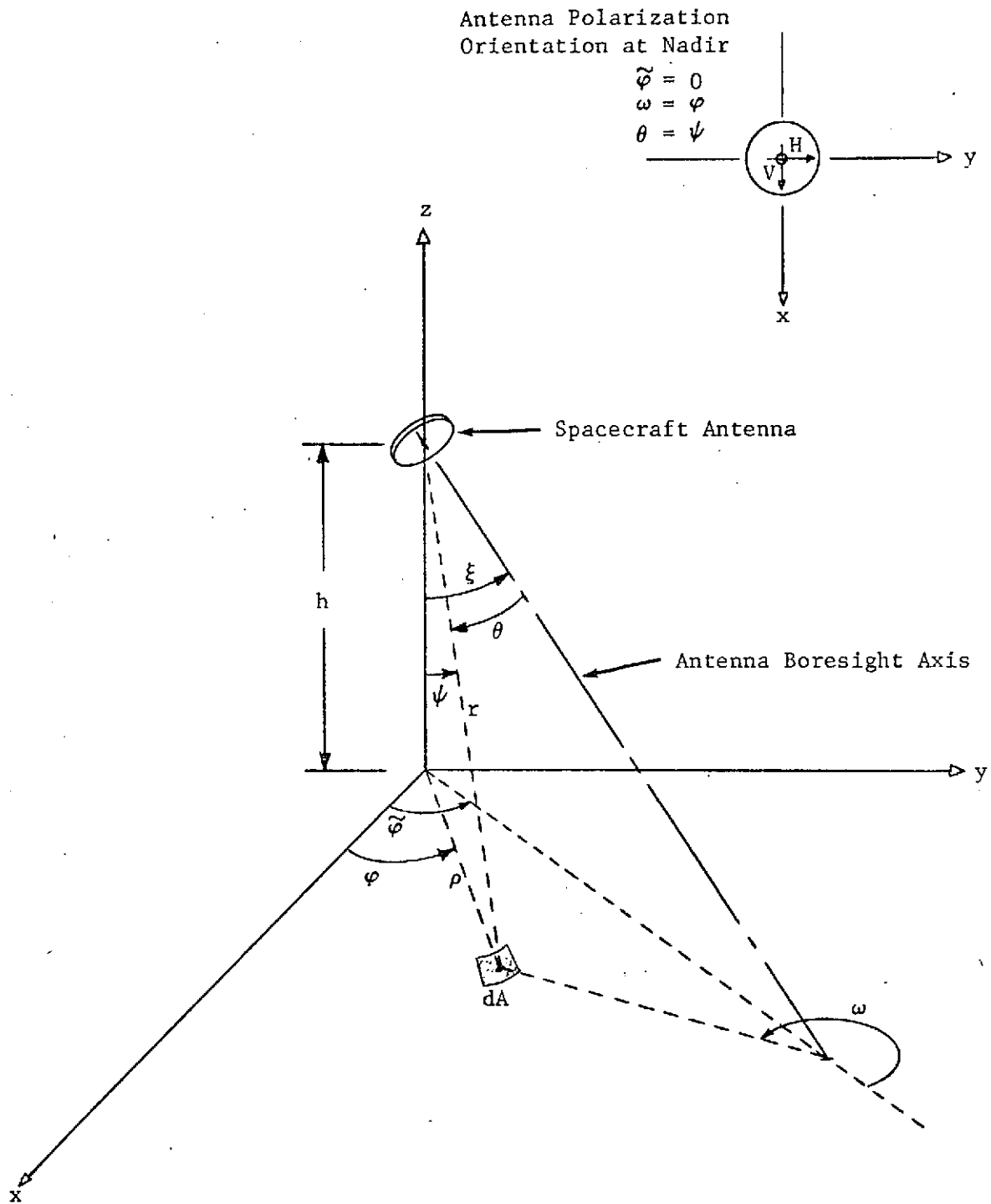


Figure 2A1. Geometry for the flat-sea impulse response computation.

and

$$\cos \omega = \frac{-\tan \xi + \left(\frac{\rho}{h}\right) \cos(\phi - \tilde{\phi})}{\sqrt{(\rho/h)^2 + \tan^2 \xi - 2(\rho/h) \tan \xi \cos(\phi - \phi)}} \quad (2A8)$$

It should be noted that the ϕ -dependence always appears as the difference $\phi - \tilde{\phi}$, thus we can ignore $\tilde{\phi}$ since the integration on ϕ is over a complete 2π radians. The first set of antenna patterns recorded by GE (ref. 2A4) indicated that the vertical port antenna pattern was nearly independent of ω (circularly symmetric) out to about -20 dB. Revised antenna patterns (ref. 2A5), however, show that both the horizontal and vertical ports exhibit asymmetric pattern shapes. When the antenna pattern is asymmetric, the ω -integration in (2A6) is very difficult to perform and must be done numerically. As a result, one tends to lose the physics of the problem in mathematical detail. In order to simplify the problem, it was assumed that the antenna pattern was independent of the azimuth angle coordinate ω and of the form*

$$f(\theta, \omega) \approx e^{-\frac{\sin^2 \theta}{\gamma}} \quad (2A9)$$

The constant γ determines the beamwidth of the pattern and should be chosen to yield an average of the two principal plane beamwidths when dealing with asymmetric patterns. Substituting (2A9) in (2A6) and using (2A7) yields

$$P_r(t, \xi) = \frac{G_o^2 \lambda^2}{L_p h^4 (4\pi)^3} \int_0^\infty \frac{\delta\left(t - \frac{2h}{c} \sqrt{1 + \epsilon^2}\right) \sigma^o(\psi)}{[1 + \epsilon^2]^2} \rho d\rho \int_0^{2\pi} \exp\left\{\frac{-4}{\gamma} \left[1 - \frac{1}{(1 + \epsilon^2)} (\cos^2 \xi + \epsilon \sin 2\xi \cos \phi + \epsilon^2 \sin^2 \xi \cos^2 \phi)\right]\right\} d\phi \quad (2A10)$$

*This approximation is assumed valid out to the -10 dB points in the pattern.

where $\epsilon = \rho/h$ and $\phi - \tilde{\phi}$ has been replaced by ϕ since the integration is over 2π radians. Denoting the ϕ -integral as Q and rearranging terms yield

$$Q = e^{-\frac{4}{\gamma} \left[1 - \frac{\cos^2 \xi}{1 + \epsilon^2} \right] + b} \int_0^{2\pi} e^{a \cos \phi + b \sin^2 \phi} d\phi \quad (2A11)$$

where

$$a = \frac{4\epsilon}{\gamma} \frac{\sin 2\xi}{(1 + \epsilon^2)}$$

$$b = \frac{4\epsilon^2}{\gamma} \frac{\sin^2 \xi}{(1 + \epsilon^2)}$$

Since

$$e^{-b \sin^2 \phi} = \sum_{n=0}^{\infty} \frac{(-1)^n b^n \sin^{2n} \phi}{n!},$$

equation (2A11) can be integrated exactly and

$$Q = 2\sqrt{\pi} e^{-\frac{4}{\gamma} \left[1 - \frac{\cos^2 \xi}{(1 + \epsilon^2)} \right] + b} \sum_{n=0}^{\infty} \frac{(-1)^n \Gamma(n + \frac{1}{2})}{\Gamma(n + 1)} \left(\frac{2b}{a}\right)^n I_n(a)$$

where the $I_n(\cdot)$ are Bessel functions of the second kind and order n . Since $2b/a = \epsilon \tan \xi$, Q becomes

$$Q = 2\sqrt{\pi} \exp \left\{ -\frac{4}{\gamma} \left[1 - \frac{\cos^2 \xi}{(1 + \epsilon^2)} - \epsilon^2 \sin^2 \xi \right] \right\} \sum_{n=0}^{\infty} \frac{(-1)^n \Gamma(n + \frac{1}{2})}{\Gamma(n + 1)} (\epsilon \tan \xi)^n I_n \left(\frac{4\epsilon}{\gamma} \frac{\sin 2\xi}{(1 + \epsilon^2)} \right) \quad (2A12)$$

It should be noted that since both ξ and ρ/h are very small, the series in (2A12) will numerically converge very rapidly. Substituting (2A12) and $\beta = \rho^2/h^2$ in (2A10) yields the following expression for the flat sea impulse response,

$$P_r(t, \xi) = \frac{\sqrt{\pi} G_o^2 \lambda^2}{L_p (4\pi)^3 h^2} \int_0^\infty \frac{\delta\left(t - \frac{2h}{c} \sqrt{1+\beta}\right) \sigma^0(\psi)}{\left[1+\beta\right]^2} \exp\left\{-\frac{4}{\gamma} \left[1 - \frac{\cos^2 \xi}{(1+\beta)} - \beta \sin^2 \xi\right]\right\} \\ \cdot \sum_{n=0}^{\infty} \frac{(-1)^n \Gamma(n + \frac{1}{2})}{\Gamma(n+1)} \left[\sqrt{\beta} \tan \xi\right]^n I_n\left(\frac{4}{\gamma} \sqrt{\beta} \frac{\sin 2\xi}{(1+\beta)}\right) d\beta \quad (2A13)$$

Using the property of the δ -function, the integral in (13A) is equal to the integrand evaluated at

$$t - \frac{2h}{c} \sqrt{1+\beta} = 0 \text{ or } \beta = c^2 t^2 / 4h^2 - 1$$

and

$$P_r(t, \xi) = \frac{\sqrt{\pi} G_o^2 \lambda^2}{(4\pi)^3 h^2 L_p} \frac{\sigma^0(\psi_o)}{\left[\frac{ct}{2h}\right]^4} \exp\left\{-\frac{4}{\gamma} \left[1 - \frac{\cos^2 \xi}{c^2 t^2 / 4h^2} - \left(\left(\frac{ct}{2h}\right)^2 - 1\right) \sin^2 \xi\right]\right\} \\ \cdot \sum_{n=0}^{\infty} \frac{(-1)^n \Gamma(n + \frac{1}{2})}{\Gamma(n+1)} I_n\left(\sqrt{\left(\frac{ct}{2h}\right)^2 - 1} \frac{\sin 2\xi}{\left(\frac{ct}{2h}\right)^2} \frac{4}{\gamma} \left[\sqrt{\left(\frac{ct}{2h}\right)^2 - 1} \tan \xi\right]^n\right)$$

Converting to the two-way incremental ranging time, i.e., $\tau = t - 2h/c$, the flat-sea impulse response becomes

$$P_r(\tau, \xi) = \frac{\sqrt{\pi} G_o^2 \lambda^2}{(4\pi)^3 h^2 L_p} \frac{\sigma^o(\psi_o)}{\left[\frac{c\tau}{2h} + 1\right]^4} \exp \left\{ -\frac{4}{\gamma} \left[1 - \frac{\cos^2 \xi}{\left(\frac{c\tau}{2h} + 1\right)^2} - \left\{ \left(\frac{c\tau}{2h} + 1\right)^2 - 1 \right\} \sin^2 \xi \right] \right\} \\ \cdot \sum_{n=0}^{\infty} \frac{(-1)^n \Gamma(n + \frac{1}{2})}{\Gamma(n + 1)} I_n \left(\sqrt{\left(\frac{c\tau}{2h} + 1\right)^2 - 1} \frac{4 \sin 2\xi}{\gamma \left(\frac{c\tau}{2h} + 1\right)^2} \right) \left[\tan \xi \sqrt{\left(\frac{c\tau}{2h} + 1\right)^2 - 1} \right]^n \quad (2A14)$$

The total mean return is a convolution of (2A5) with (2A14), i. e.

$$\langle P_{rss}(\tau, \xi) \rangle = \int_0^{\infty} P_r(\hat{\tau}, \xi) P_{ss}(\tau - \hat{\tau}) d\hat{\tau} \quad , \quad (2A15)$$

where the lower limit in (2A15) is taken to be 0 since $P_r(\tau, \xi)$ is identically zero for $\tau < 0$. In general, (2A15) must be integrated numerically; however, for $\xi = 0^\circ$ (nadir) some simplification is possible. In particular, the flat-sea impulse response is, for $\xi = 0^\circ$,

$$P_r(\tau, 0) = \frac{\pi G_o^2 \lambda^2}{(4\pi)^3 h^2 L_p} \frac{\sigma^o(\psi_o)}{\left[\frac{c\tau}{2h} + 1\right]^4} e^{-\frac{4}{\gamma} \left[1 - \frac{1}{\left(\frac{c\tau}{2h} + 1\right)^2} \right]} \quad .$$

Since $\frac{c\tau}{2h} \approx \ll 1$ for nadir operation,

$$P_r(\tau, 0) \approx \frac{\pi G_o^2 \lambda^2}{(4\pi)^3 h^2 L_p} \sigma^o(\psi_o) e^{-\frac{4c}{\gamma h} \tau} \quad , \quad (2A16)$$

and since the antenna beamwidth is so narrow we may take $\psi_o \approx 0^\circ$. Substituting (2A16) and (2A5) in (2A15) yields the following expression for the mean return waveform on nadir,

$$\langle P_{\text{RSS}}(\tau, 0) \rangle = \frac{\pi G_o^2 \lambda^2}{2(4\pi)^3 h^2 L_p} \left(\frac{\hat{P}_t}{L_p} \right) \sigma^o(0) \exp \left\{ -\Delta(\tau-100)^2 + \frac{1}{\Delta} \left[\frac{2c}{\gamma h} - \Delta(\tau-100) \right]^2 \right\} \cdot \left\{ 1 - \operatorname{erf} \left[\frac{\left\{ \frac{2c}{\gamma h} - \Delta(\tau-100) \right\}}{\sqrt{\Delta}} \right] \right\}, \quad (2A17)$$

where

$$\Delta = \frac{1}{\alpha} \left[1 - \frac{1}{\left(1 + \alpha c^2 / 8 \zeta_m^2 \right)} \right].$$

It should be noted that $\sqrt{\alpha}$ is proportional to the pulse length and not to the square root of the pulse length; this arises because of the way in which the pulse shape was defined (see equation 2A1).

The two principal-plane antenna patterns are shown in Figure 2A2 for vertical port excitation. As can be seen, the Gaussian pattern approximation provides a reasonable fit; however, the parameter γ must be changed by about a factor of two between the $\omega = 0^\circ$ and 90° pattern cuts in order to maintain the fit. Figure 2A3 is a plot of the mean return waveform as computed from (2A17) with

$$K = \left(\frac{\hat{P}_t}{L} \right) \frac{\pi G_o^2 \lambda^2}{2(4\pi)^3 h^2 L_p}.$$

The difference between the two curves for $\gamma = 7.88 \times 10^{-4}$ and 3.66×10^{-4} is 0.88 dB at the peaks of the two mean returns. These two curves provide bounds on the true mean return which will lie somewhere between the $\gamma = 7.88 \times 10^{-4}$ and 3.66×10^{-4} curves. Also shown in Figure 2A3 is a mean return with $\gamma = 5 \times 10^{-3}$ which is just about midway between the other two curves. Hence, it was assumed that the true vertical port antenna pattern could be represented by the Gaussian function given in (2A9) and with $\gamma = 5 \times 10^{-3}$. Unfortunately, time was not available to reduce GE's antenna

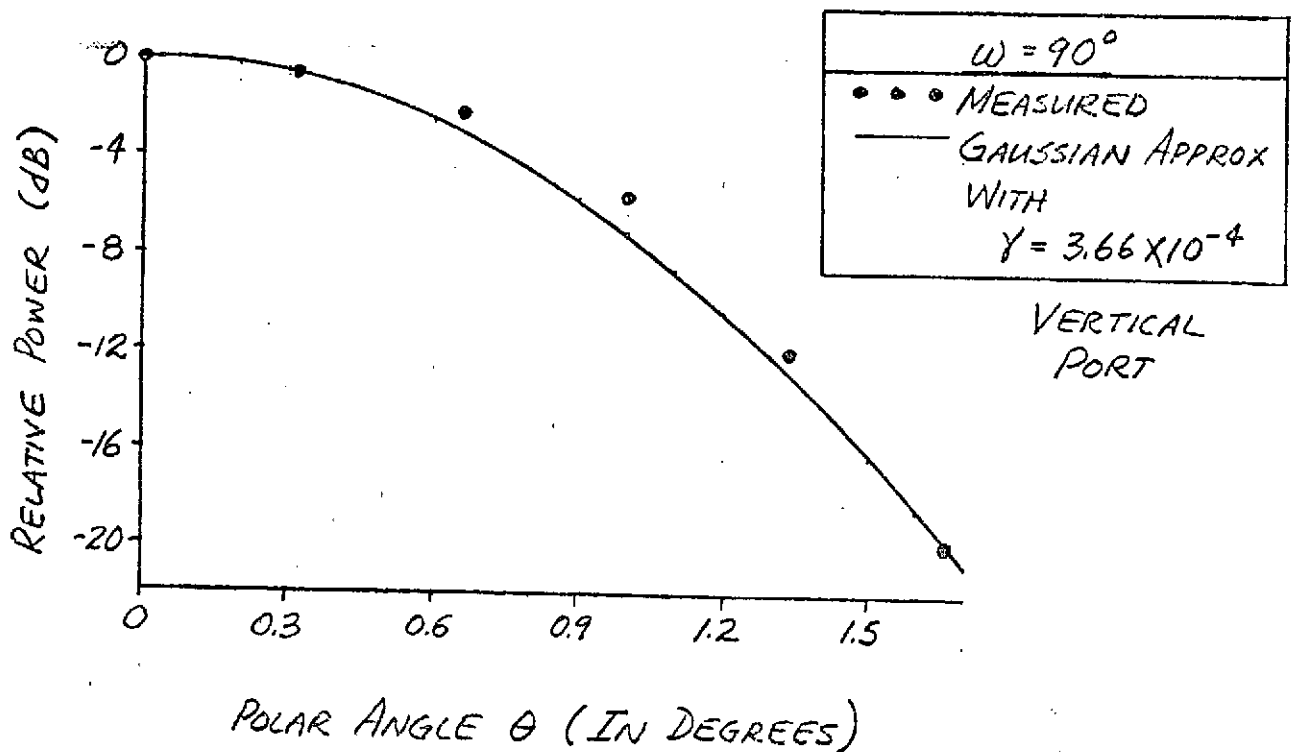
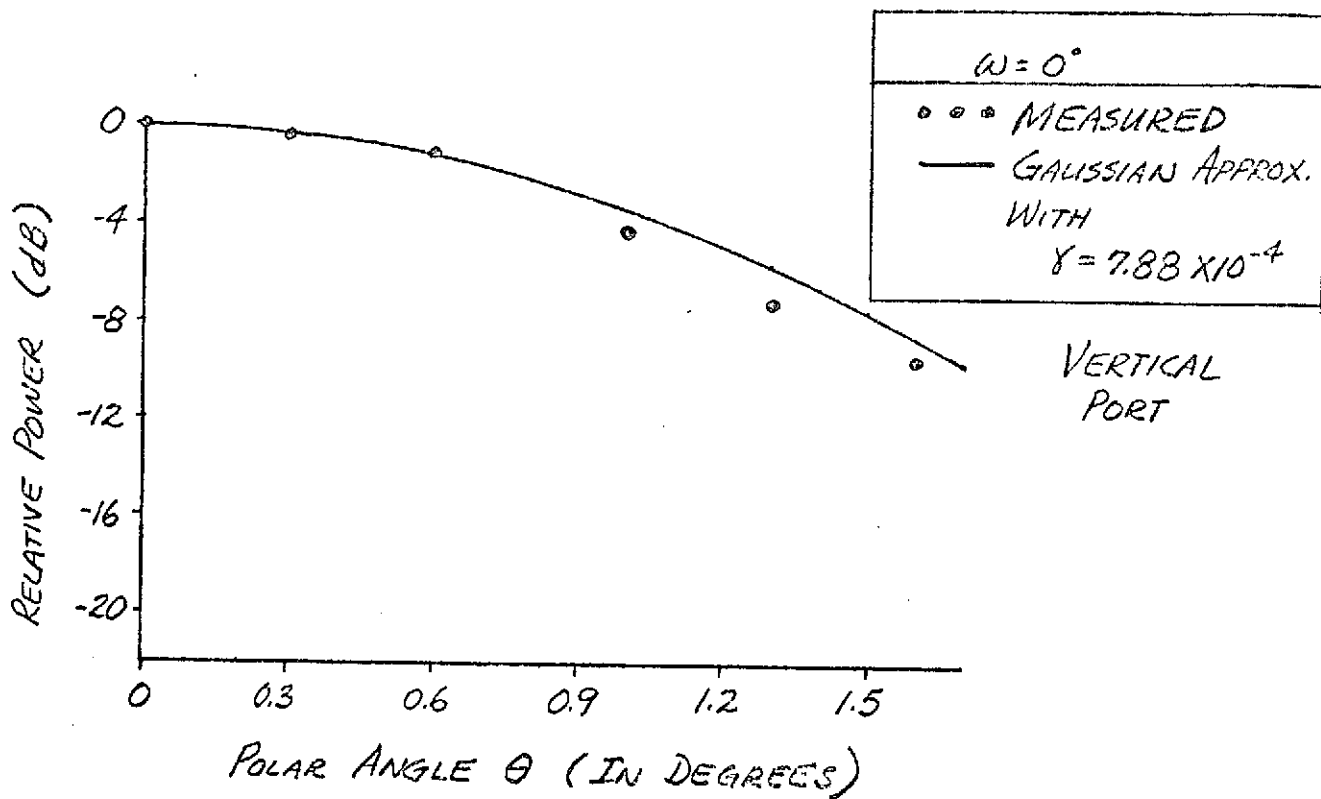


Figure 2A2. Vertical port principal plane antenna patterns (in Figure 2A1, $\omega = 0$ corresponds to the $y = 0$ plane and $\omega = 90^\circ$ corresponds to the $x = 0$ plane).

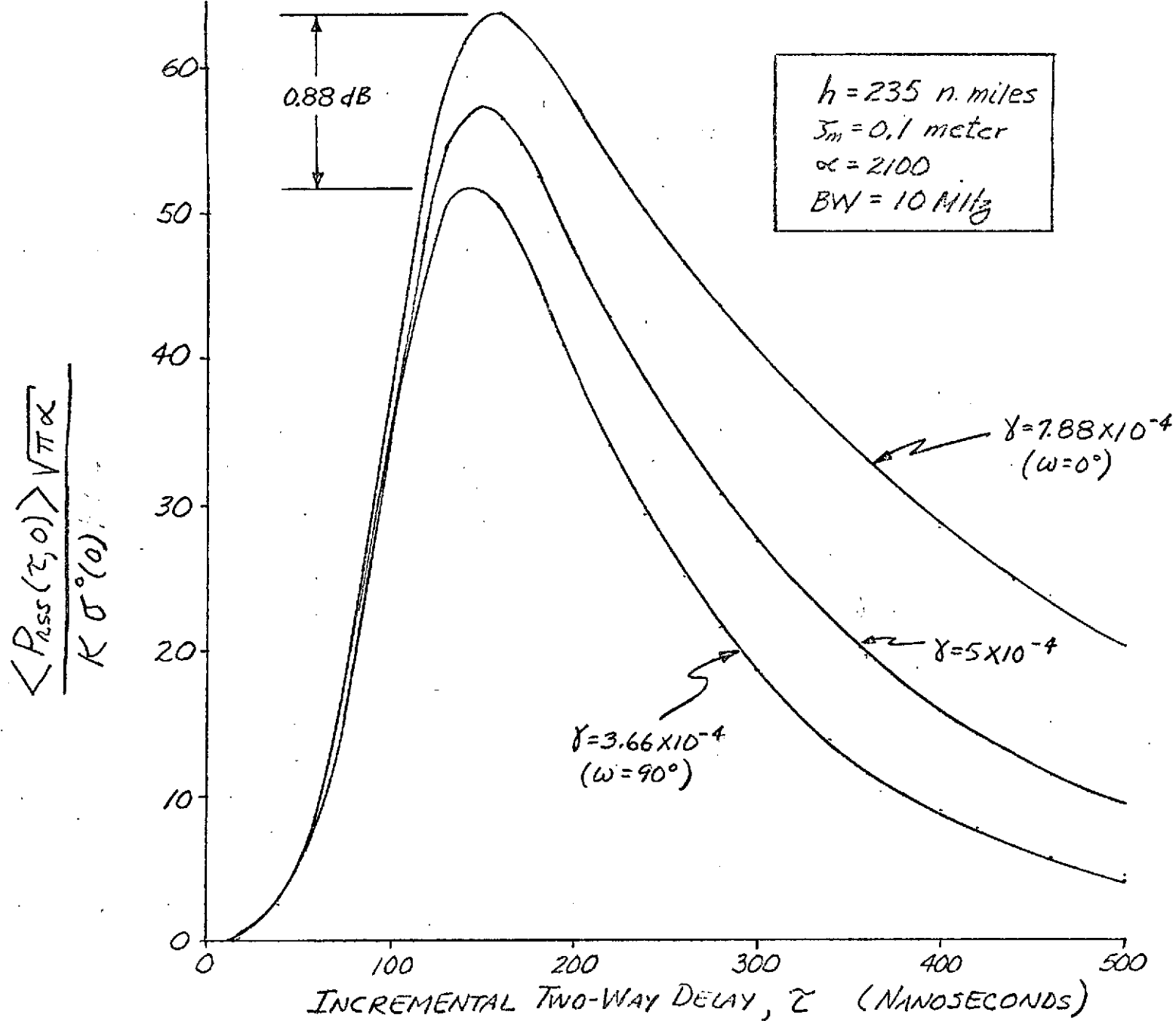


Figure 2A3. Normalized nadir mean return for various antenna pattern tapers.

pattern data and compute $\langle P_{\text{rss}}(\tau, 0) \rangle$ using these data; however, the circularly symmetric Gaussian pattern with $\gamma = 5 \times 10^{-4}$ should be a good computational approximation.

Figure 2A4 is a plot of the normalized mean return waveform at nadir for various values of rms waveheight ζ_m . These curves clearly show that both the shape and amplitude of the mean return waveform are dependent on ζ_m only through variations in σ^0 for reasonable values of ζ_m , i. e. $\zeta_m \lesssim 2$ meters.* In deriving equation (2A17), we assumed that σ^0 could be taken from inside the integral since the angle $\psi = \tan^{-1}(\rho/h)$ would not differ appreciably from the pointing angle of the antenna. Using the dependency of σ^0 on ψ as determined in ref. A1, equation (2A15) was numerically integrated for various pointing angles of the antenna out to 15.6° . There was no appreciable difference between $\langle P_{\text{rss}}(\tau, \xi) \rangle$ computed with $\sigma^0(\psi)$ inside the integral and $\langle P_{\text{rss}}(\tau, \xi) \rangle$ computed with $\sigma^0(\psi=\xi)$ taken outside of the integral. Figures 2A5 through 2A9 are plots of the mean return for antenna pointing angles of 0° and 0.5° , 3° , 8° , and 15.6° , respectively. These results were computed by numerically integrating (2A15) using (2A14) and (2A5).

Figure 2A10 shows how the peak-of-the-mean return decreases as the antenna is scanned off nadir, excluding σ^0 effects. This curve shows the decrease in the peak-of-the-mean return as a function of pulse shape, scan angle and antenna pattern. The total decrease in the peak-of-the-mean return as a function of scan angle is obtained by adding the variation of σ^0 (in dB) to this curve. For a wind speed of 5 knots, σ^0 changes by about 17 dB as the pointing angle varies from 0° to 15.6° . Thus, the total change in the peak-of-the-mean return from 0° to 15.6° is about 36 dB. This is the dynamic range which would be required of the receiver if it detected the peak-of-the-mean return.

*When $\zeta_m = 2$ meters, the significant waveheight, $H_{1/3}$, is 8 meters.

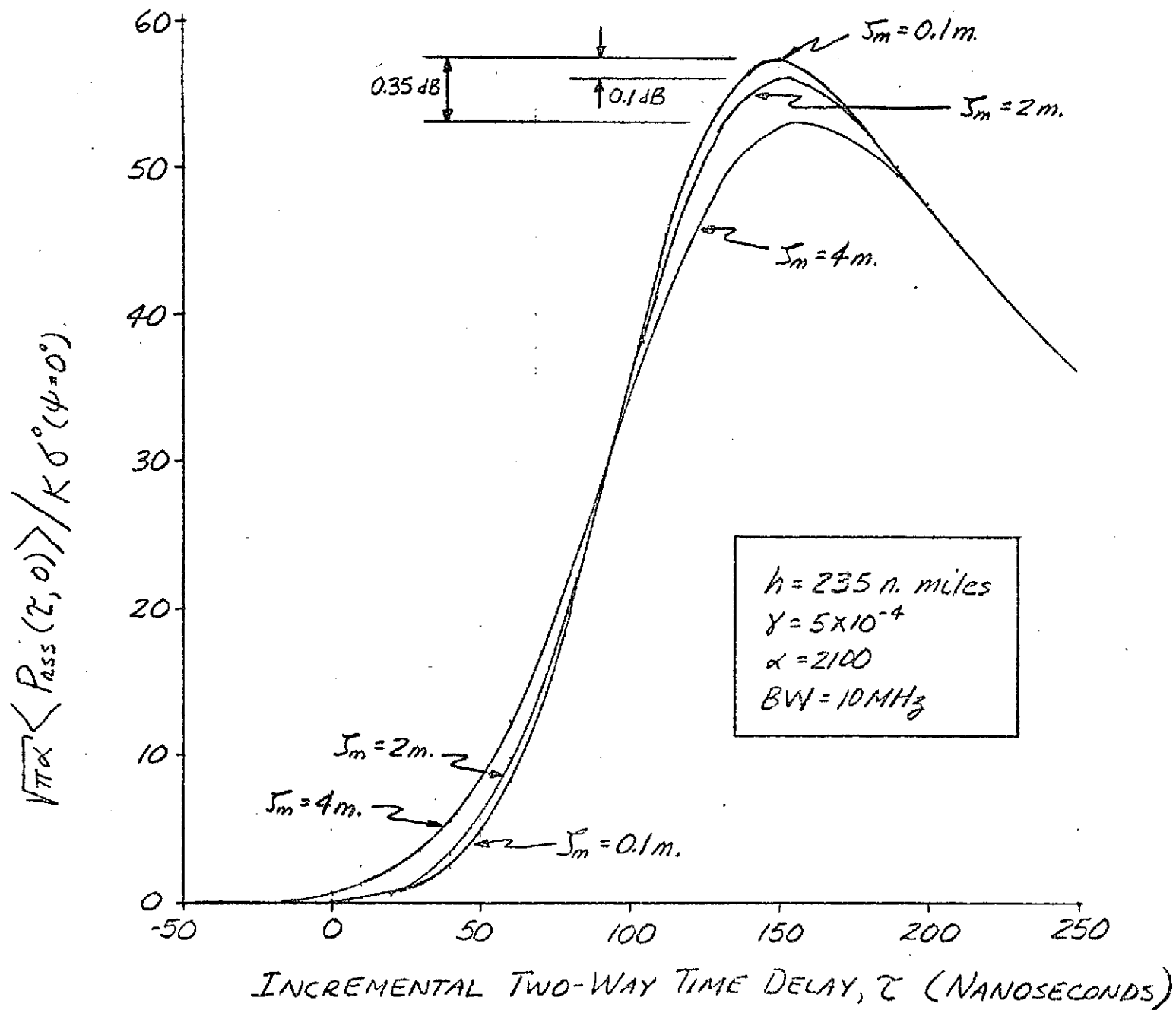


Figure 2A4. Normalized nadir mean return as a function of the rms waveheight ζ_m .

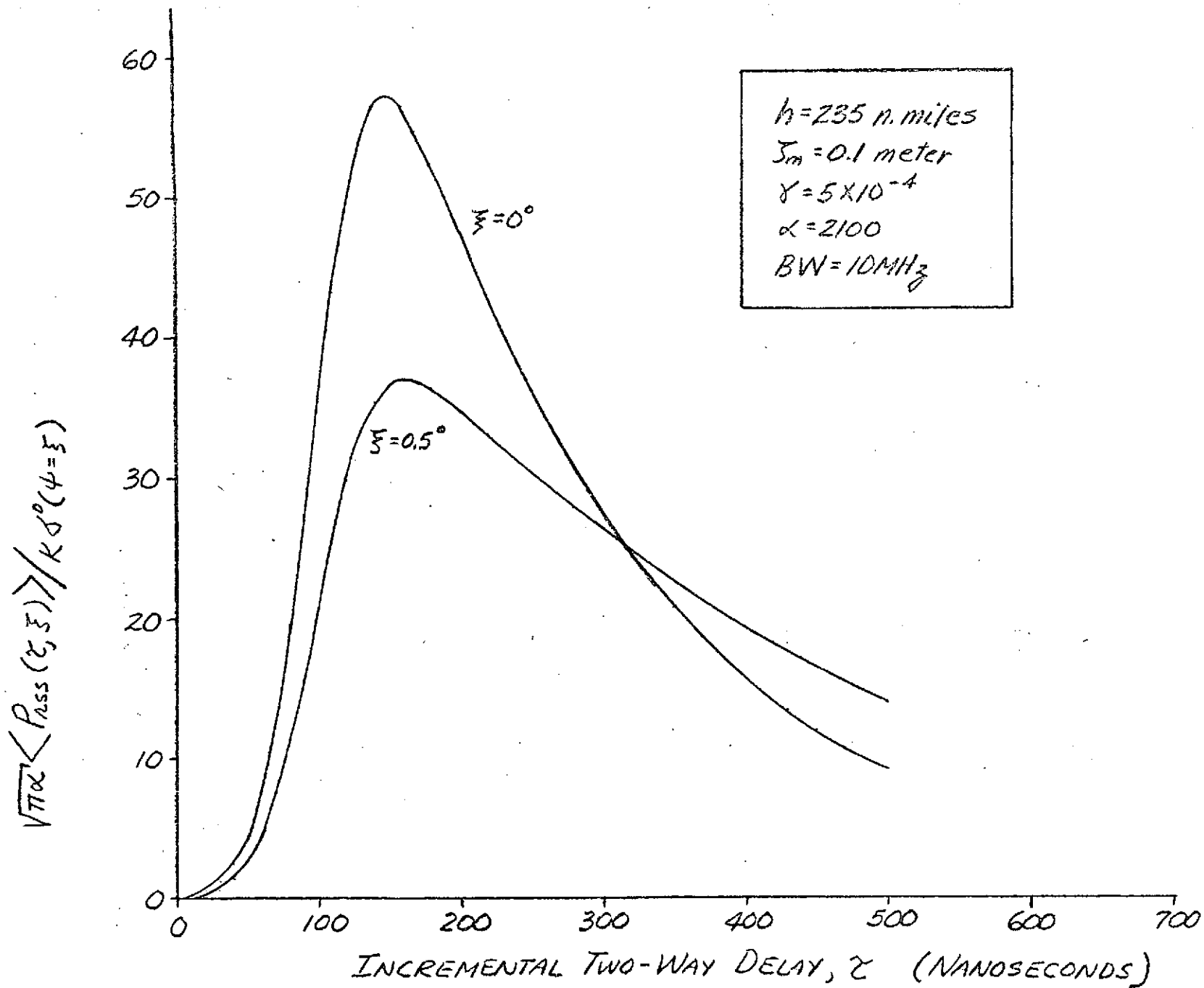


Figure 2A5. Normalized mean return for antenna pointing angles of 0° and 0.5° off nadir.

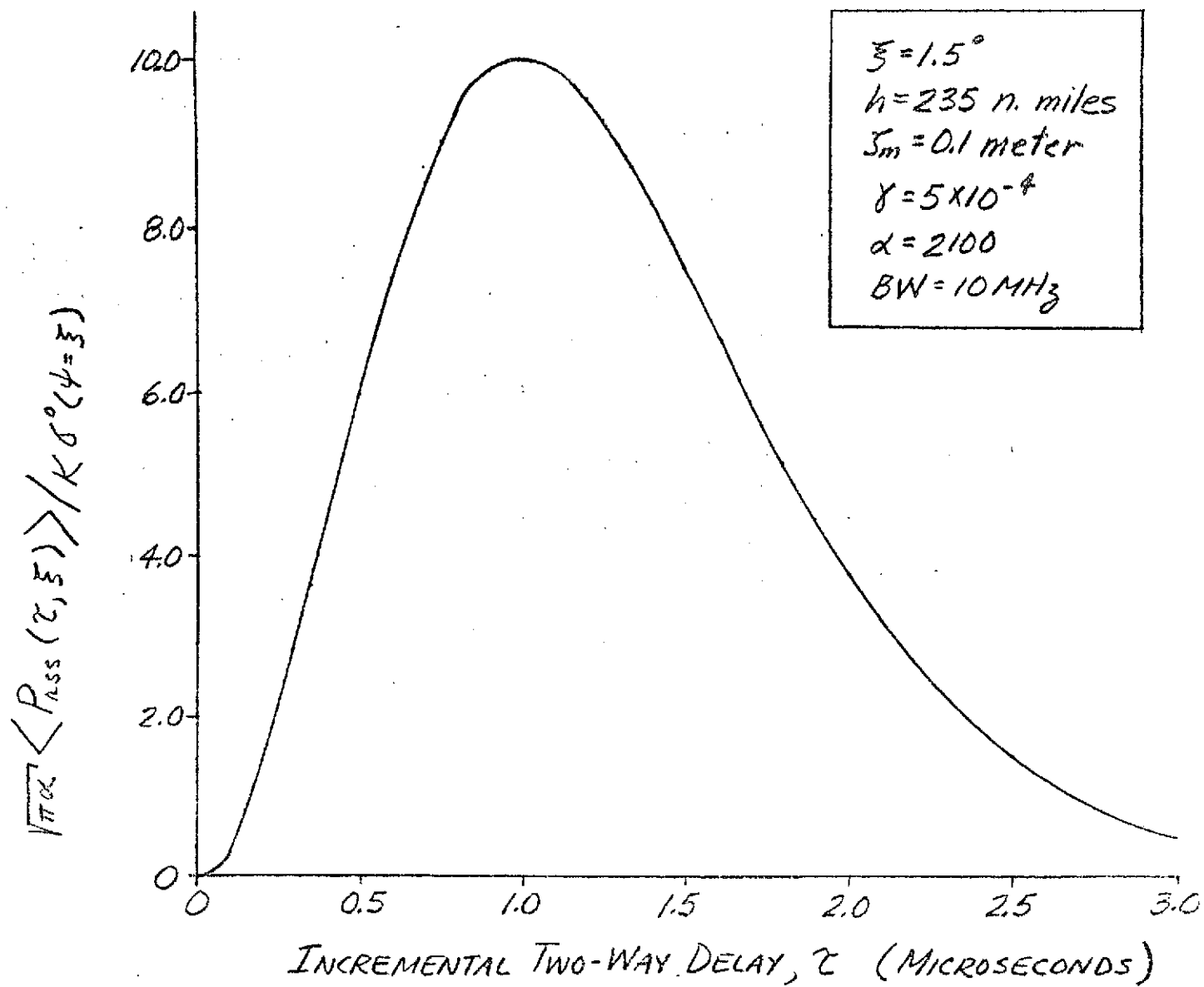


Figure 2A6. Normalized mean return for an antenna pointing angle of 1.5° off nadir.

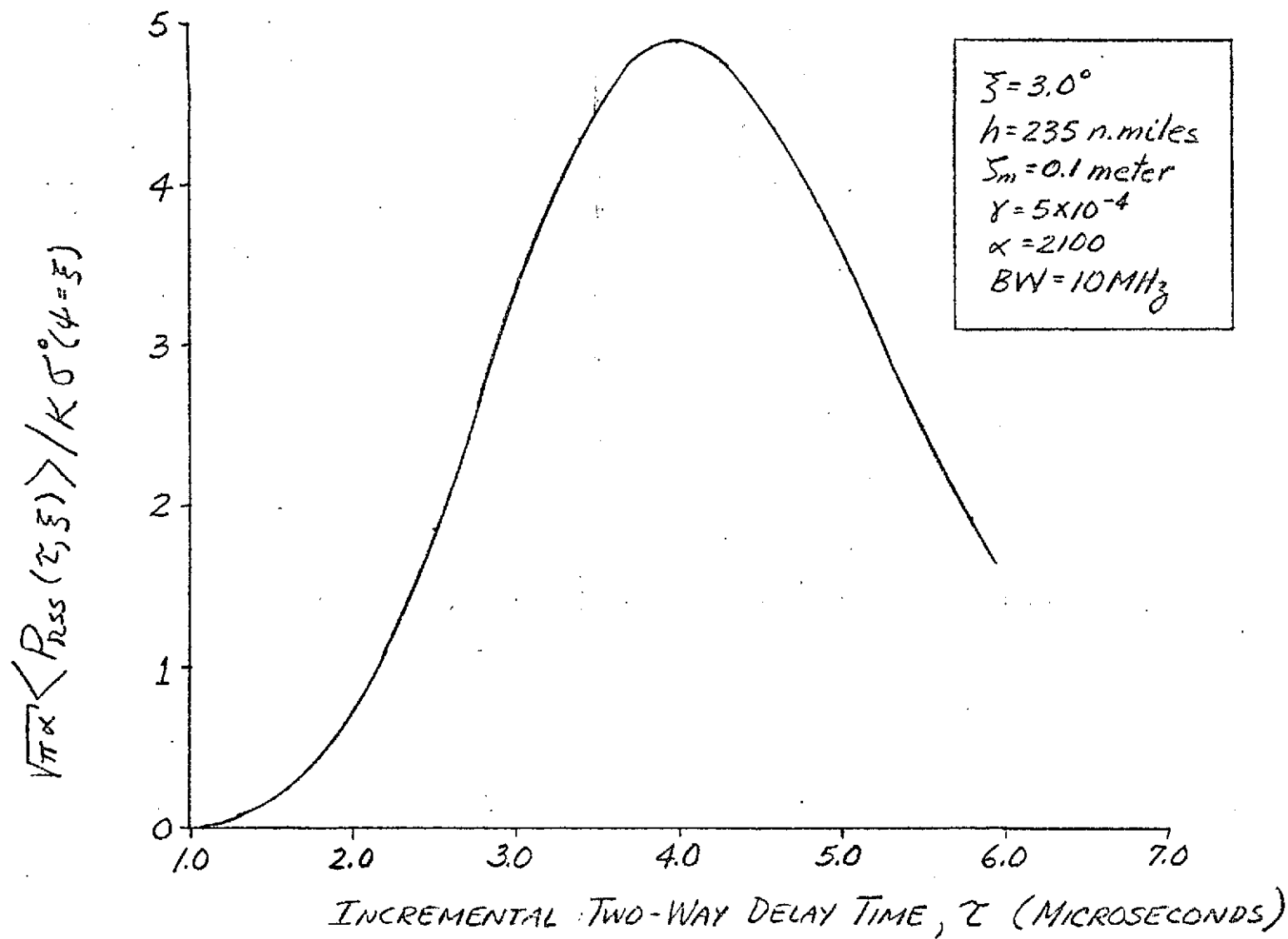


Figure 2A7. Normalized mean return for an antenna pointing angle of 3° off nadir.

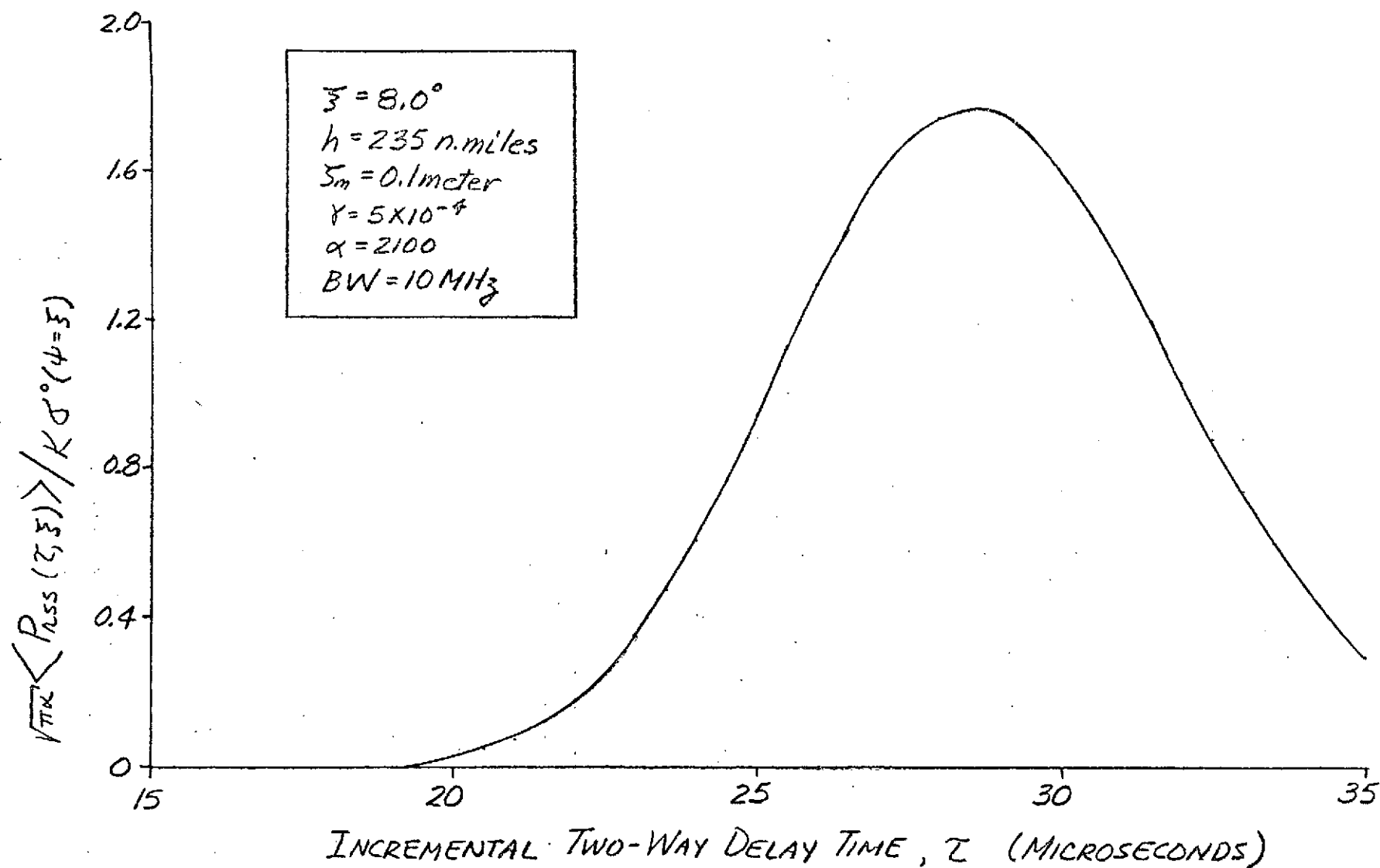


Figure 2A8. Normalized mean return for an antenna pointing angle of 8° off nadir.

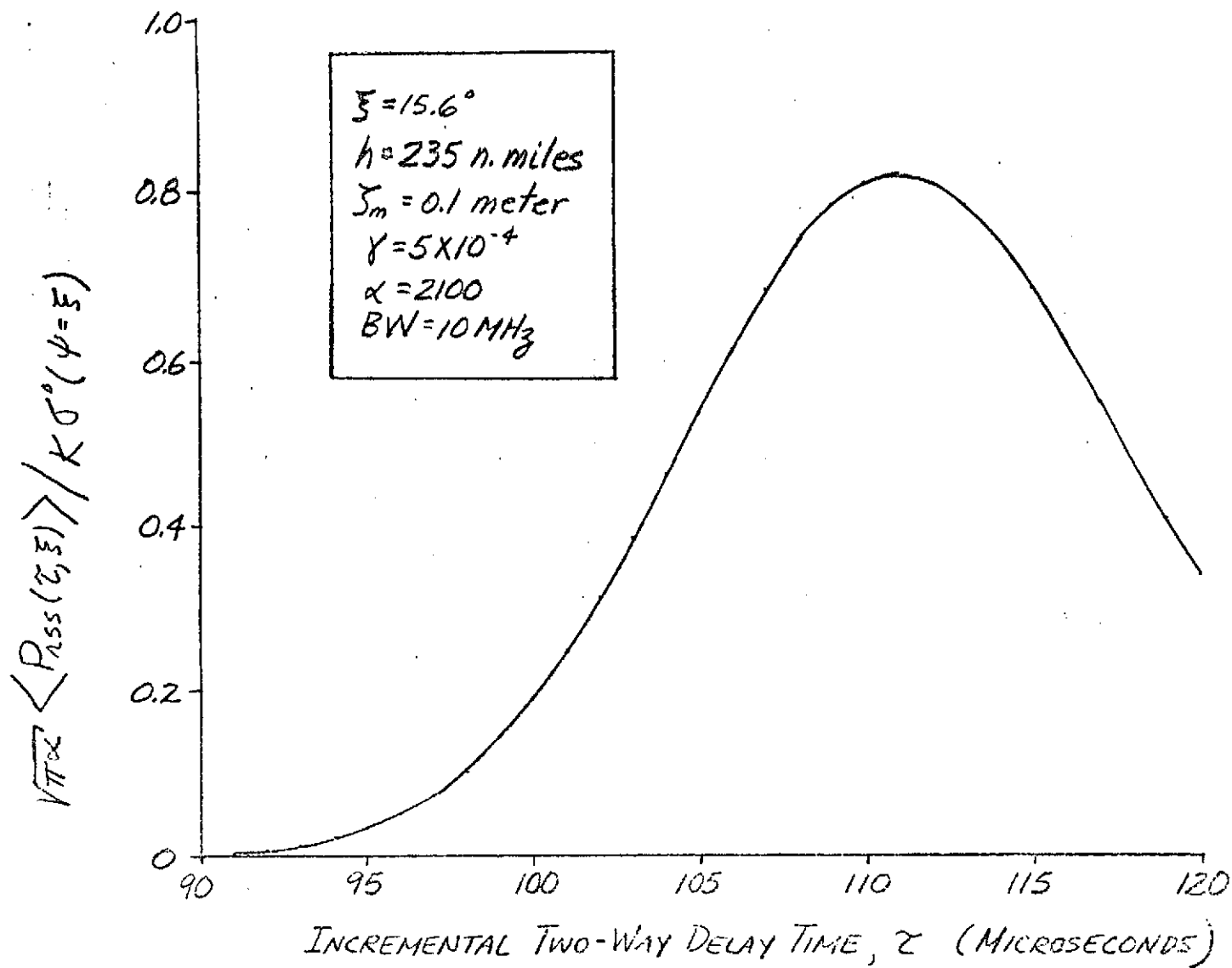


Figure 2A9. Normalized mean return for an antenna pointing angle of 15.6° off nadir.

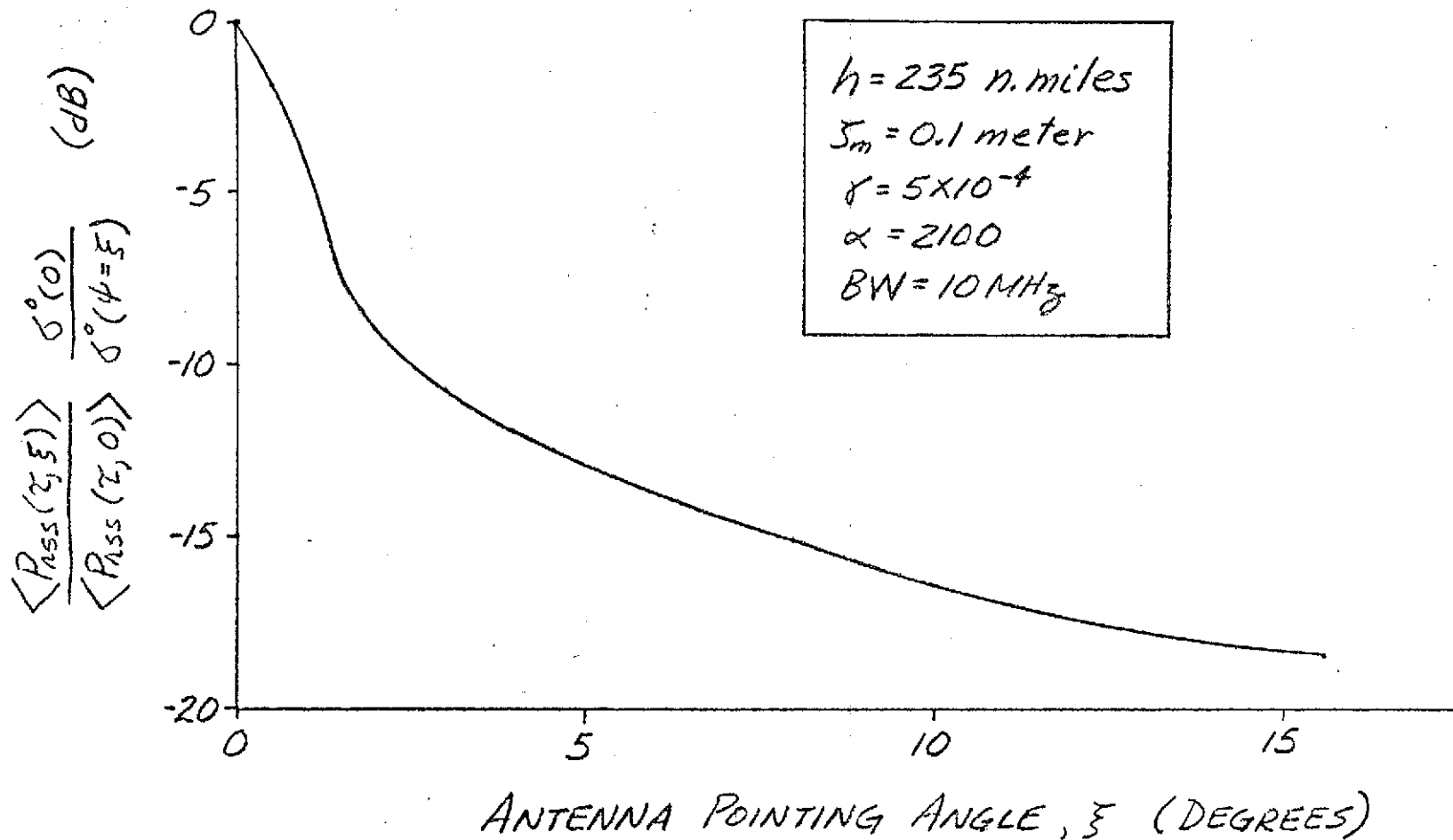


Figure 2A10. Decrease in peak-of-mean return as a function of antenna pointing angle and not including σ^0 effects.

REFERENCES

- 2A1. "A Study of the Capabilities of the Geodetic Satellite Altimeter to Measure Ocean Surface Characteristics," Final Report, Contract No. NASW-1909, Research Triangle Institute, April, 1970.
- 2A2. "S-193 Microwave Radiometer/Scatterometer Altimeter," Calibration Data Report, Vol. 1B, Contract No. NAS9-11195, General Electric Company, October, 1972.
- 2A3. Moore, R. K. and C. S. Williams, Jr., "Radar Terrain Return at Near-Vertical Incidence," Proc. of IRE, Vol. 45, pp. 228-238, February, 1957.
- 2A4. "S-193 Microwave Radiometer/Scatterometer Altimeter," Calibration Data Report, Vol. II, Contract No. NAS9-11195, General Electric Company, May, 1972.
- 2A5. "S-193 Microwave Radiometer/Scatterometer Altimeter," Calibration Data Report, Vol. II, Contract No. NAS9-11195, General Electric Company, July, 1972.

APPENDIX 2B

SIMULATION OF THE AGC r-FACTOR

This section presents the results of our investigation of the relationship between the "mean of the peaks" and the "peak-of-the-mean" or the r-factor. The need for this relationship comes about because of the manner in which the Skylab S-193 altimeter operates. (The GEOS-C AGC system operates similarly in the acquisition mode.) This AGC scheme basically involves development of a control voltage which is a function of the peak signal voltage encountered during an AGC gate interval. Since data processing procedures depend on the peak of the average waveform instead, there is an obvious need for a connecting relationship.

The first work relating to r-factor, by Lambert (ref. 2B1), comprised a state variable simulation of the r-factor values and use of closed-form detection statistics from Rice (ref. 2B2). The present effort was undertaken expecting to corroborate Lambert's findings; the results, however, were found to be in substantial disagreement with his results. We argue the validity of our data based on the added degree to which the S-193 receiver is modeled. For example, rather than assuming Rayleigh or Chi-Squared detector statistics, the detector/video amplifier statistics are actually generated to the extent to which a valid system model exists for the S-193 hardware.

A block diagram of our hybrid computer simulation is shown in Figure 2B1. All computations prior to and including the video amplifier were performed using an EAI 380 analog/hybrid computer and the remaining operations utilized a PDP8/e minicomputer. Receiver thermal noise was not included in this simulation and the results are felt to correspond to SNR values greater than 10 dB. Other simulation details are identical to those given in our 1972 report (ref. 2B3). Three 100 ns waveform cases were computed corresponding to 0, 1, and 1.5 degrees off-nadir; a few sample values of the mean waveforms are plotted on the theoretical waveforms* in Figures 2B2 and 2B3 and the correspondence is seen to be quite good. Time did not permit computation

*These waveforms are slightly different from those computed in Appendix 2A. They do, however, correspond to the waveforms employed in Lambert's computations. This was done in order to study the exact same situation which Lambert studied.

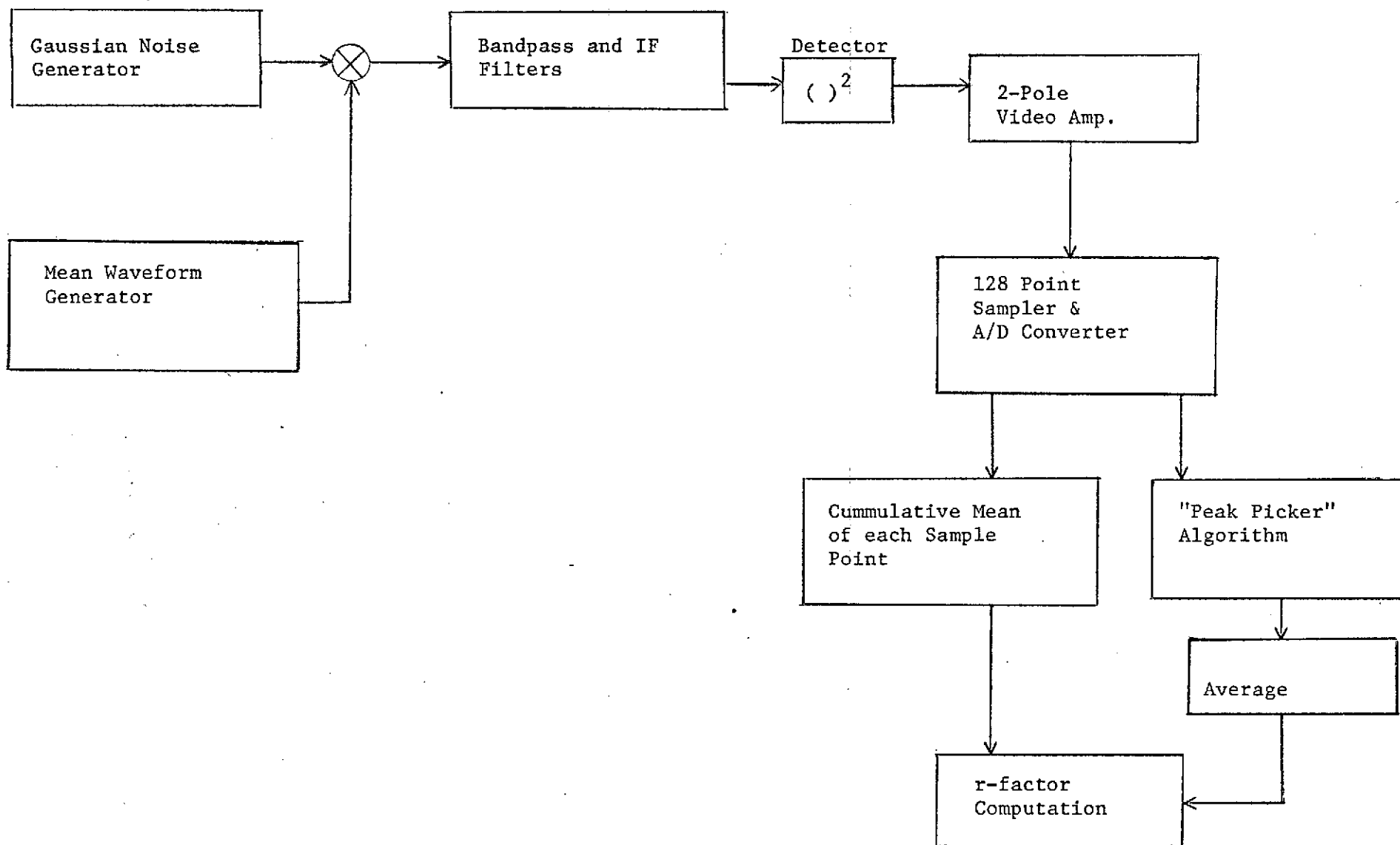


Figure 2B1. Block Diagram of r-factor Simulation.

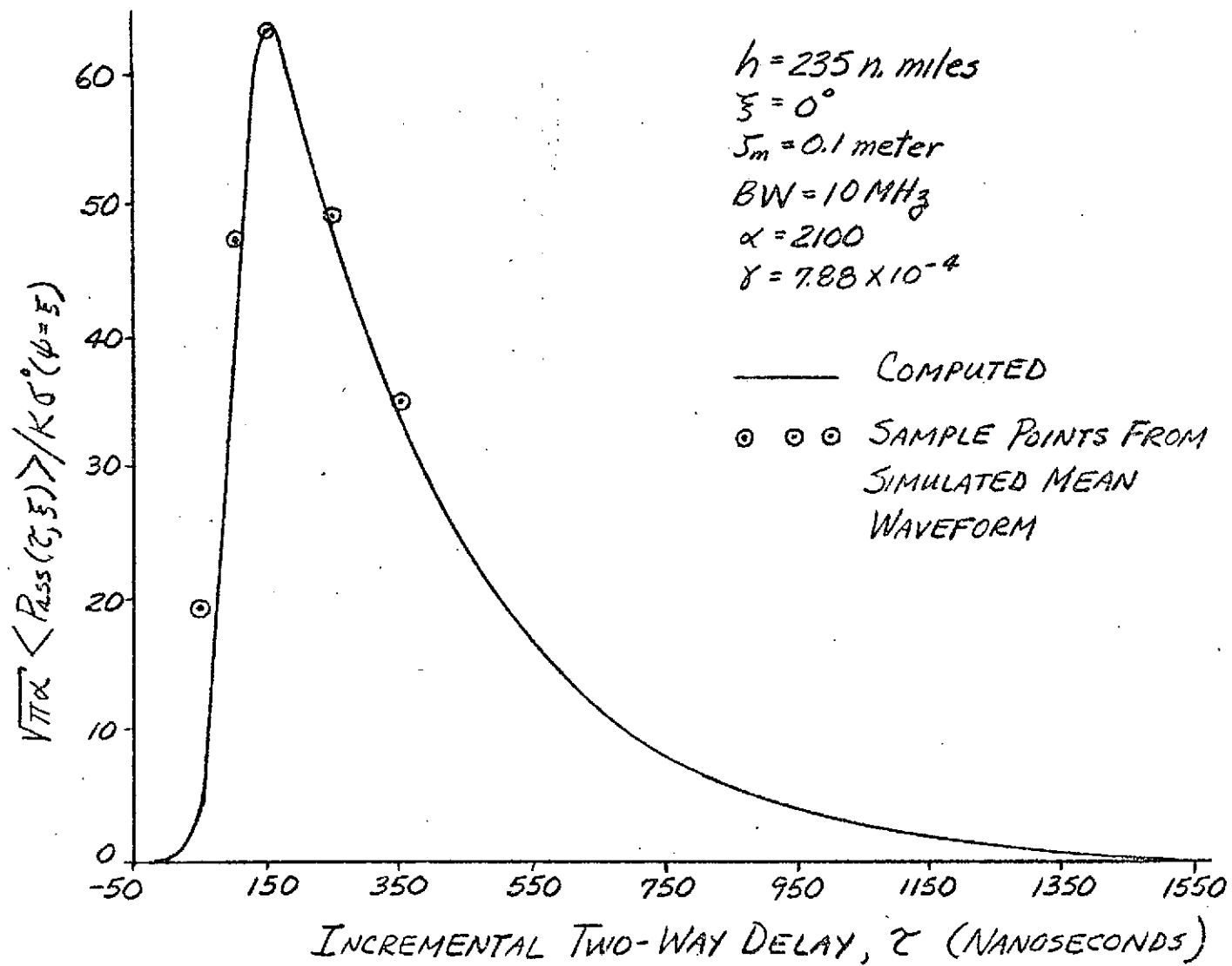


Figure 2B2. Comparison of theoretical and simulated mean return waveform at nadir.

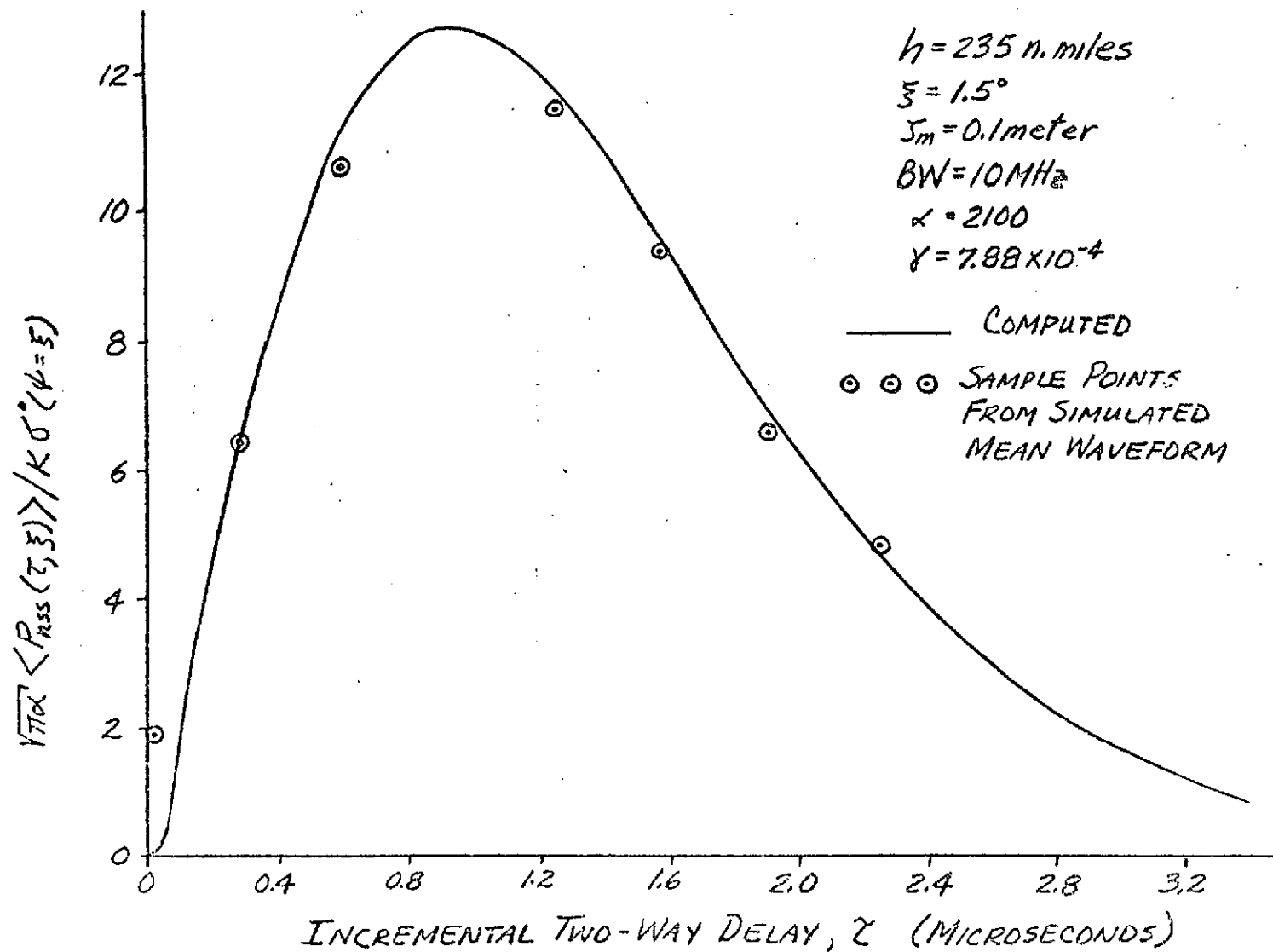


Figure 2B3. Comparison of theoretical and simulated mean return waveform at 1.5° off nadir.

of other, large off-nadir angles.

Figure 2B4 shows a comparison of the two r-factor results. Whereas Lambert's result decreases rapidly over the angle range of 0-1.5 degrees, our result displays an r-factor of 0.69, 0.58, and 0.53 at angles of 0, 1.0, and 1.5 degrees. Note that the discrepancy between the two curves is considerably larger than the expected angular dependence of σ^0 .

In order to verify our simulation results on the r-factor problem, we have investigated the AGC calibration data presented in ref. 2B4. Figure 2B5 is a plot of the AGC (voltage) analog-to-digital converter output versus altimeter receiver input power as measured at the output of the antenna. These data were obtained from the flight model of the altimeter and were selected because they represent normal operating conditions, i.e. 25°C, 10 MHz bandwidth and a 600 ns AGC gate window. Unfortunately, ref. 2B4 did not state what the input power was; however, it must be the mean-of-the-peaks of the input power waveform because of the manner in which the AGC voltage is measured.

The input pulse shape was triangular with a 100 ns rise time and a 500 ns decay time. This shape is a very good approximation to the mean return pulse shape at nadir (see Figure 2B2). The "clean pulse" curve was obtained with just the pulse input, and the input power in this case is equivalent to the peak-of-the-mean return power.* The "clutter pulse" curve was obtained with the input being a product of noise and the triangular pulse, which is approximately what the actual sea-scattered signal will be at nadir. In this case, the input power will be equal to the mean-of-the-peaks of the input signal since the AGC is a "peak-picker" device. For the input power between -95.5 to -60.5 dBm, we see that the clean pulse curve requires 3 dB more input power than the clutter pulse curve in order to yield the same AGC output. From our previous reasoning, we note that the mean-of-the-peaks of the return power is thus equal to the peak-of-the-mean return power plus 3 dB. Therefore, for an input power range of -95.5 to -60.5 dBm and at nadir, the r-factor is -3 dB. Comparing this result with Lambert's computations and the simulation results in Figure 2B4, we see that the 3 dB agrees very well with the simulation result of 3.24 dB (0.69 in voltage ratio). We therefore conclude that the r-factor as derived from our simulation effort is substantiated by the data shown in Figure 2B5, of off-nadir angles of 3, 8, and 15.6 degrees is advisable.

*Since the input waveform is deterministic, the peak of the mean detected signal is equal to the mean of the peaks which is what the AGC measures.

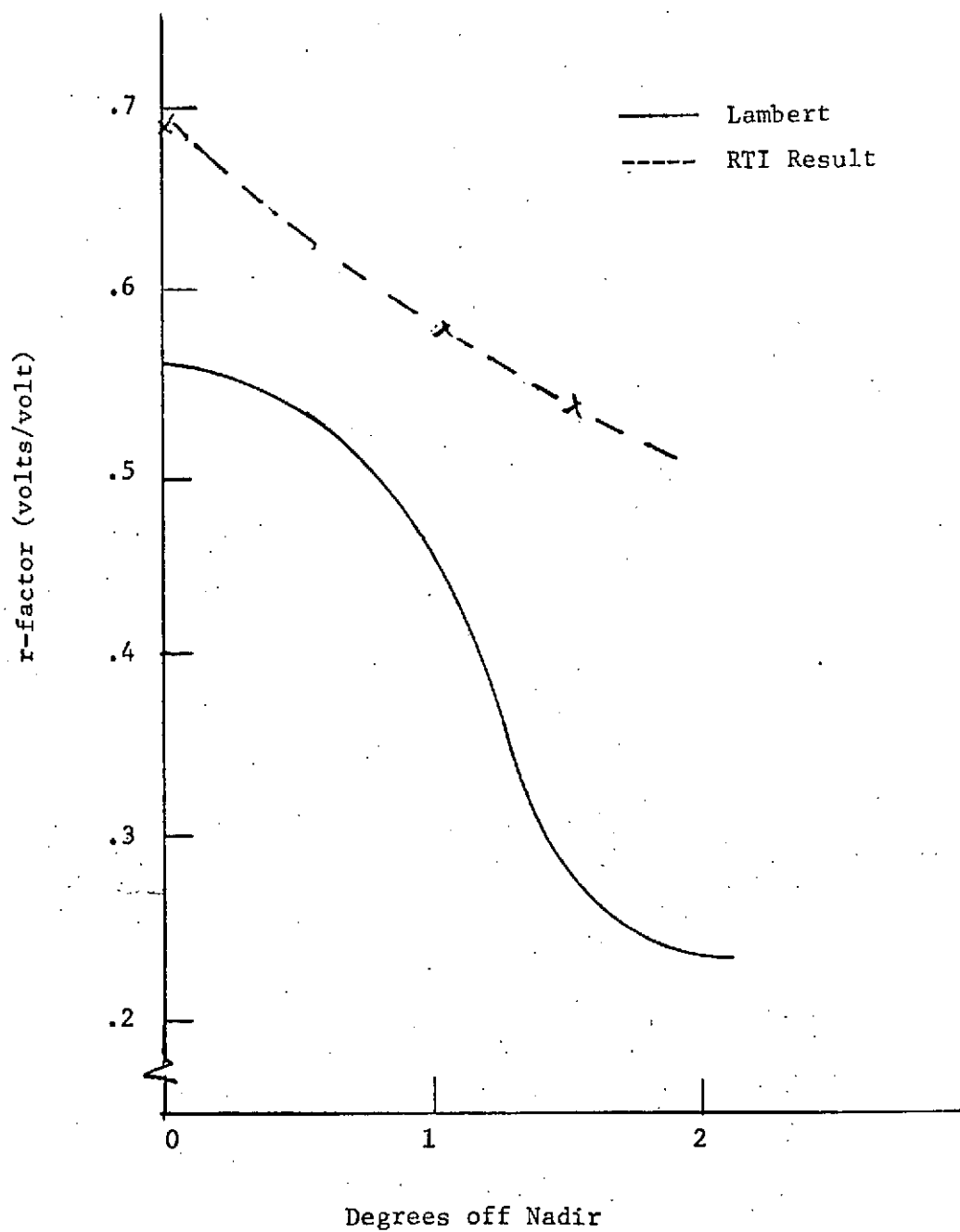


Figure 2B4. Comparison of r-factor results, 100 ns case.

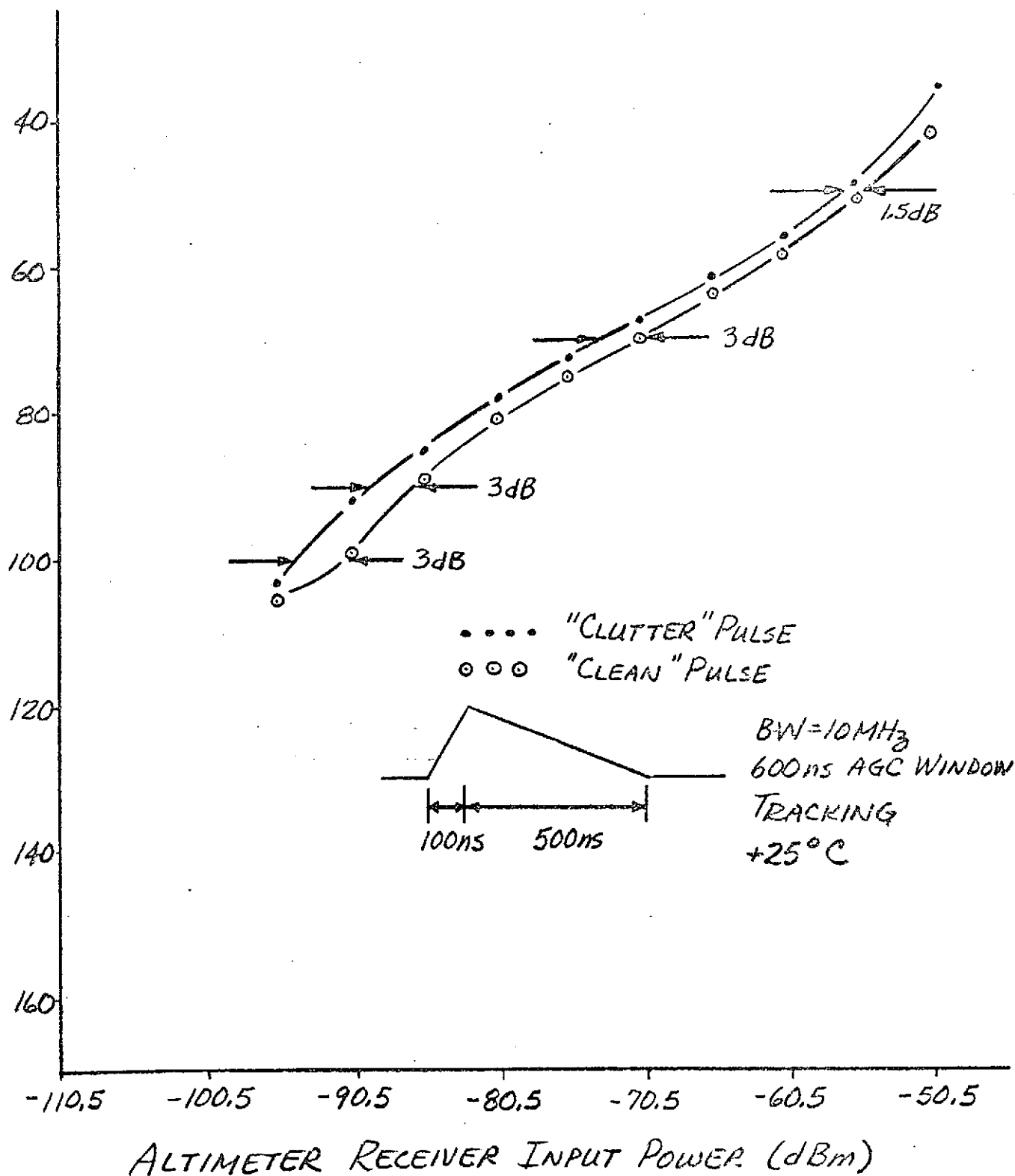


Figure 2B5. AGC calibration curve obtained by G.E.

Another interesting factor is given in Table 2BI below.

Table 2BI. r-Factor Versus Number of Waveforms Processed

<u>Number</u>	<u>r-factor</u>
1	.9992
2	.8761
4	.5892
8	.5436
16	.5588
32	.5491

These data correspond to an off-nadir angle of 1.5 degrees. The results show that an approximate steady-state condition should exist for the S-193 AGC time constant (~50 samples).

In summary, we feel that the comparisons shown identify a serious data processing information deficiency in regard to σ^0 measurement with the S-193 system. To solve this problem, we recommend that an r-factor study be conducted using the S-193 breadboard hardware in conjunction with pulse shaping circuits which approximate computed waveshapes over the range 0, 1.5, 3, 8, and 15 degrees off-nadir.

REFERENCES

- 2B1. Lambert, R., "Automatic Gain Control Loop Calibration Curve Analysis," G. E. System Tech. Memo., STM 2-3-LA, G.E., Utica, N.Y., February, 1971.
- 2B2. Rice, S. O., "Mathematical Analysis of Random Noise," in Selected Papers on Noise and Stochastic Processes, Edited by Nelson Wax, pp. 133-317, Dover Publications, Inc., New York, 1954.
- 2B3. "Analysis of Satellite Altimeter Signal Characteristics and Investigation of Sea-Truth Data Requirements," Final Report, Contract No. NAS6-1952, Research Triangle Institute, April, 1972.
- 2B4. "S-193 Microwave Radiometer/Scatterometer Altimeter," Calibration Data Report, Vol. 1B, Contract No. NAS9-11195, General Electric Co., October, 1972.

APPENDIX 2C

COMPUTER PROGRAMMING FOR TRACKER AND SAMPLE-AND-HOLD SIMULATION

Hardware Details for Waveform and Sampling Simulation

The analog computer used to generate the simulated ocean-scattered radar pulses was a EAI-380, and the 12-bit minicomputer used to simulate either the altimeter sample-and-hold gates (for waveform experiments) or the altimeter's splitgate tracker was a PDP8/e. The following list provides additional details of the hardware available for waveform and tracker simulation:

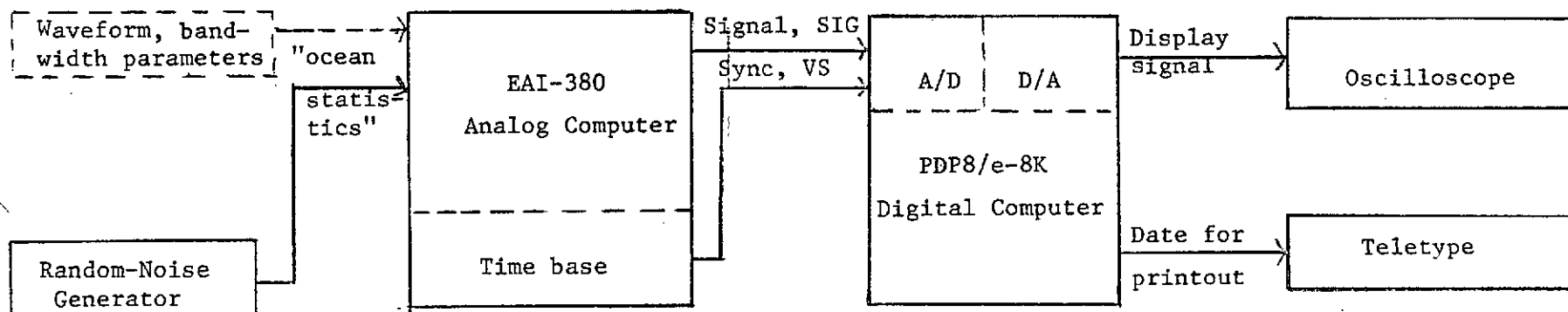
Available Laboratory Hardware

- 1 - PDP8/e Computer
 - 1 - Type KM8-E Memory Extension (total of 8K memory)
 - 1 - Type KE8-E Extended Arithmetic Element
 - 1 - Type AD01A A/D Converter with AH04 Sample and Hold Amplifier
 - 2 - Type AA50 D/A Converter
 - 1 - Type DR8-EA 12-Channel Buffered I/O
 - 1 - Type DK8-E Real-Time Clock
- (Above two items available but not used in the simulation described here.)
- 1 - EAI 380 Analog Computer
 - Storage scope, X-Y plotter, etc.

The relationship between the analog and the digital computers is presented in Figure 2C1. The analog computer is operated in a repetitive pulse mode of operation and the square-wave output from its time base is used as a synchronization or timing signal to one of the A/D channels of the digital computer. This sync signal will be denoted VS (the voltage for synchronizing) in the following discussion.

After satisfying synchronization criteria, the digital computer samples the simulated radar return pulse signal, denoted SIG in the following. After sampling a preset number of return radar pulses, the results are displayed on an oscilloscope or are printed out on the computer's Teletype unit.

The digital computer programming was done in the PDP8 assembly language to produce a large, general-purpose sampling subroutine which could handle



2-63

Figure 2C1. Relationship between Analog and Digital Computers.

either the altitude tracker or the waveform sampling functions as desired; this subroutine is called from FOCAL, the BASIC-like conversational language available on the PDP8. We used FOCAL to handle the details of formatting, I/O, and so forth, but used the assembly language sampling subroutine for its speed and efficiency and because of the specific control required for timing details.

General Sampling Subroutine Structure

To discuss our sampling subroutine, we use the terms gates, weights, and individual samples whose relationship is shown schematically in Figure 2C2. All timing is relative to the zero-going transition of the sync signal, VS, and the three important relative delay parameters d_1 , d_i , and d_b are also indicated in the figure. The entire sampling sequence is started a variable delay time, d_1 , from the sync signal's zero transition. There are a total of N_G gates, with each gate consisting of a total of N_w individual samples. The individual samples are multiplied by different weights, W , and the result for a given gate is a weighted sum, $(\text{sample}_1 \times W_1 + \text{sample}_2 \times W_2 + \text{sample}_{N_w} \times W_{N_w})$. A delay, d_i , between each weighted sample within a gate determines the total gate width. At the end of each gate a delay, d_b , determines the between-gate spacing.

The delays d_1 , d_i , and d_b are implemented by a counting loop which, in effect, uses the basic computer cycle as a clock. The N_G gates are all equal in width, equally spaced in time, and have identical weighting within the gate; this entire sequence is "free-running" when started at d_1 after the sync zero. The basic computer timing cycle thus provides the relative spacing for the entire sampling sequence, with the sync details providing the absolute time reference.

In our sampling subroutine, the maximum number of gates is 128, with each gate comprising from 1 to 128 individual samples - consequently there is a maximum of 128 weights. At the end of each sequence of ≤ 128 gates, the gate results update a set of ≤ 128 separate gate sum locations, so that the program accumulates a running mean. (As a minor point of interest, we also store a set of ≤ 128 squares of individual gate results; the gate variances can be obtained, if desired, from the sum of squares and the square of the sum of individual results.)

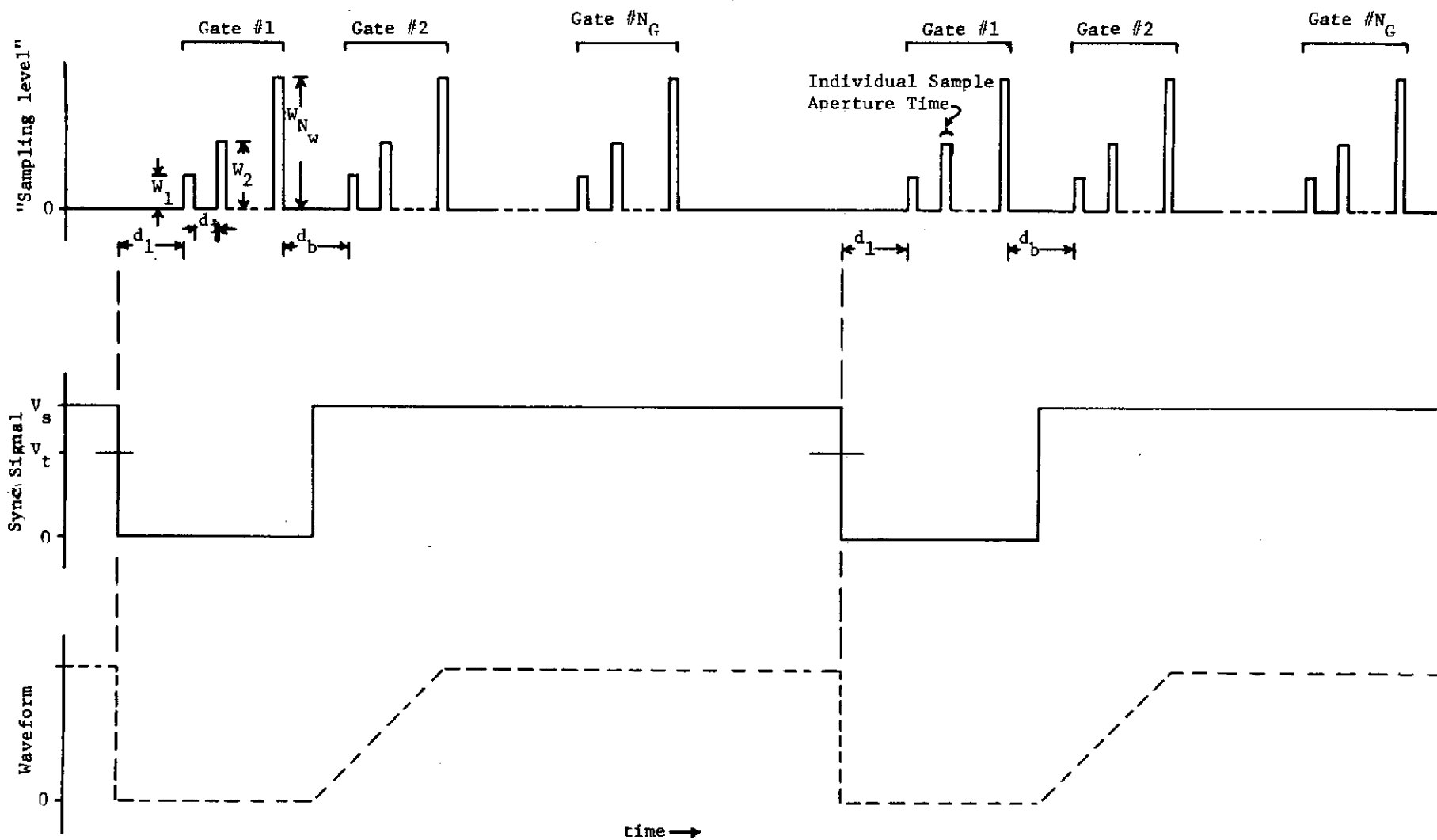


Figure 2C2. Time Relationships in Sampling Subroutine.

Uses of the Sampling Subroutine

To use the sampling subroutine for a simple waveform sample, we set $N_w = 1$, set weight $W_2 = 1$, adjust the delay parameters d_1 and d_b as desired, and set N_G for anywhere from 1 to 128, to obtain a set of N_G point samples on the waveform as averaged over N_S sample cycle (that is, over N_S successive simulated returns).

For use as a split-gate tracker, we set $N_G = 2$, set $N_w = 128$, all weights to $1/128$, adjust d_1 as appropriate, set d_1 so that the gate width is correct, and set d_b as appropriate for the time-separation of the two gates. In order to use the sampling subroutine for closed-loop tracker simulation, the two gate results must be transferred back to the main FOCAL program where the operation "first gate minus half the second gate" is performed, and the closed loop transfer characteristics are used to calculate the new position of the tracker. This position is set into the sampling subroutine as a new value of the delay-from-sync parameter d_1 .

Finally, the use of the sampling subroutine to simulate a set of eight sample-and-hold waveform sampling gates is straightforward; set $N_G = 8$, adjust widths by d_1 , set $d_b = 0$ (to obtain immediately adjacent gate results), and set the N_w and the individual weight values as appropriate to the characteristics of the sample-and-hold gates. If the sample-and-hold acts as a perfect integrator, all weights would be equal. If the sample-and-hold acts as a final-value-only hold, all weights would be zero except for the last which would be 1. A case intermediate between these extremes would be the sample-and-hold having a RC-type of behavior, and in this case the weighting would be maximum at the final weight and exponentially reduced from this at progressively earlier weights.

Computer Program of Sampling Subroutine

There is little point in reproducing program listings for the sampling subroutine just described. The listing is not only machine-dependent but also would be confusing since the subroutine is part of a general package which includes a floating point variable storage and recall area, an integer storage and recall area, and a routine to repetitively display on the oscilloscope (via the D/A converters) the contents of the integer storage area. The interrelationships of these functions and their relationship to the overall FOCAL system plus standard 8K FOCAL overlay have led to several different parts of the sampling subroutine being located in various discrete positions in the memory of the computer.

While a complete listing is not provided, an overall flow chart for the sampling subroutine is shown in Figure 2C3. The delays are identified merely as blocks, whereas actually the delay operation involves counting up in a loop. Input parameters include the delays DL, DI, and DB (d_1 , d_1 , and d_b respectively), information specifying channel and gain for the A/Ds for both the sync signal VS and the waveform channel SIG, the sync threshold VT, and the desired total number of complete sample cycles NS. Three separate subroutine entry points are indicated, and their differences are as follows: Entry 1 loads the complete set of parameters and the full set of sample weights, sets all results to zero and starts the sampling; Entry 2 sets results to zero and starts the sampling for parameters and weights as already loaded; and Entry 3 permits acquiring additional sample cycles for a new higher value of NS. The actual number of complete sample cycles acquired is variable NT, and the results are stored in the array RESULT(I), $I = 1$ to NG, where NG is the number of gates. (Although not shown on the flow chart, an additional array RESULT2(I) stores the sum of squares of individual results for variance calculations.) Two loops are involved in the details of synchronizing with VS; the first loop checks to see that VS exceeds the threshold VT, and when this is satisfied the second loop waits until VS falls below VT which occurs on the sync signal's trailing edge transition to zero.

One additional function indicated in the flow chart is provided by variables MAX and TMAX. TMAX stores the highest individual sample point obtained for each single sample cycle (during which a total of $NG \times NW$ individual sample points will have been acquired), and MAX contains the sum of the TMAX values. This provides information needed in an investigation of the peak-of-the-mean vs. mean-of-the-peaks problem, the r-factor problem described in Appendix 2A of this report.

On subroutine exit, the results RESULT(I) [and RESULT2(I)], NT, and MAX are available to the main FOCAL routine. All subsequent processing and print-out is done there.

Discussion

The sampling subroutine as described has been implemented in a "real-time" situation. We indicate real-time in quotation marks, because the radar pulse times and bandwidths have been scaled to fit the capabilities

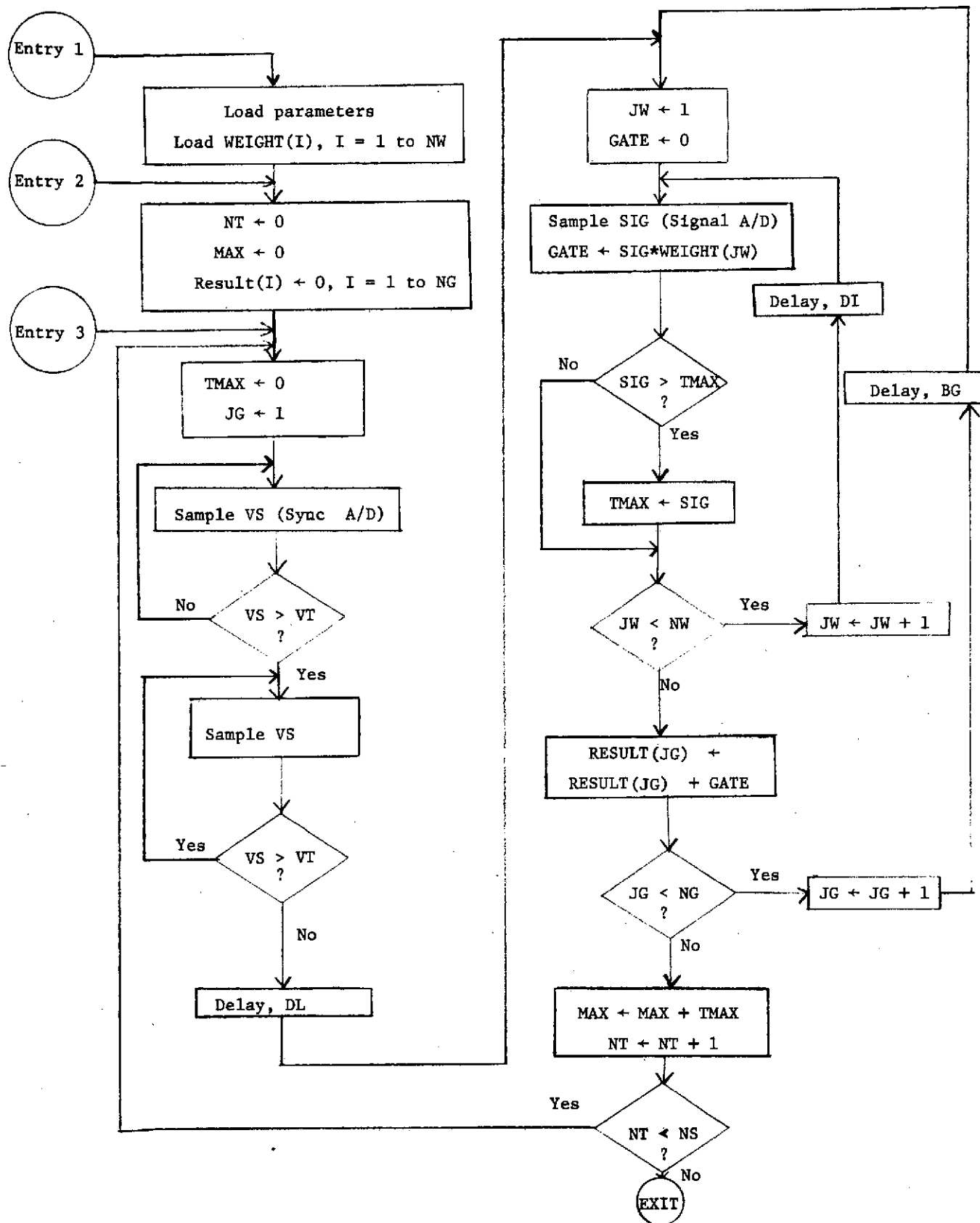


Figure 2C3. Flowchart for Sampling Subroutine.

of the available analog and digital computers. One could consider situations in which the digital computer input might be magnetic tape containing already-digitized data. A straightforward FORTRAN program could be written to accomplish the general operations indicated in Figure 2C2. The flow chart of Figure 2C3 would be changed only at the details of synchronization, and by writing "READ SIG" in place of "Sample SIG (signal A/D)" and "READ VS" in place of "Sample VS...". The delay operations would be different in detail; rather than counting in a loop, the "Delay, DL" operation would consist of skipping a number (related to DL) of digitized samples from the input tape (and similarly for delays d_i and d_b).

CHAPTER 3

TASK E. GEOS-C SATELLITE PROGRAM

3.0 INTRODUCTION AND SUMMARY

This chapter presents the results from investigations conducted under Task E, the contract task which is related to the GEOS-C satellite program. A summary of the contents of each subsequent section of Chapter 3 is provided immediately below.

Altimeter data processing objectives and requirements are examined in Section 3.1 in terms of signal-processing characteristics of the presently planned altimeter hardware. Data considerations related to the acquisition of altitude data, geodetic slope data, and waveform information are discussed relative to basic characteristics of the altimeter data which derive from the on-board altitude tracker and the effective illuminated area.

Section 3.2 gives estimates of the signal-to-noise ratio (SNR) under which we expect the equipment to operate, and presents recommendations for system-level tests relative to SNR.

Section 3.3 considers telemetry data rate requirements necessary to support the presently planned experiments. We find that low and high data rates of 300 and 9000 bits/sec are needed.*

The final section, 3.4, reviews presently planned calibration and qualification tests and gives recommended additions.

An appendix to this chapter discusses the finite radar spot size's smoothing effects and the consequent limitations on surface feature measurement; a possible computational program to predict such effects is described.

3.1 Altimeter Data Considerations

The General Electric Company (GE), the GEOS-C hardware contractor, is presently planning to design the altitude tracker to have a closed loop bandwidth of approximately 4 Hz, for use in all modes except acquisition. The resulting filtering due to the tracker loop is to be followed by an on-board averaging process which will also affect statistical properties of the altimeter data. Autocorrelation properties of the tracker output and the tracker-plus-averager output are shown in Figure 3.1 for inputs that are uncorrelated.

*At this time, it is planned to telemeter only 10 sample-and-hold (S&H) gate values. If all 16 S&H values are telemetered, the required data rate is approximately 14,000 bits/sec.

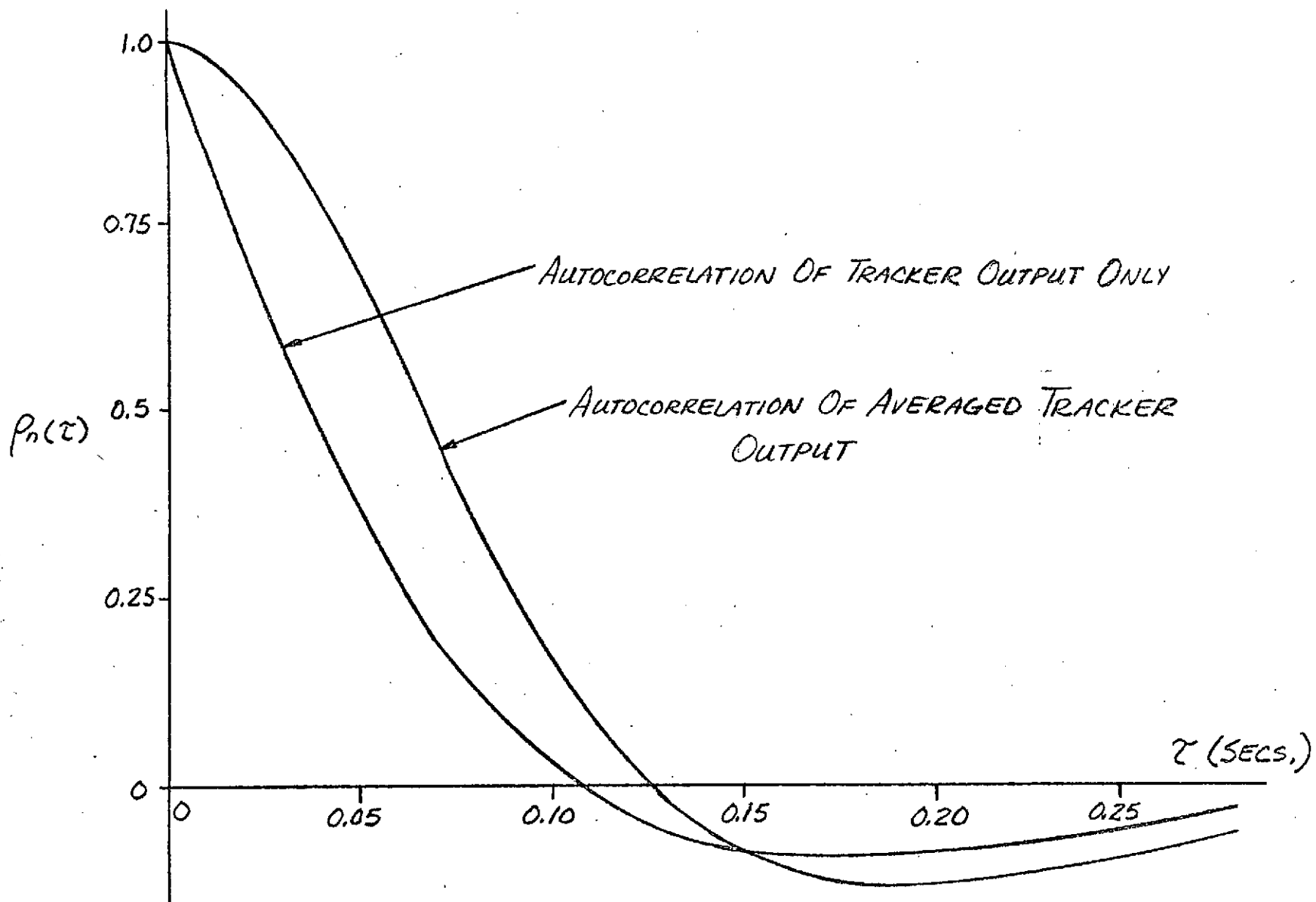


Figure 3.1. Autocorrelation functions for tracker output and averaged tracker output.

(Derivation of these quantities will be given in 3.1.1.). Examination of Figure 3.1 shows that the correlation span is correspondingly longer for the averaged output,* and the detailed calculations given in 3.1.1 show the averaged output data will be essentially statistically independent over 0.1 second intervals. Also note that present plans are to telemeter the tracker error signal in synchronism with each received pulse. Thus, in principle, the altitude error signal for each pulse will be available for post-flight data reconstruction; this reconstructed signal should be free of most on-board tracker constraints.

The selection of on-board processing characteristics should be subject to the following considerations:

- 1) For altitude measurements only, there is a consensus of opinion that averaging altitude data points over a one-second time period will be necessary to yield satisfactory variance properties in the geodetic data. On the basis of designing to a particular altitude noise level per unit time, it makes little difference whether the averaging is accomplished in the hardware or on the ground. This statement of course assumes that the on-board tracking and averaging devices are statistically near-optimum.
- 2) A second (and generally misunderstood) requirement derives from the need for obtaining geodetic slope data. Note that a slope measurement is akin to a differentiation process, and the data processing techniques would be expected to differ from those of altitude measurement. The work of Cohen and Zondek (ref. 3.1) indicates that a considerably higher data rate may be needed for this purpose. It has been suggested that the maximum data rate of 100 altitude samples per second may in fact be best. This subject is somewhat complex; in a continuous-time analogy it represents estimation of the derivative of a stochastic process. In the discrete case, some forms of measurement noise can be shown to lead to a solution involving a minimum in the relationship between error and sample rate. This is in contrast to the usual practice of sampling a function at the highest practicable rate, a valid viewpoint for deterministic processes but not necessarily appropriate for stochastic processes.
- 3) System parameters chosen to optimize data collection for either altitude or slope measurements, as in 1 and 2 above, are not necessarily best for

*These results are somewhat different from those contained in the GE proposal, mainly because GE used a $\frac{\sin x}{x}$ approximation of tracker bandwidth effects.

purposes of waveform experimentations. We feel that a second, narrower bandwidth option should be available in addition to the presently planned 4 Hz bandwidth. The reasons are:

a) For waveform measurements this narrow bandwidth would be desirable to avoid having to attempt tracker motion reconstruction with the attendant risk, telemetry problems and data processing complexity. With a 4 Hz bandwidth, tracker jitter will be approximately one half the pulse length (for moderately high SNRs); reduction of the bandwidth to 0.5 Hz, for instance, would reduce the variance by about a factor of three. This reduction should yield acceptable mean waveforms based upon on-board averages.

b) The lower bandwidth value should constitute an aid to acquisition since, in the final step, the signal must be determined to within ~ 20 nanoseconds (ns) from a 200 ns uncertainty. Detailed calculations for a Swerling II model show that from .5 to 1 second of search time is required to produce acceptable detection and false alarm probabilities. Because of the altitude rates possible, the tracker should be able to maintain its slew rate (from the previous 200 ns tracking step) during the search interval. Therefore, a narrow tracker bandwidth would be desirable for acquisition.

c) The lower bandwidth would permit acquisition of altimeter data in the global mode without further on-board averaging; it may also represent a better match to averaging characteristics of the footprint effect to be discussed in the next paragraph. Control loop calculations have been performed for a 0.5 Hz cross-over bandwidth based on velocity and acceleration values of 660 ns/sec and 6 ns/sec^2 * respectively; the results show that the tracking error is ~ 1 ns. The corresponding velocity and acceleration coefficients are approximately .1000 and 10. These figures thus indicate that a 0.5 Hz bandwidth, Type 1 servo is capable of accommodating the target dynamics involved.

4) In general, tracker bandwidth can be shown to be the determining

*This acceleration is larger than the orbit derived value, and is based on differentiation of a curve fitted to the Puerto Rican Trench data of Von Arx.

factor in establishing short term correlation properties of the ensuing altitude data; however for studies in which ocean-surface variations comparable to the illuminated spot size are of interest, tracker bandwidth effects are probably not the dominant process. Appendix 3A presents our preliminary work in this area; we argue that the tracker bandwidth determines the rate at which statistically independent estimates of the smoothed ocean surface process can be obtained, but that there is a smoothing function resulting from the (pulse-limited) spot size which may dominate the short term ocean surface autocorrelation characteristics. Quantitative values cannot be given at this time, and more work is definitely needed in this area.

With these remarks on GEOS-C data acquisition philosophy, we turn to an analysis and discussion of altimeter instrument-determined data characteristics.

3.1.1 Analysis of Altimeter-Data Variance Characteristics as Influenced by the On-Board Tracker.— This section presents results relating to the statistical characteristics of the altimeter output data, under the assumption that each returned pulse represents a statistically independent quantity. The analysis parallels that given in the GE proposal (ref. 3.2) and page references from GE's proposal are cited. The principal difference here is that the exact transfer characteristic of the tracker is used. We find that the presence of the on-board averager has an effect on the statistical properties of the intensive mode output data no different from that obtainable by a corresponding change in tracker bandwidth.

With the closed loop tracker transfer function (given on GE's page 1.a.2-160) as

$$B(s) = \frac{\frac{K}{t_1} (t_2 s + 1)}{s^2 + \frac{(1 + K t_2)}{t_1} s + \frac{K}{t_1}}$$

using $s = j\omega$ where ω is radian frequency, the magnitude squared function is

$$\Phi(\omega) = B(s) B^*(s)$$

$$= \frac{(Kt_2)^2 \omega^2 + K^2}{t_1^2 \omega^4 + [1 - 2K(t_1 - t_2) + (Kt_2)^2] \omega^2 + K^2}$$

In these equations, K is the loop's velocity gain constant, denoted as $K_v = K_g K$ by GE's pg. 1.a.2-159. We next determine the autocorrelation by the transform

$$\rho(\tau) = 2 \frac{1}{2\pi} \int_0^\infty \Phi(\omega) \cos(\omega\tau) d\omega$$

which can be evaluated using the following integrals from page 411 of ref. 3.3 for $a > 0$, $b > 0$, $|t| < \pi/2$.

Integral 3.733, No. 1.
$$\int_0^\infty \frac{\cos(ax) dx}{x^4 + 2b^2 x^2 \cos(2t) + b^4}$$

$$= \frac{\pi}{2b^3} \left[e^{-ab \cos(t)} \right] \frac{\sin[t + ab \sin(t)]}{\sin(2t)}$$

Integral 3.733, No. 3.
$$\int_0^\infty \frac{x^2 \cos(ax) dx}{x^4 + 2b^2 x^2 \cos(2t) + b^4}$$

$$= \frac{\pi}{2b} \left[e^{-ab \cos(t)} \right] \frac{\sin[t - ab \sin(t)]}{\sin(2t)}$$

Using these, we get

$$\rho(\tau) = \frac{(Kt_2)^2}{2\sqrt{K/t_1}} \frac{e^{-\left[\sqrt{K/t_1} \tau \cos(t)\right]}}{\sin(2t)} \times \left\{ \begin{aligned} &\sin[t - \sqrt{K/t_1} \tau \sin(t)] \\ &+ \frac{t_1/t_2}{Kt_2} \sin[t + \sqrt{K/t_1} \tau \sin(t)] \end{aligned} \right\},$$

where
$$t = \frac{1}{2} \cos^{-1} \left[\frac{1 - 2K(t_1 - t_2) + (Kt_2)^2}{2Kt_1} \right]$$

Since
$$\rho(0) = \frac{(Kt_2)^2 \left[1 + \frac{t_1/t_2}{Kt_2} \right] \sin(t)}{2\sqrt{K/t_1} \sin(2t)},$$

the normalized autocorrelation function is

$$\rho_n(\tau) = \frac{\rho(\tau)}{\rho(0)},$$

$$\rho_n(\tau) = \frac{e^{-\left[\sqrt{K/t_1} (\cos t) \tau \right]}}{1 + \frac{t_1/t_2}{Kt_2} \sin t} \times \left\{ \begin{array}{l} \sin[t - \sqrt{K/t_1} (\sin t) \tau] \\ + \frac{t_1/t_2}{Kt_2} \sin[t + \sqrt{K/t_1} (\sin t) \tau] \end{array} \right\}.$$

The function R_1 , a function of N , is defined as

$$R_1 = \frac{N^2}{\sum_{q=0}^{N-1} \sum_{k=0}^{N-1} \rho_n(|(q-k)T_o|)}, \quad \text{where } T_o = \text{time between individual pulses.}$$

(See GE page 1.a.2-60, where R_1 is defined as the "variance reduction factor due to the average of N tracking gate values to obtain average two-way range delay estimates.") To determine the effect of averaging on $\rho_n(\tau)$, $K(\tau)$ for N pulses is defined by

$$K_N(\tau) = \frac{1}{N^2} \sum_{q=0}^{N-1} \sum_{k=0}^{N-1} \rho_n(|(\tau+q-k)T_o|),$$

$$[\text{clearly } K_N(0) = \frac{1}{R_1}]$$

(This K_N is the same as GE's $K_{\Delta T_{Rr}}$, pg. 1.a.2-57, the "covariance function of the random error in the average two-way range delay estimate.")

These equations have been evaluated for a closed loop bandwidth (B_L) of 4 Hz with the results as given in Table 3.1; graphed values were already given in Figure 3.1. Note that the tracker autocorrelation is <0.1 for $\tau \geq 0.1$ sec and that the averaged autocorrelation is .173 at $\tau = .1$ sec. Suppose the tracker bandwidth is reduced to approximate the averaged output. In the system variance term

$$\frac{\sigma_{\tau}^2}{R_1} = \frac{T^2 \left[\frac{7}{24} + \left(\frac{A}{\frac{S}{N}} \right) + \left(\frac{B}{\frac{S}{N}} \right)^2 \right]}{M \frac{\text{PRF}}{\pi B_L} R_1},$$

$$R_1 \text{ with } .1 \text{ sec averaging} = 1.71^*$$

$$R_1 \text{ without } .1 \text{ sec averaging} = 1.0$$

$$B_L \text{ with averaging} = 4 \text{ Hz}$$

$$B_L \text{ without averaging} = 4 \div 1.7$$

and to first order the variance is identical in the two cases. We therefore conclude that the 0.1 sec averager is superfluous.

For the one-second average of the intensive-data mode, the variance is

$$\begin{aligned} \frac{\sigma_{\Delta T_R}^2}{R_1} &= \frac{\sigma_{\tau}^2}{R_1} + \frac{\sigma_{\epsilon Q2}^2}{N} + \sigma_{\epsilon Q1}^2 \\ &= \frac{8.04}{16.53} + \frac{.22}{10} + 3.26 = (1.95 \text{ ns})^2, \end{aligned}$$

or 29 cm standard deviation in height, where the values from GE page 1.a.2-62 and -68 were used and R_1 was recomputed for $N = 100$.[†] This result shows the dominance of the last term; the standard deviation in height would be 27 cm if only this last term were present.

*This compares with the GE value of ~ 1.78 obtained by approximating the autocorrelation function as a $\sin(x)/x$.

[†]According to conversations with E. L. Hofmeister of GE, the ϵ_{Q1} term will be one-fourth the value given in the proposal.

TABLE 3.1

TRACKER AUTOCORRELATION FOR NO AVERAGING
AND FOR 0.1 SECOND AVERAGING

Time τ in seconds	Autocorrelation	
	Tracker Output Only	Averaged Tracker Output
0.00	1.000	1.000
.01	0.851	0.983
.02	0.711	0.939
.03	0.583	0.871
.04	0.469	0.786
.05	0.366	0.688
.06	0.276	0.582
.07	0.197	0.473
.08	0.131	0.366
.09	0.075	0.264
.10	0.028	0.174
.11	-0.009	0.098
.12	-0.038	0.035
.13	-0.060	-0.015
.14	-0.076	-0.055
.15	-0.087	-0.085
.16	-0.094	-0.107
.17	-0.097	-0.121
.18	-0.097	-0.130
.19	-0.094	-0.133
.20	-0.090	-0.133
.21	-0.084	-0.129
.22	-0.078	-0.123
.23	-0.071	-0.116
.24	-0.064	-0.107
.25	-0.056	-0.097
.26	-0.049	-0.087
.27	-0.042	-0.076
.28	-0.036	-0.066
.29	-0.030	-0.057
.30	-0.024	-0.045

3.1.2 Discussion of Altimeter Variance as Influenced by Digital Delay Gate Start Signal Quantization Error.— Next, we turn to a discussion of the term $\sigma_{\epsilon Q1}^2$ in GE's tracker variance equation

$$\sigma_{\Delta T_R}^2 = \frac{1}{R_1} \sigma_{\tau}^2 + \frac{1}{N} \sigma_{\epsilon Q1}^2 + \sigma_{\epsilon Q2}^2 .$$

The quantities here are:

$\sigma_{\Delta T_R}^2$ = variance of the random error ΔT_R in the average two-way range estimate,

σ_{τ}^2 = variance of the random zero-mean tracking error,

R_1 = variance reduction factor due to averaging N tracking gate delay values,

N = number of successive tracking gate values averaged for the two-way range estimate,

$\sigma_{\epsilon Q1}^2$ = variance of digital delay gate start signal quantization error,

$\sigma_{\epsilon Q2}^2$ = variance of digital delay gate stop signal quantization error.

Approximate numerical values for the tracker variance from the above equation and based upon GE's proposal (except for the R_1 values which are based on the previous discussion) are as follows:

$$\sigma_{\Delta T_R}^2 = \frac{8}{1.71} + \frac{.22}{10} + 3.26 \text{ (ns)}^2, \text{ for 0.1 second average (N=10), and}$$

$$\sigma_{\Delta T_R}^2 = \frac{8}{16.5} + \frac{.22}{100} + 3.25 \text{ (ns)}^2, \text{ for 1.0 second averages (N=100).}$$

The dominant term in the 1 second average is the 3.26 (ns)^2 from $\sigma_{\epsilon Q1}^2$; GE does not divide this variance by 10 (unlike the $\sigma_{\epsilon Q2}^2$ term)

because they state that, "...the quantization error ϵ_{Q1} is a slowly varying error. It may remain constant for time intervals on the order of seconds. Hence, ...assume it is fully correlated over the averaging time of N pulses," whereas ϵ_{Q2} is a rapidly varying error which can assume any value in the allowed range on a pulse-to-pulse basis and hence can be assumed completely uncorrelated pulse-to-pulse.

An extremely important question is the rate at which ϵ_{Q1} varies. Depending on that rate, the $\sigma_{\epsilon_{Q1}}^2$ term may be different from the indicated $3.26 \text{ (nanoseconds)}^2$. This is because $\sigma_{\epsilon_{Q1}}^2$ has been derived from the quantizing time step T_{Q1} under the assumption that the probability density function $p(\epsilon_{Q1})$ is uniform over the quantizing range as shown below:

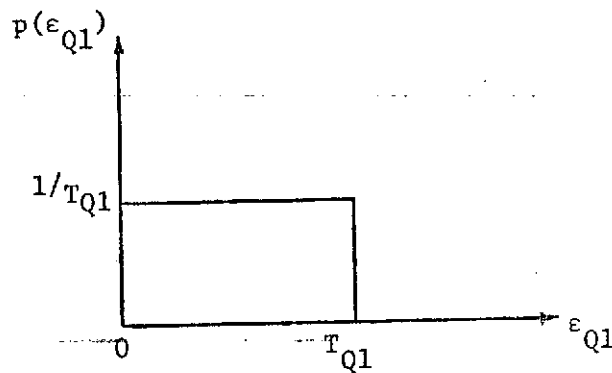


Figure 3.2. Probability density function for the error ϵ_{Q1} .

Under this assumption of uniform density, the mean and variance of the quantizing error are immediately found to be

$$\begin{aligned} \mu_{\epsilon_{Q1}} &= \int_{-\infty}^{\infty} p(\epsilon_{Q1}) \cdot \epsilon_{Q1} \, d\epsilon_{Q1} = \int_0^{T_{Q1}} \frac{1}{T_{Q1}} \cdot \epsilon_{Q1} \, d\epsilon_{Q1} \\ &= \frac{T_{Q1}}{2} \end{aligned}$$

$$\begin{aligned} \text{and } \sigma_{\epsilon_{Q1}}^2 &= \int_{-\infty}^{\infty} p(\epsilon_{Q1}) \cdot (\epsilon_{Q1} - \mu_{\epsilon_{Q1}})^2 \, d\epsilon_{Q1} = \int_0^{T_{Q1}} \frac{1}{T_{Q1}} (\epsilon_{Q1} - T_{Q1}/2)^2 \, d\epsilon_{Q1} \\ &= T_{Q1}^2/12 \end{aligned}$$

The same form holds for σ_{ϵ}^2 . For the intensive mode, the GE documents indicate $T_{Q1} = 6.25$ ns and $T_{Q2} = 1.58$ ns, leading to

$$\sigma_{\epsilon_{Q1}}^2 = \frac{(6.25)^2}{12} = 3.26 \text{ (ns)}^2$$

and

$$\sigma_{\epsilon_{Q2}}^2 = \frac{(1.58)^2}{12} = 0.22 \text{ (ns)}^2$$

But in order that $\sigma_{\epsilon_{Q1}}^2$ be representative for altitude data requires that the data be acquired over a long time span compared to the typical period of variation of ϵ_{Q1} in order that the assumption of uniform $p(\epsilon_{Q1})$ over the interval $(0, T_{Q1})$ is valid. Let τ_{DQ1} be the correlation time of ϵ_{Q1} , and we will consider three different cases depending upon whether τ_{DQ1} is much larger than, much smaller than, or of the same order of magnitude as t_o , where t_o is the altimeter observation period of interest.

Case 1. $\tau_{DQ1} \gg t_o$.

Suppose it were possible to profile exactly the same ocean area a number of separate times, each profile taken in a time t_o . Suppose that all factors except ϵ_{Q1} are constant. Then one could compare the m separate profiles obtained, and upon repeating the experiment for m large enough that $(mt_o) \gg \tau_{DQ1}$, the data would appear as in the following sketch, Figure 3.3.

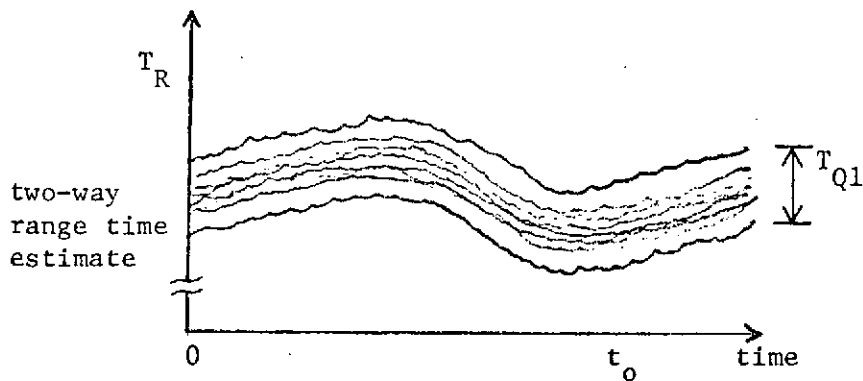


Figure 3.3. Possible data for a number of profiles of the same ocean area, for $\tau_{DQ1} \gg t_o$.

The point is that ϵ_{Q1} does not change during any single profile, that $\sigma_{\epsilon_{Q1}}^2$ would be related to the absolute altimeter accuracy, and that for local geoidal feature mapping (over a time span t_o or less) the relative accuracy of the profile is not affected by ϵ_{Q1} . That is, $\sigma_{\epsilon_{Q1}}^2$ defined by $T_{Q1}^2/12$ is related to the statistics of an ensemble of separate altitude measurements, and for practical reasons the actual altimeter will measure only one or two members of this ensemble of altimeter profiles. The manner in which ϵ_{Q1} should be interpreted depends on whether one's interest is in absolute or relative accuracy.

Case 2. $\tau_{DQ1} \ll t_o$.

In this case ϵ_{Q1} can be treated the same as ϵ_{Q2} . That is, the $\sigma_{\epsilon_{Q1}}^2$ is correctly given by $T_{Q1}^2/12$ and the contribution of $\sigma_{\epsilon_{Q1}}^2$ to $\sigma_{\frac{\Delta T_R}{\Delta T_R}}^2$ is reduced by a factor of N since ϵ_{Q1} is decorrelated in a short time compared to the observation time. The variance formula would then be

$$\begin{aligned} \sigma_{\frac{\Delta T_R}{\Delta T_R}}^2 &= \frac{\sigma_{\tau}^2}{R_1} + \frac{T_{Q2}^2}{12N} + \frac{T_{Q1}^2}{12N} \\ &= \frac{8}{1.71} + \frac{0.22}{10} + \frac{3.26}{10} \text{ (ns)}^2 \text{ for 0.1 second averages.} \end{aligned}$$

In this case ϵ_{Q1} poses no particular problem.

Case 3. $\tau_{D_{Q1}}$ and t_o of the same order of magnitude.

In this case any observed profile could contain one or several discrete jumps by T_{Q1} in the estimated range T_R . This means discrete altitude jumps of $(6.25 \text{ ns}, T_{Q1}) \times (.15 \text{ m/ns}, c/2) \pm 0.9 \text{ meters}$, and it is uncertain what the best procedure would be for removing this ϵ_{Q1} contamination from the altimeter data; possibilities range from simple data post-editing to time-varying Wiener filter implementation. It is worth remarking that changes of 0.9 meters in 0.1 second time intervals are small compared with the altitude rate of 100 meters/second which the tracker should accommodate.

Based on the discussion of the above three cases, it is clear that more detail is needed about statistical characteristics of ϵ_{Q1} . Cases 1 or 2 would be strongly preferable to Case 3, the intermediate case. If the time characteristic of ϵ_{Q1} falls into Case 3, it would be desirable to stabilize ϵ_{Q1} better in order to achieve more nearly a Case 1 situation.

3.2 Open Questions Regarding Estimated Values of Altimeter SNR

In this section we review some of the uncertainties that arise in the ~~calculation of received power~~. Such calculations must be regarded as approximations and engineering judgements and therefore used with due regard for needed safety factors. The three areas of uncertainty to be discussed are: first, what we have denoted the "threshold effect"; then, signal-to-noise-ratio (SNR) estimates; and finally, sea state experimentation.

3.2.1 The Threshold Effect.— The threshold effect in the context of GEOS-C represents a possible degradation in system accuracy for low SNR values, which the radar equation does not predict. The data to be discussed indicate that this effect might cause the intensive mode to be inoperative for moderate to large waveheight conditions.

The threshold problem is one of considerable theoretical complexity; we have been unable to locate published results that are directly applicable to the GEOS-C problem. The literature also used the terms global, ambiguity, and anomalous errors to describe the threshold effect. This effect represents one of the research areas of spread-spectrum techniques, and the results available in the literature are adequate only to identify the effect as a

potential problem area. The most recent textbook treatment of the problem is by Sakrison (ref. 3.4). He states (pg. 62),

"Note that calculating the probability that the global maximum of $|(\hat{s}_\beta, W)|$ falls outside the central interval is equivalent to solving a first passage time problem for a Gaussian process, a classical unsolved problem. The problem of how to calculate estimates of mean-square error in the threshold region, or even to calculate for what value of signal to noise ratio...threshold effects start to occur can be regarded as one of the important open problems in communication theory at the present time."

While the following paragraphs present the results of our brief study of the effect, we feel that the existing theoretical work is not sufficiently developed to justify the considerable effort which would be needed to analyze the specific GEOS-C system; instead we recommend that acquisition and tracking tests be made, as a function of estimated loop losses, with the GEOS-C pulse compression and altitude tracker hardware as early as possible in the progress.

Following are the results of our brief survey of the threshold effect. The paper which brought the subject to our attention is by McAulay and Hofstetter (ref. 3.5). In this paper, the authors focus on the threshold behavior of a chirp system through an analysis based on the Barankin bound.

They find that for a time-bandwidth product of 100 and a SNR of 2.5 dB, the range variance is 7 dB larger than that predicted by the Cramer-Rao bound (which should correspond closely to the radar equation result). They conclude that a linear 40:1 pulse compression system should operate at a SNR greater than 10 dB if meaningful unbiased range measurements are to be obtained. Two other important papers on the subject are by Seidman (ref. 3.6) and Glave (ref. 3.7). Both of these papers cast serious doubt on the utility of the Barankin theory. They show it to be a very loose and parametrically unstable bound which, for the cases considered, produces a very optimistic result. An abbreviated version of the Seidman result is shown in Figure 3.4, which indicates that the Barankin bound predicts performance in excess of the theoretical maximum (the classical Shannon bound). Both Seidman and Sakrison recommend use of the Cramer-Rao bound for the high SNR case and the Ziv and Zakai bound for the low SNR case. Seidman argues that the threshold can be located to within ± 2 dB with this theory, for a relatively wide class of waveforms; this paper shows

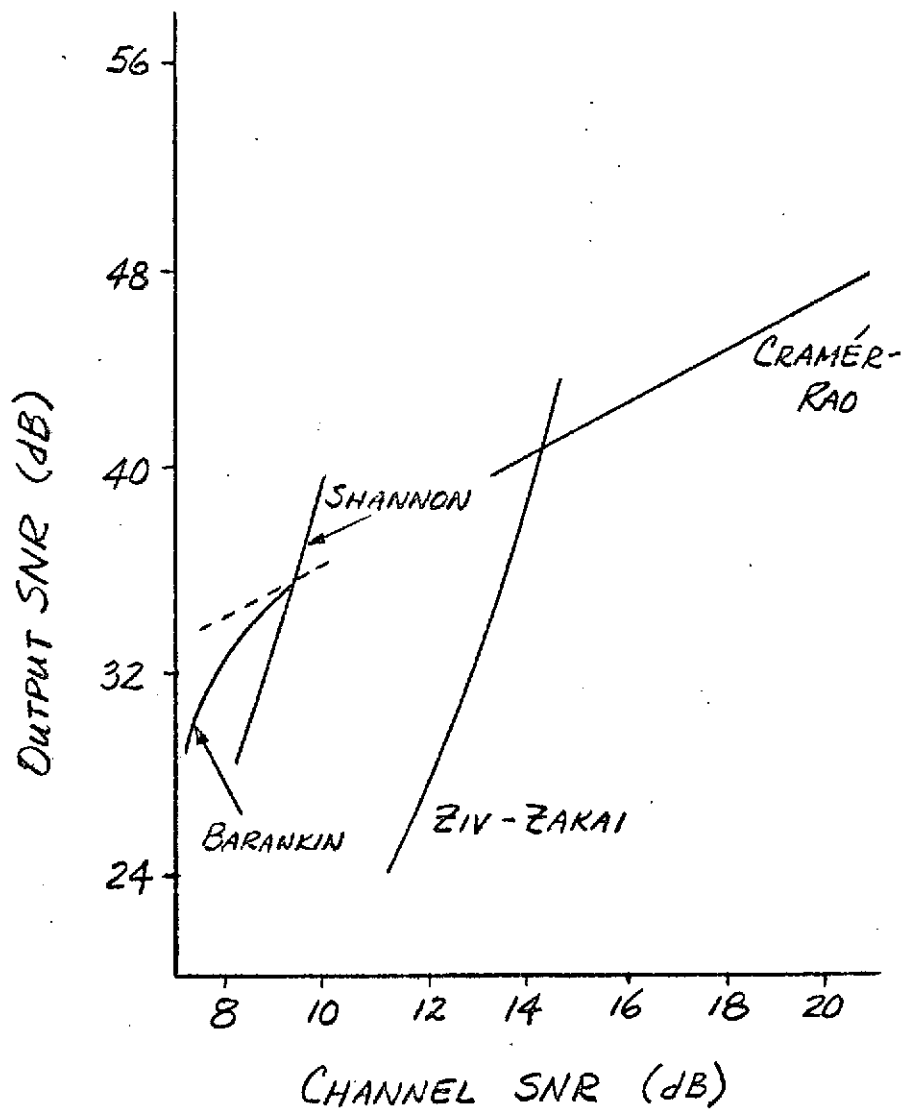


Figure 3.4. Noisy channel performance bounds for a time-bandwidth product of 40.

the threshold point to be between 14-18 dB for a time-bandwidth product of 80.

The papers thus far mentioned consider only point, non-fluctuating targets. To our knowledge, the only reference which considers other target characteristics is Van Trees (ref. 3.8). In this work, he considers a point Rayleigh-fluctuating target and derives error equations (p. 305) based on an approximate analysis. Figure 3.5 shows computed values based on his equations, for conditions we feel are close to the GEOS-C parameters. The Van Trees results are interesting; in this case a threshold behavior is encountered which is a function of the number of pulses available. Figure 3.5 shows this result and indicates that, for very low SNR values, a tracker which effectively operates on 10 samples (for example, a 5.0 Hz bandwidth and a prf of 100) will encounter range errors which are degraded by a factor of 10 compared to linear estimates. This theory involves a number of approximations and the results should be considered only qualitative; however, the tracker-bandwidth tradeoff is most interesting.

We discussed possible threshold effects in the altimeter during a telephone conversation with Mr. R. J. McAulay, and his comments and suggestions are as follows:

1. He definitely feels that the altimeter pulse compression system will exhibit threshold behavior and is not aware of any theoretical work relating to the extended, fluctuating target problem.
2. He recommends that the ability of the system to "maintain lock" be investigated via the Ziv-Zakai approach (point target) to determine if the global uncertainty exceeds the tracker "pull-in" range. As a consultant, he recommends Lawrence P. Seidman of Systems Control, Inc., Palo Alto, California.

3.2.2 SNR Estimates.— The SNR value given in GE's proposal is ~14 dB for the intensive mode, based on a calm-sea value for σ^0 of 9 dB. We estimate other system losses to be:

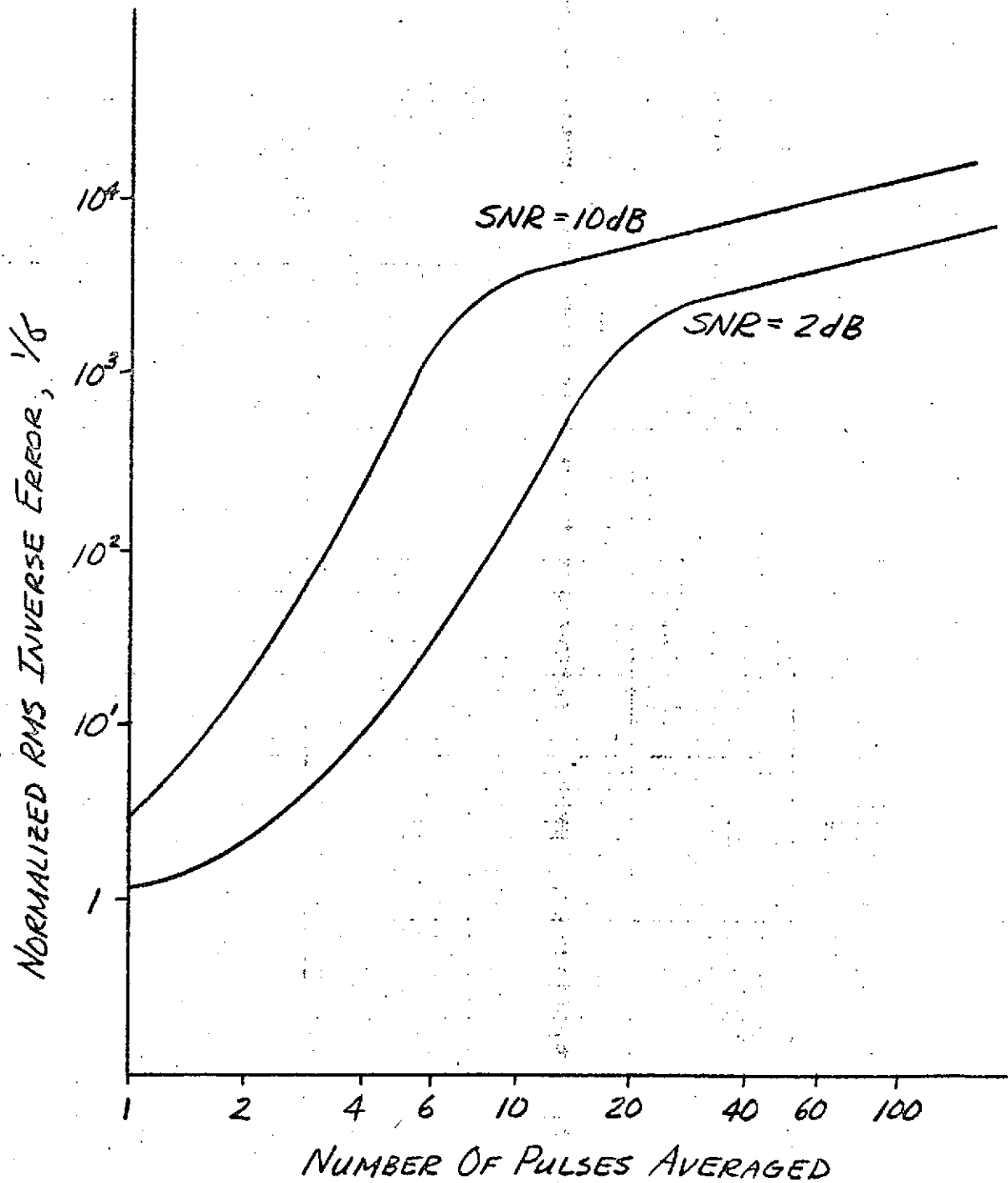


Figure 3.5. Tracker rms error as a function of SNR and number of pulses averaged, from Van Trees.

antenna pointing error (1 degree off nadir)	3.4 dB
pulse compression sidelobe filter loss	2.2 dB
miscellaneous degradation (power output, noise figure, atmospheric loss)	2 dB
Total	7.6 dB
Resulting SNR for calm seas	6.4 dB
Resulting SNR for SWH* 3-4 ft	3 dB
Resulting SNR for SWH ~6 ft	0 dB

Because of the marginal values of SNR shown, especially in regard to waveform data acquisition and to acquisition and maintenance of tracker lock, we recommend:

1) The pulse compression sidelobe filter should be omitted. For the above SNR values time sidelobes would not be important, and also the system bandpass properties will provide some degree of sidelobe modification.

2) The satellite altitude should be reduced by approximately 20% to achieve higher effective SNR.

3) Again, system tests including pulse compression and the altitude tracker should be conducted as early as possible to document system performance for SNRs near 0 dB, particularly in the area of non-linear detection characteristics.

3.2.3 Sea State Experimentation.— Sea state measurement will degrade with SNR primarily because:

1) The increased noise baseline will cause the signal component to be a smaller percentage of the recorded waveform. Therefore the uncertainty in measuring signal properties will be greater.

2) At low SNR values the tracker variance will increase and S&H position uncertainty will become greater. Note that the S&H circuits will be tied to the range tracker and that time jitter (tracking error) will be superimposed on the on-board average waveforms.

In view of the potential degradation in range error due to the threshold effect, Category 2 is considered to be the most important error component, particularly since the S&H jitter is related to the high intensity mode tracker-bandwidth. For example, if the one second tracker jitter is .50 meter,

*Significant Wave Height

the 10/second sample-rate jitter would be 1.5 meters or about one pulse length. These figures indicate that the considerable advantage of accumulating on-board average waveforms may be lost. Also note that previous studies have recommended that sea state experimentation emphasize rough sea conditions (see ref. 3.9). Present SNR estimates indicate this would not be advisable, even disregarding the threshold effect. The task of demonstrating the sea-state measurement concept is more difficult for small wave-heights.

A problem associated with waveform studies is that of measuring signal fluctuation statistics. Recent data from the Wallops/NRL aircraft program suggest that present statistical scattering models may be of limited validity. The requirement for relatively clean individual waveforms is more stringent here than in any of the experiments considered. Study may in fact show that this measurement is of limited usefulness for the SNR constraints encountered.

3.3 Telemetry Requirements

Tables 3.2 and 3.3 show the values which we consider to be minimum ~~and maximum~~ telemetry requirements for the various signal categories. These tables are largely based on the instrument data characteristics shown in Table 3.4 (which is taken from the GE proposal). The low data rate result shows that ~300 bits/sec are required unless the plateau gate is sampled every pulse. The plateau gate probably need not be sampled at this rate since the assumption of statistical independence of each sample and ocean surface homogeneity will allow a slower data accumulation rate (~10/sec).

In the high data rate case, the instantaneous plateau gate data are omitted since they are duplicated by the S&H data. Table 3.3 shows a bit rate of approximately 9000 bits/sec is needed if 10 S&H values are telemetered and a bit rate of 14,000 bits/sec is needed if all S&H values are used. Note that the tracker error signal is the second largest item in Table 3.3. This arises since tracker reconstruction considerations dictate that this quantity be densely sampled.

TABLE 3.2

LOW DATA RATE TELEMETRY SUMMARY

		Bit Rate (BPS)	
		Min	Max
I. Low data rate parameters			
<u>Housekeeping quantities</u>			
Approx 6 values, 8 bits each		5 (1/[10 sec])	48 (1/sec)
<u>Clock Data</u> (20 bits/minute)		nil	
<u>System Outputs</u> same as I-mode 2/sec		10 (1/[10 sec])	192 (2/sec)
II. Medium data rate parameters			
<u>Status Words</u> 8 bits, 1/sec.		8	8
<u>AGC</u> 8 bits		16 (2/sec)	80 (10/sec)
<u>Altitude word</u> upper 16 bits, 1/sec.		16	16
<u>Tracker error signal</u> 8 bits, 1/sec.		8	8
III. High data rate parameters			
<u>Altitude word</u> 16 bits, 10/sec.		160	160
<u>Inst. plateau gate</u> 8 bits		80 (10/sec)	800 (100/sec)
Total		298	1312

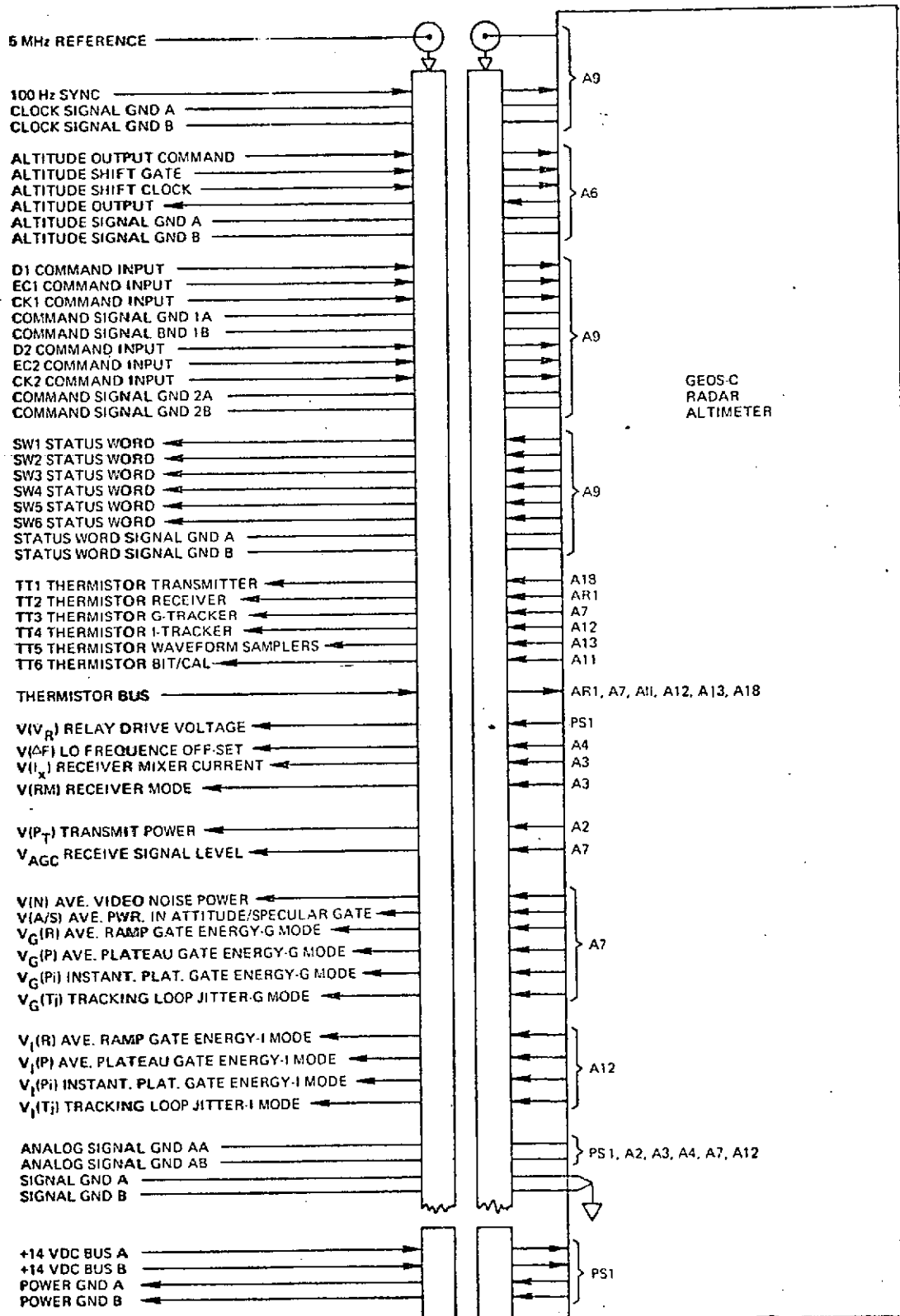
TABLE 3.3

HIGH DATA RATE TELEMETRY SUMMARY

		Bit Rate (BPS)	
		Min	Max
I. Low data rate parameters			
<u>Housekeeping quantities (temp. & voltage)</u>			
Approx. 6 values, 8 bits each		5 (1/[10 sec])	48 (1/sec)
<u>Clock Data</u> (20 bits/minute)		nil	
<u>System outputs*</u> - typical quantities:			
avg. noise power, avg. specular gate, avg. ramp gate, avg. plateau gate, calib. data, average waveforms, loop lock signal assume 12 parameters @8 bits		10 (1/[10 sec])	192 (2/sec)
II. Medium data rate parameters			
<u>Status words</u> 8 bits, 1/sec		8	8
<u>AGC</u> 8 bits		16 (2/sec)	16 (10/sec)
<u>Altitude Word</u> upper 16 bits, 1/sec		16	16
III. High data rate parameters			
<u>Altitude Word</u> 16 bits, 10/sec		160	160
<u>Tracker error signal</u> 8 bits, 100/sec		800	800
Subtotal		1010	1304
Waveform sample and hold data 100/		8000 (10 S&H)	12,800 (16 S&H)
Total		9010	14,104

*Note that the instantaneous plateau gate is omitted in the I mode.

TABLE 3.4
GEOS-C ALTIMETER DATA OUTPUTS
(From GE Proposal, Figure 1.a.1-5)



3.4 Recommended Calibration Tests

Altimeter system level electrical tests have been examined with reference to the test categories utilized in recent GEOS-C meetings. These categories are listed and defined below:

A. Functional Tests

These tests constitute verification of the proper sequencing and appropriate responses of all mode commands which can be exercised after the satellite is in orbit. As such, these constitute the most isolated or "buttoned-up" form of electrical test. Tests will be under the control of the TAMS system and altimeter input will consist of clean signals applied via waveguide or RF inputs.

B. Subsystem Performance Tests

These tests consist of data acquisition of the subsystem (e.g., tracking loop) and major component level (e.g., antenna), and of tests based on use of built-in test/calibrate functions. From an engineering standpoint, these tests will provide the most detailed information available on the system.

C. System Performance Tests

These tests constitute verification of the performance of the major system functions such as acquisition, altitude measurement, average waveform measurement, signal fluctuation probability density measurement, and drift-rate/bias tests on these parameters.

D. Engineering Data/Calibration Data Tests

These tests will culminate in a final calibration data book which will provide the prime data base for experiment investigators. The data base will represent results of tests defined in this category and all appropriate test data obtained from other test categories.

In the efforts reported herein, we have attempted to place ourselves in the position of a GEOS-C investigator and to examine present test plans in terms of experiment requirements. On this basis our results apply only to categories B and D of the intensive mode. In presenting these findings, the information covered by E. L. Hofmeister at the 8 November 1972 Status Review meeting is given in Tables 3.5-3.9; our recommended test additions are given in Tables 3.10 through 3.12. These items are considered to be self-explanatory in view of previous discussions, and will not be individually examined here.

TABLE 3.5

SUBSYSTEM PERFORMANCE TESTS - GLOBAL MODE

1. Transmitter

- Peak power
- RF frequency/pulse spectrum
- Pulse shape - single and burst
- PRF
- Burst pulse spacing
- Transmit pulse time jitter
- Transmit loss

2. Antenna

Performance measured at lower level; antenna assembly.

3. Receiver

- Noise figure
- Receive loss
- AGC/Tracking sensitivity
- Receiver dynamic range
- AGC dynamic range
- AGC dynamic range
- AGC linearity
- Receiver bandwidth; bandpass characteristic
- Detector; performance measured at lower level
- Video bandwidth; frequency response to AGC loop
and waveform samplers

4. Signal processor

- a. AGC loop
 - Loop bandwidth; frequency response (acquisition and
 - Loop step response tracking)
- b. Tracking loop
 - Gate configuration; width, spacing, and spacing for burst
 - Loop bandwidth; frequency response
 - Loop step response
 - Loop response to ramp input
 - Track gate step size
- c. Altitude output
 - Averaging process

TABLE 3.6

SUBSYSTEM PERFORMANCE TESTS - INTENSIVE MODE

1. Transmitter

- Peak power
- RF center frequency
- Pulse spectrum
- Pulse shape
- PRF
- Transmit pulse time jitter
- Transmitter phase shift
- Transmit loss

2. Antenna

Performance measured at lower level; antenna assembly

3. Receiver

- Noise figure
- Receive loss
- AGC/Tracking sensitivity
- Receiver dynamic range
- AGC dynamic range
- AGC linearity
- Receiver bandwidth; bandpass characteristic
- Signal-to-noise ratio improvement
- Time sidelobe levels
- Compressed pulse shape
- Detector; performance measured at lower level
- Video bandwidth; frequency response to AGC loop, tracking loop, and waveform samplers

4. Signal Processor

- a. AGC loop
 - Loop bandwidth; frequency response (acquisition and tracking)
 - Loop step response
- b. Tracking Loop
 - Gate configuration; positions, widths, and spacing
 - Tracking gate step size
 - Loop bandwidth; frequency response
 - Loop step response
 - Loop response to ramp input
- c. Altitude processing
 - Averaging process
- d. Waveform sampling system
 - Sample gate width
 - Number of sampling gates
 - Sample gate spacing
 - Reference time for sampling gates

TABLE 3.7

SUBSYSTEM PERFORMANCE TESTS - GLOBAL & INTENSIVE MODES BUILT-IN TEST/
CALIBRATE

1. Time delay calibration

Instrument delay bias measurement; internal vs.
external measurement

2. Transmit/receive power calibration

3. Receiver/AGC calibration

Shape and level of IF signal #1
Shape and level of IF signal #2

4. Signal processor calibration

Shape of video test waveform #1
Shape of video test waveform #2

TABLE 3.8

SYSTEM PERFORMANCE TESTS

Global Mode Tests

GM 1	Acquisition Test
GM 2	Height Measurement Test
GM 3	Instrument Drift Rate Test
GM 4	Instrument Bias (Calibrate/Test) Test

Intensive Mode Tests

IM 1	Acquisition Test
IM 2	Height Measurement Test
IM 3	Instrument Drift Rate Test
IM 4	Instrument Bias (Calibrate/Test) Test
IM 5	Average Impulse Response Test
IM 6	Echo Amplitude Probability Density Test

TABLE 3.9

ENGINEERING DATA/CALIBRATION DATA TESTS

- A. Final calibration data package consists of data from these tests plus selected data from performance tests
- B. Some important engineering/calibration data
1. Transmit pulse shapes: photos of RF and detected RF transmit pulses
 2. Point target return pulse shapes: couple transmit pulses into receiver and photograph pulses at pre-compression IF test point, IF test point, and video test point
 3. AGC calibration curves: AGC control voltage versus peak input pulse power for different signal types and temperatures
 4. S & H amplitude calibration curves: S & H output voltage versus input voltage for each gate at several temperatures
 5. Calibration curves for other analog output signals: TBD
 6. All characteristics of built-in test/calibrate system
 - Calibrated attenuation value
 - Shape and level of IF test signals
 - Shape of video test waveforms
 - AGC voltage, tracking point, waveform sampler values for operation-on-test signals
 7. Probability density functions and autocorrelation functions for selected analog output signals for clean/noisy test signal inputs

 V_{AGC} $V_{(N)}$ $V_{(A/S)}$ $V_G(R)$ $V_I(R)$ $V_G(P)$ $V_I(P)$ $V_G(P1)$ $V_I(P1)$ $V_G(T1)$ $V_I(T1)$

IAW1

IIW1

 \vdots \vdots

IAW16

IIW16

TABLE 3.10

RECOMMENDED ADDITIONS TO SUBSYSTEM PERFORMANCE TESTS*

1. Transmitter
 - a. Statistics of start of altitude countdown relative to transmit pulse (ϵ_{Q1})
 - b. Transmit frequency stability
 - c. TWT time delay versus H. V. level over regulation range
2. Antenna
 - a. Test to verify multipath free range conditions (e.g., demonstrate 1/R signal dependence)
3. Receiver
 - a. Total receiver linearity test (r-f through video amplifier)
 - b. Noise figure test of a batch of mixer/diodes to sample aging characteristics over several months and test environmental dependencies
 - c. Measure receiver dynamic range with AGC voltage fixed (open loop)
 - d. Measure pulse compression SNR improvement for post compression IF values of SNR in the range of 0-13 dB
 - e. Measure receiver pre- and post-detection bandpass characteristics
4. Signal Processor
 - a. Measure tracker jitter statistics using a clutter signal with documented fluctuation statistics and for SNR (post-compression IF) values from "break-lock" to + 10 dB
5. Subsystem performance tests/built-in test and calibrate
 - a. Instrument delay bias measurement versus temperature, warm-up period, and accumulated instrument running time.

*Most parameters should be measured as a function of expected variations in subsystem supply voltage, temperature, input signal level, etc.

TABLE 3.11

RECOMMENDED ADDITIONS TO SYSTEM TESTS

Performance Tests

- a. Noise figure with all subsystems in operation
- b. Acquisition time versus r-f signal level
- c. Tracker break-lock mean value
- d. Internal delay stability
- e. Transmit signal leakage (with r-f output separately terminated) relative to level and time delay of internal calibrate signals

TABLE 3.12

RECOMMENDED ADDITIONS TO ENGINEERING DATA/CALIBRATION DATA TESTS

- A. Measure pulse compression time sidelobes with reasonable time delay between transmit pulse to ensure that receiver recovery effects are not present (e.g., use a coaxial delay line or return from a corner reflector).
- B. Simultaneously record the time difference between the on-board filtered altitude output and a sample-and-hold (S&H) position, with the tracker operating with a clutter signal, to determine whether or not S&H position reconstruction is necessary. Simultaneous records of the tracker error signal are also desirable.
- C. Measure drift characteristics of the tracking gate positions with respect to the transmit pulse.
- D. Measure receiver response to a short pulse (~one nanosecond).

REFERENCES

- 3.1 Cohen, C. J.; and Zondek, B.: Accuracy of Deflection of the Vertical Derived from Satellite Altimetry. Technical Report TR-2626, Naval Weapons Laboratory, Dahlgren, Virginia, October 1971.
- 3.2 GEOS-C Radar Altimeter - Volume I. Technical Proposal, Phases II and III: Submitted in response to Applied Physics Laboratory of John Hopkins University's Request for Proposal for GEOS-C Radar Altimeter, Phases II and III AC-10126, by the General Electric Company, Aerospace Electronic Systems Department, Utica, New York, May 1972.
- 3.3 Gradshteyn, I. S.; and Ryzhik, I. M.: Tables of Integrals, Series, and Products. Academic Press, New York, 1965.
- 3.4 Sakrison, D. J.: Notes on Analog Computation. Van Nostrand Reinhold, New York, 1970.
- 3.5 McAulay, R. J.; and Hofstetter, E. M.: Barankin Bounds on Parameter Estimation. IEEE Trans. Information Theory, Vol. IT-17, No. 6, November 1971, pp. 669-76.
- 3.6 Seidman, L. P.: Performance Limitations and Error Calculations for Parameter Estimation. Proc. IEEE, Vol. 58, No. 5, 1970, pp. 644-52.
- 3.7 Glave, F. E.: A New Look at the Barankin Lower Bound. IEEE Trans. Information Theory, Vol. IT-18, No. 3, May 1972, pp. 349-56.
- 3.8 Van Trees, H. L.: Detection, Estimation, and Modulation Theory, Part III. John Wiley, New York, 1971.
- 3.9 Analysis of Satellite Altimeter Signal Characteristics and Investigation of Sea-Truth Data Requirements. Final Report, Contract No. NAS6-1952, Research Triangle Institute, April 1972.

APPENDIX 3A

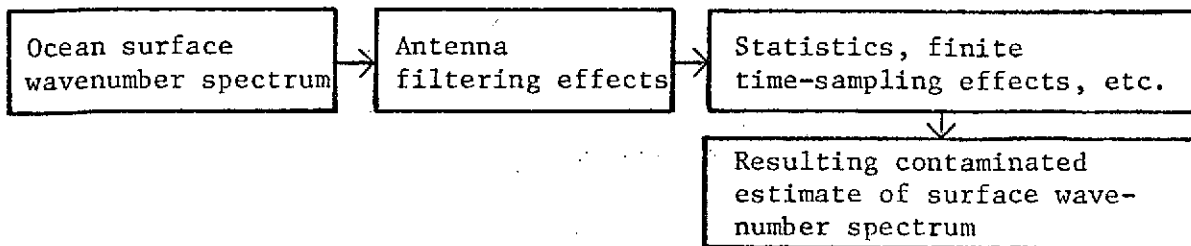
As a number of authors have noted, the determination of geodetic data by spacecraft experiments is similar to the study of a noisy signal after passage through an electrical filter. For example, the geoid can be determined from orbit perturbations of the spacecraft; in this case the equivalent filter is a low pass filter as the higher harmonics are not sensed by the spacecraft. The particular appeal of the radar altimeter is that it permits the direct measurement of higher order surface harmonics, at least over the ocean and to the extent that effects of ocean currents and meteorological phenomena are either absent or can be corrected. Even for this case, there is an effective higher frequency (shorter surface wavelength) cut-off which is related to the size of the radar footprint (among other things).

Typically, one calculates the radar footprint radius R (for pulse-length limited geometries) from the relationship

$$R = \sqrt{hcT} \quad (3A1)$$

where h is the satellite altitude, c is the speed of light, and T is the radar pulse length; it is then often asserted that the footprint diameter ($2R$) represents the minimum surface wavelength which the altimeter can determine, and that the altimeter response is essentially flat for surface wavelengths greater than $2R$ and zero for wavelengths less than $2R$. We feel that it is correct to approach this subject with the point of view of determining an effective transfer function to describe the satellite altimeter's response to the amplitude a_s of each surface wavenumber k_s ($k_s = 2\pi/\lambda_s$) but that it is not adequate just to assume this transfer function flat out to a cut-off wavenumber $k_c = 2\pi/(2R)$ and zero for $k_s > k_c$. Instead it should be possible to calculate the transfer function, and this appendix sketches the first steps in such a calculation. We have been limited by time and money but the problem is an important one which merits further study.

The point of view used is as sketched below:



Note that the process labelled "Antenna filtering effects" implicitly includes details of the transmitter and receiver impulse response, of the transmitted pulse shape, and of the altitude tracker processing. The starting point is the ocean surface's description by a vector wavenumber spectrum, wavenumber \vec{k} . Any given \vec{k} could equally well be described by a magnitude k , a phase α_k relative to the chosen (arbitrary) origin of the surface coordinate system, and a polar angle describing the orientation of \vec{k} relative to the surface coordinate system's x-axis. We make the assumption that any given wavenumber does not change appreciably in direction over an ocean area centered at nadir and somewhat larger than the radar "footprint". The ocean surface coordinate system's x-axis is arbitrarily chosen to be in the direction of any specific wavenumber magnitude, k_s , being considered. Figure 3A1 summarizes the problem's geometry and the notation to be employed.

As can be seen from Figure 3A1, a non-zero ocean surface elevation z_s , due to the wavenumber k_s , will cause a given incremental scattering area located at ρ, ϕ to be at a different distance, r , from the antenna than would be the case for a perfectly flat sea. Consequently the time at which this incremental area contributes to the radar return will be different from the flat-sea case, and the summation of return signal from the entire ocean ~~surface would be expected~~ to have a time-behavior different from the flat-sea value.

This summation is made easier by noting that $z_s \ll h$ for any case of practical interest; thus to negligible error, the angle θ is unchanged from the flat-sea value. Also, $\phi, \tilde{\phi}$ and ω are the same as for the flat sea. The angle ψ , defined in Figure 3A1 as the angle between the z-axis and the straight line drawn from the satellite to the scattering area, will be taken as the angle that the radar pulse is incident upon the scattering area. This last assumption may be slightly risky as it ignores the slope of the local sea surface relative to the plane $z = 0$, but for the k_s values of interest to geodetic satellite programs the assumption is probably acceptable because of the small slopes anticipated.

From Equation 2A6 of Appendix 2A of this report, the ocean surface impulse response is given by

$$S_{a_s}(t, \xi) = \frac{G_o^2 \lambda^2}{L_p(4\pi)^3} \int_{\text{scattering surface area}} \frac{\delta(t - 2r/c) f^4(\theta, \omega)}{r^4} \sigma^0(\psi) dA \quad (3A2)$$

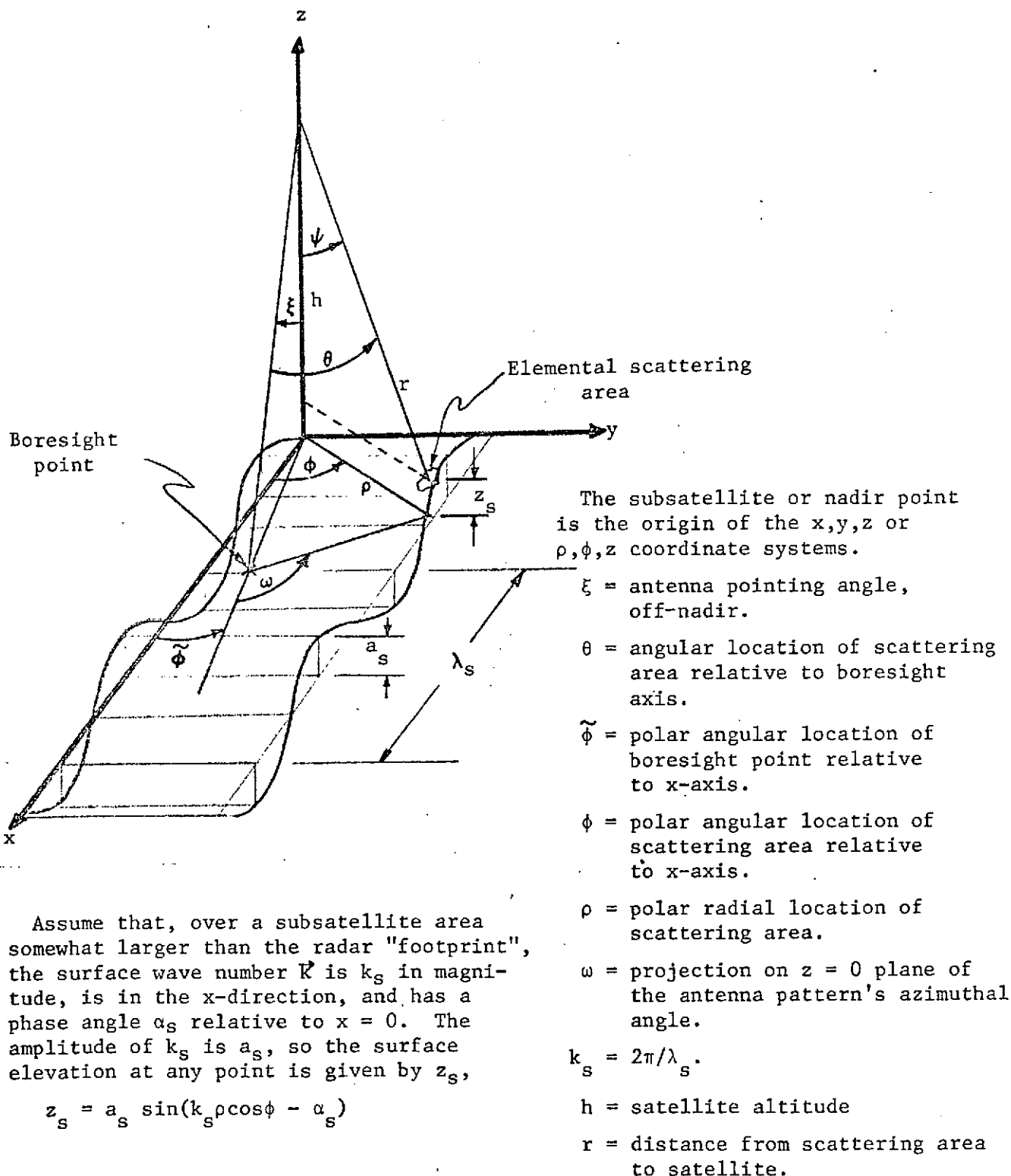


Figure 3A1. Satellite-ocean surface geometry, and summary of notation.

(For convenience of notation in later paragraphs, we use S_{a_s} rather than the P_r of Appendix 2A.) The various quantities not already defined in the present section are as defined in Appendix 2A. Notice that Equation 3A2 contains two approximations. The first is the use of the angle ω to represent the antenna azimuthal angle whereas ω is actually the projection of the azimuthal angle onto the plane $z = 0$. This is unimportant, particularly as one is so often forced to assume antenna patterns of azimuthal symmetry as was the case in the calculations later in Appendix 2A. The second approximation is the already-discussed use of ψ in the backscattering cross-section $\sigma^0(\psi)$. The integration over scattering area surface is carried out using the ρ, ϕ coordinates,

$$dA = \rho d\rho d\phi \quad , \quad (3A3)$$

and so we need a relationship between r and ρ for the δ -function in (3A2). From the triangle whose sides are r , ρ , and $(h-z_s)$, we find that

$$r \doteq h \sqrt{1 + (\rho/h)^2 - 2z_s/h} \quad , \quad (3A4)$$

to an approximation good for all times of interest to the satellite problem. But $r = ct/2$ as well, and using the ranging time τ defined by,

$$t = \frac{2h}{c} + \tau \quad , \quad (3A5)$$

we can find the relationship between ρ and τ to be specified by,

$$\rho^2 \doteq \left(\frac{c\tau}{2} \right)^2 + ch\tau + 2hz_s \quad . \quad (3A6)$$

Notice that unlike the flat-sea case, the relationship between ρ and τ is not unique because of the ϕ dependence contained in the non-zero z_s term of (3A6). The r^4 in the denominator of the integral 3A1 may safely be approximated by

$$r^4 \doteq h^4 (1 + \rho^2/h^2)^2 \quad . \quad (3A7)$$

Then assuming the antenna pattern $f(\theta, \omega)$ to be independent of ω and denoting the pattern by $f(\theta)$, the integral (3A2) becomes

$$S_{a_s}(\tau, \xi) = \frac{1}{2\pi} \int_0^{2\pi} \tilde{S}_{a_s}(\tau, \xi, \phi) d\phi \quad , \text{ for } \tau \geq 0 \quad (3A8)$$

where

$$\tilde{S}_{a_s}(\tau, \xi, \phi) = \frac{G_o^2 \lambda^2}{2(4\pi)^2 L_p h^4} \int_0^\infty \frac{f^4(\theta) \sigma^0(\psi) \delta[\rho - \sqrt{(\frac{c\tau}{2})^2 + ch\tau + 2hz_s}]}{(1 + \rho^2/h^2)^2} \rho d\rho .$$

From Appendix 2A, we have

$$\cos \theta = \frac{\cos \xi + \rho/h \sin \xi \cos(\phi - \tilde{\phi})}{\sqrt{1 + \rho^2/h^2}} \quad (3A9)$$

From Figure 3A1,

$$\tan \psi = \rho/h \quad (3A10)$$

and by earlier definition,

$$z_s = a_s \sin(k_s \rho \cos \phi - \alpha_s) \quad (3A11)$$

Equation (3A8) above is written in terms of $S_{a_s}(\tau, \xi, \phi)$; this notation is introduced here for later reference. While (3A8) as written above implies ρ -integration inside the ϕ -integral, the order of indicated double integration could obviously be reversed and (3A8) rewritten to show ϕ -integration inside a ρ -integral.

Thus (3A8) gives us the desired impulse response function for any specified k_s and $\tilde{\phi}$ with the ρ and ϕ dependence of quantities in (3A8) specified by (3A9)-(3A11), but because of the complexity of the geometry and particularly because of the form of the δ -function argument for non-zero a_s in (3A11), we cannot proceed any further toward the (desired) closed-form result. Expression (3A8) merely serves as a kind of symbolic shorthand to describe the two-dimensional numerical integration which has to be performed. Presumably a grid or cell size will have to be chosen on the ρ, ϕ surface with the δ -function providing a yes-no decision on whether each cell's contribution is to be included in the running subtotal which is the digital computer's approximation to the double integral. A judicious choice will have to be made for the "width" to allow for the δ -function; because of the finite grid cell size and finite computer precision, the argument of the δ -function cannot be required to be exactly zero but must be provided a small width (either side of zero) within

which the δ -function will be non-zero. It is difficult to specify ahead of time how to choose these various parameters for a numerical approximation to (3A8); probably it will be necessary to vary the parameters to empirically ascertain where the numerical integration's result will become reasonably independent of surface grid sizes and δ -widths. This procedure may be expected to be quite expensive in computer running times.

Thus, while the result (3A8) may appear straightforward symbolically, it is of little use for practical reasons. We will now specialize the problem to $\xi = 0$, again assuming azimuthal symmetry of the antenna pattern. Figure 3A2 below reproduces just the plane r, ρ, h from Figure 3A1, at some instant of time τ , for $\tau > 0$.

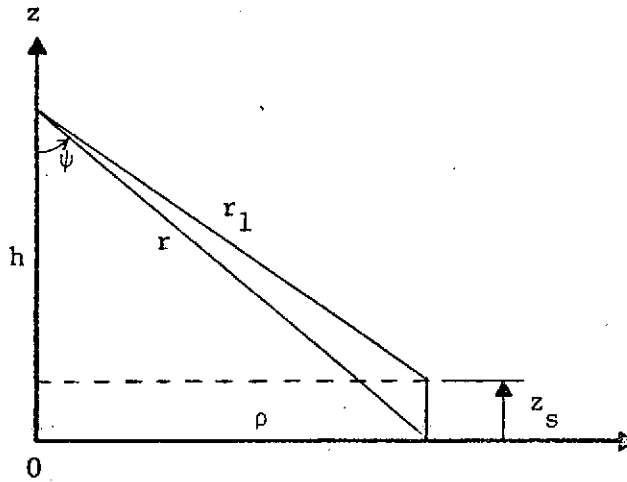


Figure 3A2. Geometry for time $\tau > 0$.

It is seen that r is the distance from satellite to scatterer which we would have if $a_s = 0$, and r_1 is the distance from satellite to scatterer for non-zero a_s . We calculate the time shift $\tau_1 - \tau$ corresponding to the difference between r_1 and r by the following steps:

$$r_1 - r \doteq - z_s \cos \psi \quad (3A12)$$

$$\cos \psi = \frac{1}{\sqrt{1 + (\rho/h)^2}} \quad (3A13)$$

Since $\rho \doteq \sqrt{cht}$, and $z_s = a_s \sin(k_s \sqrt{cht} \cos \phi - \alpha_s)$, and since $(\tau_1 - \tau) = 2(r_1 - r)/c$, then for Δ_τ defined as $\Delta_\tau = \tau_1 - \tau$, we find

$$\Delta_{\tau} = \frac{2a_s}{c} \frac{\sin(\alpha_s - k_s \sqrt{ch\tau} \cos\phi)}{\sqrt{1 + (c\tau/h)^2}} \quad (3A14)$$

Here Δ_{τ} is the time shift such that the impulse response function contribution which would have occurred at τ for $a_s = 0$ now occurs at a new time τ_1 ,

$$\tau_1 = \tau + \Delta_{\tau} \quad (3A15)$$

Now consider the use made of the surface impulse response function $S_{a_s}(\tau, \xi)$. For a transmitted signal $P_t(t)$, the received signal $P_r(\tau, \xi)$ will be given by the following convolution

$$\begin{aligned} P_r(\tau, \xi) &= P_t(t) * S_{a_s}(\tau, \xi) \\ P_r(\tau, \xi) &= \int_{-\infty}^{\infty} S_{a_s}(\tau_1, \xi) P_t(\tau - \tau_1) d\tau_1 \end{aligned} \quad (3A16)$$

If the properties of $P_t(\tau)$ are such that

$$\begin{aligned} P_t(\tau) &= 0 & \tau < 0 \\ P_t(\tau) &= 0 & \tau > T \end{aligned} ,$$

then together with the property $S_{a_s}(\tau) = 0, \tau < 0$, the convolution expression becomes

$$P_r(\tau, \xi) = \frac{1}{2\pi} \int_0^{2\pi} d\phi \int_{\tau-T}^{\tau} \tilde{S}_{a_s}(\tau_1, \xi, \phi) P_t(\tau - \tau_1) d\tau_1, \quad \tau > 0 \quad (3A17)$$

and

$$P_r(\tau, \xi) = 0, \quad \tau < 0$$

In obtaining (3A17), we substituted (3A8) for S_{a_s} and reversed the order of the τ_1 and ϕ integrations. Notice that $\tilde{S}_{a_s}(\tau, \xi, \phi)$ can be characterized (for ξ small or zero) as describing two separate effects: 1) an amplitude effect due to the change in geometry (the difference in ψ and the $1/r^4$ vs $1/r_1^4$ as in Figure 3A2); and 2) a time shift effect as indicated in the discussion of the Δ_{τ} defined by (3A14).

The time shift effect will be very much more important than the amplitude effect for the case $\xi = 0$ and for the relative magnitudes of h and a_s in the

satellite problem. Notice from (3A8) that, if $a_s = 0$ and $\xi = 0$, then $\tilde{S}_o(\tau, 0, \phi)$ is identical to $S_o(\tau, 0)$. Thus for $\xi = 0$ and the already-assumed azimuthal antenna beam symmetry, a very good approximation to (3A17) is obtained by substituting $\tilde{S}_o(\tau_1, 0)$ for $S_o(\tau, 0, \phi)$ in the integrand,

$$P_r(\tau, 0) \doteq \frac{1}{2\pi} \int_0^{2\pi} d\phi \int_{\tau+\Delta_\tau-T}^{\tau+\Delta_\tau} S_o(\tau_1, 0) P_t(\tau + \Delta_\tau - \tau_1) d\tau_1 \quad (3A18)$$

In (3A18) one can for all times of practical interest approximate (3A14) by

$$\Delta_\tau = \frac{2a_s}{c} \sin(\alpha_s - k_s \sqrt{ch\tau} \cos\phi) \quad (3A19)$$

This expression for $P_r(\tau, 0)$ still will require fairly extensive computer times for actual evaluation, but no unclear decisions or "widths of delta functions" are required as compared to our discussion of (3A8). The virtue of (3A18) is that $S_o(\tau, 0)$ can be evaluated once and entered in the computer as a table of values vs. τ ; it may even be possible to approximate $S_o(\tau, 0)$ by a single function as in Appendix 2A, equation (2A16) of this report.

If the problem is not restricted to $\xi = 0$, we see from (3A18) and (3A8)-(3A11) that for non-zero ξ , the θ -dependence on ϕ will prevent the use of a previously calculated or tabulated set of values for $S_{a_s}(\tau, \xi)$ in (3A18). Instead, the integral of (3A8) must be put into (3A18), leading to a triple integration and the already-discussed problem of the proper choice of a "delta-width".

To see what (3A18) means let $k_s \rightarrow 0$ but keep a_s non-zero. Then

$$\Delta_\tau \doteq \frac{2a_s}{c} \sin\alpha_s, \quad (3A20)$$

$$k_s \rightarrow 0$$

and

$$P_r(\tau, 0) = \int_{\tau+\Delta_\tau-T}^{\tau+\Delta_\tau} S(\tau_1, 0) P_t(\tau + \Delta_\tau - \tau_1) d\tau_1 \quad (3A21)$$

$k_s \rightarrow 0$

By changing variables, (3A21) may be rewritten as

$$P_r\left(\tau - \frac{2a_s}{c} \sin \alpha_s\right) = \int_{\tau-T}^{\tau} S_o(\tau_1, 0) P(\tau - \tau_1) d\tau_1 \quad (3A22)$$

$$k_s \rightarrow 0$$

Thus for $k_s \rightarrow 0$, the result is a simple time-shift of the signal from the flat-sea situation, with the maximum time shift being $2a_s/c$ and the actual time shift determined by the phase angle α_s which, in effect, described the surface harmonic phase at the satellite nadir point. The condition $k_s \rightarrow 0$ actually means $k_s \ll 2\pi/(2R)$ with R as given by (3A1). (Notice also that (3A22) becomes the usual time convolution if $a_s = 0$.)

Holding a_s fixed at some typical value (perhaps a couple of meters), it will be necessary to consider the details of the altitude tracker loop and determine the balance point for the different shaped waveforms $P_r(\tau, 0)$ produced as k_s is increased. The entire process can be carried out for a number of different k_s values, holding a_s fixed and setting $\alpha_s = \pi/2$ (the maximum deviation from flat-sea), and the results will eventually lead to a graph of the approximate form shown below.

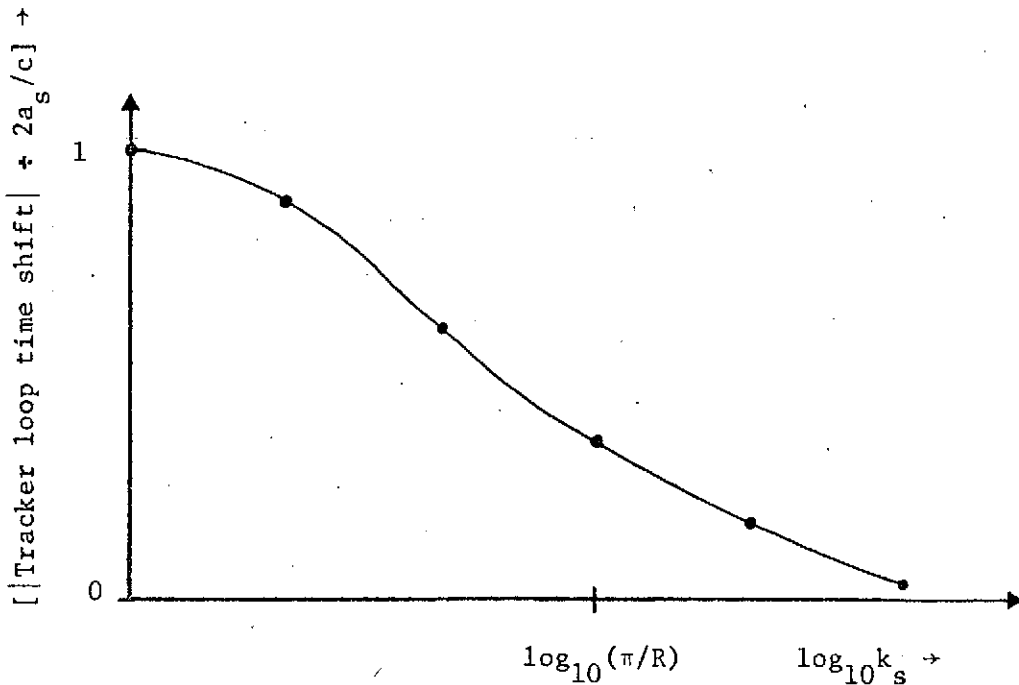


Figure 3A3. Sketch of normalized tracker time-shift vs. k_s , for $\alpha_s = \frac{\pi}{2}$.

This curve is the desired result, the wavenumber transfer function which describes the effects of the footprint filtering process on the wavenumber spectrum. Of course, this discussion has been in the idealized limit (only waveform ensemble averages have been considered), and so the results of a program of calculations based on (3A18) would represent the fundamental limits of the altimeter measurement of surface harmonics. We have not carried out such a program, but have described in this appendix how to begin on the problem.